Université catholique de Louvain

École Polytechinique de Louvain
ICTEAM Electrical Engineering

Improved Ray-Tracing for Advanced Radio Propagation Channel Modeling

Francesco Mani

Thèse présentée en vue de l'obtention du grade de Docteur en Science de l'Ingénieur

Composition du Jury

Prof. Claude Oestges (UCL, Belgium), Promoteur
Prof. Danielle Vanhoenacker-Janvier (UCL, Belgium), Président
Prof. Christophe Craeye (UCL, Belgium)
Prof. Vittorio degli Esposti (Università di Bologna, Italy)
Dr. Katsuyuki Haneda (Aalto University, Finland)

Juin 2012

Acknowledgements

Despite what one may think, the work behind a PhD thesis is definitely not an individual work. For this reason, I would like to spend few lines to thank all the people that made this achievement possible.

First and most important of all, I would like to express my greatest gratitude to my advisor Prof. Claude Oestges for his guidance and support. His constant help and always useful advices made the accomplishment of this thesis much easier to me. It has been a pleasure to work with him through all these years. I would also like to thank him for his effort to find the financial support that made this thesis and the opportunity to present the results achieved in many international symposia possible.

A significant part of this thesis would not have been possible without the fruitful collaboration with Prof. Vittorio degli Esposti and Dr. Enrico Vitucci from University of Bologna in Italy. I am sincerely grateful for their cooperation and for their hospitality during my short but important visit to their department.

I would also like to thank the aforementioned Prof. Vittorio degli Esposti, Dr. Katsuyuki Haneda, Prof. Danielle Vanhoenacker-Janvier and Prof. Christophe Craeye for having devoted part of their time to serve as member of the jury of this thesis. All their comments were important to improve significantly the quality of this work.

Measurements play a crucial role in channel modeling and carrying out a measurement campaign is a task more complex than one may think. It includes logistics, manufacture and the collaboration of many people. I would like to thank all the present and past colleagues and friends from the propagation group and ICTEAM department that helped me in this difficult task: Olivier, Ling, Pat, Nizabat, David, Maxime, Lyazid and Ulas. For the same reason, I would like to thank Pascal Simon, Robert Platteborze and David Spote, technicians of ICTEAM department and WELCOME laboratory, for their assistance. In this context, my gratitude goes also to Dr. François Quitin for sharing part of his measurements and research. His collaboration has been essential for realizing an important part of this work.

My final thanks go to my parents and friends for their support and encouragement during all these long years.

Contents

List of Figures

List of Tables

List of abbreviations

AoA Azimuth of Arrival

AoD Azimuth of Departure

BER Bit Error Rate

BS Base Station

DMC Dense Multipath Component

EM Electomagnetic

EoA Elevation of Arrival

EoD Elevation of Departure

GTD Geometrical Theory of Diffraction

GO Geometrical Optics

GSCM Geometry-Based Stochastic Channel Models

HPBW Half-Power BeamWidth

LOS Line of Sight

MIMO Multiple Input Multiple Output

MPC Multipath Component

MRE Mean Relative Error

MT Mobile Terminal

NLOS Non-Line of Sight

OFDM Orthogonal Frequency-Division Multiplexing

PDP Power Delay Profile

RMS Root Mean Square

RMSE Root Mean Square Error

RT Ray-Tracing

SISO Single Input Single Output

UTD Uniform Theory of Diffraction

UWB Ultra Wide Band

VNA Vector Network Analyzer

XPD Cross-Polar Discrimination

Vectorial notations

- Notation for unit vectors is as $\hat{u}$
- Notation for vectors is as $\mathbf{v}$ or $\mathbf{V}$
- Notation for dyads is as $\overline{\mathbf{D}}$
- Notation for matrices is as $[M]$

Abstract

The characterization of the wireless propagation channel has always been an important issue in radio communications. However, in recent years, given the dramatic increase of demand in terms of capabilities of wireless systems, e.g. data rate, quality of service etc., the study of propagation has become of crucial importance. As measurements are generally costly and time consuming, channel models are widely used for this purpose.

The modeling of propagation may rely on different types of models: empirical, statistical and deterministic. Typically, the latter, based on the electromagnetic properties of the propagating waves, relies on Ray-Tracing (RT), a geometrical optic technique used to evaluate the paths followed by rays as they interact with the environment. This technique has been widely used to predict the behavior of propagation both in outdoor and indoor scenarios. Classic RT tools take into account line of sight propagation, specular reflection and diffraction, with penetration included when indoor propagation is considered.

With the advent of diversity techniques and MIMO systems, whose goal is to exploit the multi-dimensional properties of a channel, it is required that the prediction models are capable to analyze propagation in depth, i.e. including polarization, delay and angular behavior of a channel. A 3-D RT tool has the great advantage to be able to provide inherently that kind of information, but to achieve a sufficient accuracy, it is necessary to develop an advanced prediction tool. To this goal in this thesis a pre-existent RT software [1] has been improved by implementing in it propagation mechanisms as penetration, diffuse scattering and contributions by vegetation.

After an introduction to wireless propagation in general and RT techniques in particular, in the first part of the thesis all the propagation mechanisms of the advanced version of the UCL RT tool, both the pre-existent and the newly implemented ones, are presented. The main part of the thesis is the parameterization and validation of the simulated results with measurements. It has been carried out in different scenarios, both indoor and outdoor, and a particular focus has been dedicated to the role of diffuse scattering, which results to represent a significant part of the received signal. In this context, in collaboration with the propagation group from University of Bologna, a polarization model for diffuse scattering has been developed, parameterized with ad-hoc measurements, implemented and validated in typical scenarios. The thesis is concluded with some practical applications of the developed RT tool.

1

Introduction

1.1 The wireless communication channel

A communication system is a system whose goal is to reproduce at one point either exactly or approximately a message selected at a different point, as stated in the milestone paper by Shannon *A Mathematical Theory of Communication* [2]. Fig 1.1 presents a schematic version of this concept.

The communication channel is the medium over which the message is conveyed from a transmitting point to a receiving point. In wireless communications, the information is transmitted between units that are not physically connected. In wireless radio communications, the signal is an electromagnetic (EM) wave transmitted and received by antennas that may or may not be considered part of the channel depending on the system under consideration. Before transmission, the message has to be opportunely modified into a signal suitable for the type of communication and for the characteristics of the channel. The transmitted signal is modified by the communication channel, depending on its characteristics. This effect is depicted in the scheme of Fig. 1.1 with the block called *Noise Source.* In wireless systems, the noise sources can be divided into multiplicative and additive ones [3]. This can be described using the well-known formula:

$$x\left(t\right) = h\left(t, \tau\right) \otimes y\left(t\right) + n\left(t\right) \tag{1.1}$$

$x\left(t\right)$ and $y\left(t\right)$ are, respectively, the time-variant transmitted and received signal and $n\left(t\right)$ is the additive noise, that is normally either generated inside the receiver itself or by some interfering signal. Propagation delay τ is defined as the time taken by a signal to arrive at its destination.

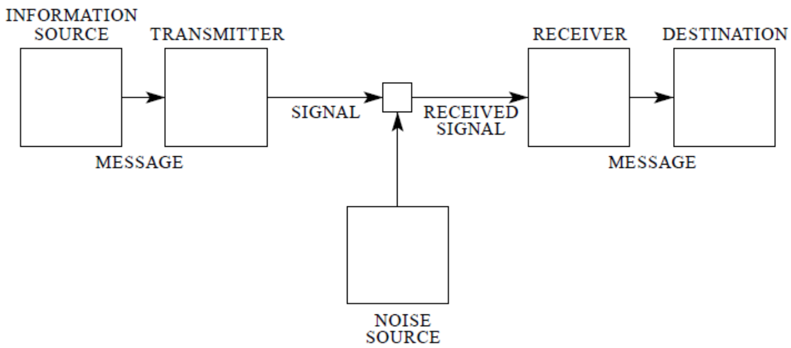

Figure 1.1: Scheme of a communication system [2]

The time-variant impulse response of the channel, $h(t, \tau)$, takes into account the multiplicative effects that are generated by the EM waves interacting with the propagation environment between the transmitter and the receiver. This can be furtherly explained by saying that wireless channels are characterized by multipath propagation (see Fig. 1.2), i.e. the transmitted signal arrives at the receiver via multiple paths displaced in space and delay as results of multiple interactions with the propagation environment. Each path is characterized by a complex amplitude γ, a polarization vector, a delay of arrival τ and directions of departure and arrival $\Omega_{d,a}$. A simplified example of multipath discrete impulse response at a given time t_k is presented in Fig. 1.3.

A way to define the type of wireless communication is by its range and, accordingly, by the propagation environment, i.e. the type of channel. Here is a list of different wireless systems classified by range:

Satellite link The communication is between a geostationary satellite and, normally, a fixed base station on the earth. The propagation is influenced by the atmosphere and by meteorological conditions. If the link is with a mobile user on earth, the environment surrounding the user may also play an important role.

Terrestrial link Fixed links between base stations on earth in the range of tens of kilometers. Atmospheric and terrain effects, together with obstructions by obstacles affect the propagation.

Macrocell The link is between a base station and mobile users with range in the order of kilometers. Outdoor scenario that can be anything between rural and urban are comprised. The base station is generally over the rooftop.

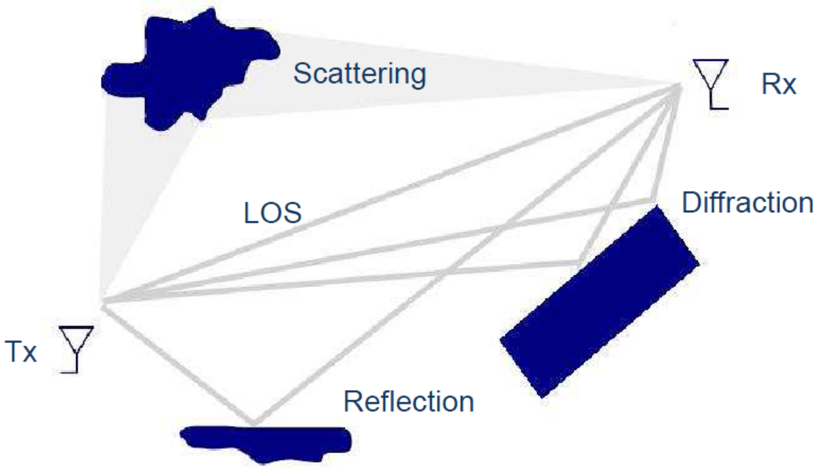

Figure 1.2: Simple scheme of multipath propagation

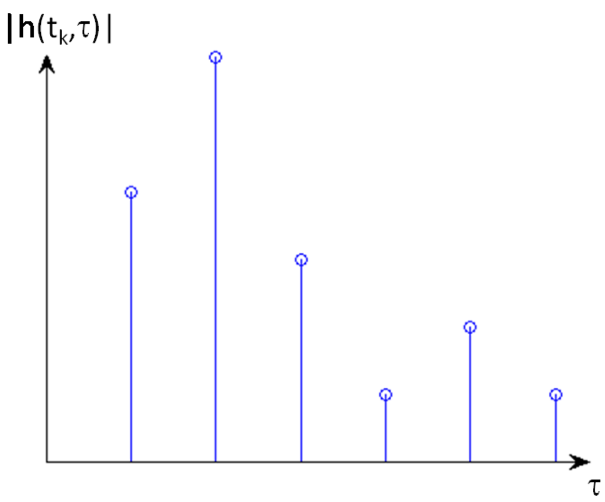

Figure 1.3: Example of discrete channel impulse response at a given time t_k

Microcell Covering a radius of $\approx 500m$ between a base station and mobile users. Typically used in dense urban scenario with the base station below roof top level. Propagation is determined by the surrounding scenario.

Picocell Both terminals may be either fixed or mobile with a maximum distance of $\approx 100m$. It represents indoor scenarios, e.g. offices, public areas and shopping malls, where the propagation characteristics depend on the type of environment, size and shape of the rooms, presence of people and so on.

In the following two sections, the metrics that characterize the wireless channels and the way different channels can be modeled are briefly presented.

1.1.1 Channel characteristics

If propagation in free space is considered, as starting point, it is well know that an EM wave experiences the following isotropic path loss:

$$L_{fs} = \left(\frac{4\pi d}{\lambda}\right)^2 \tag{1.2}$$

where d is the distance between transmitter and receiver and λ is the wavelength. In general, **path loss** can be definded as the attenuation with distance of an EM wave as it progresses in the propagation environment. Commonly, this law is approximated with the following equation [4]:

$$L = L_0 \left(\frac{d}{d_0}\right)^\gamma \tag{1.3}$$

where d_0 is a reference distance, L_0 takes into account additional losses of the system and γ is the path loss exponent. It is not difficult to see that this last parameter is a measure of how fast the path loss increases with distances. The path loss exponent strongly depends on the propagation environment. In free space $\gamma = 2$, in a simplified scenario where LOS and ground reflection are considered $\gamma = 4$ and in general it can be deduced empirically from measurements. In case of scenarios that create a waveguide effect, $\gamma \leq 2$ can be found, while in scenarios where there is a severe attenuation, e.g. an indoor scenario with terminals on multiple floors, it can be as high as $\gamma = 6$.

In practice, it is not true that the received power is constant for a fixed distance in a given environment. In fact, path loss is a parameter that is able to predict only the local median behavior of the channel [3]. If a macrocell is considered and receivers are placed on a ring at a certain distance from the base station, different obstacles will influence in a different way the propagation environment relative to each receiver through blockage, reflections, diffractions, etc. causing a random variation of the received signal around the median path loss. This effect is called **shadowing** (or large-scale fading) and it has been shown that it can be modeled both in outdoor [5] and indoor [6] scenarios as a log-normal random variable.

Shadowing is a large-scale phenomenon. This means that its effects on the received power occur over *large* distances. Nevertheless, if the receiver is moved over *small* distances the received power may still varies significantly. This small-scale effect is called **fading** (or, more precisely, small-scall fading) and it is generated by constructive and destructive interference of the different propagation paths that contributes to the received power. Fading is modeled as a random process and, generally, it can be described by two probability distribution: Rayleigh, when all the paths have the same average energy, and Rice, when there is a dominant path (generally, but not necessarily, LOS).

Each path arrives at the receiver covering a different distance, thus with a different delay. This means there is a delay dispersion of the transmitted signal at the receiver. **Delay spread** is the metric that analyzes this channel characteristic and can be evaluated, in its root means square form, as it follows:

$$\tau_{rms} = \sqrt{\frac{\int_0^{\tau_{max}} (\tau - \tau_m)^2 P_h(\tau)\, d\tau}{\int_0^{\tau_{max}} P_h(\tau)\, d\tau}} \tag{1.4}$$

where the power delay profile $P_h(\tau)$ is

$$P_h(\tau) = E\left\{ |h(t,\tau)|^2 \right\} \tag{1.5}$$

and the mean delay τ_m is

$$\tau_m = \frac{\int_0^{\tau_{max}} \tau P_h(\tau)\, d\tau}{\int_0^{\tau_{max}} P_h(\tau)\, d\tau} \tag{1.6}$$

The **Coherence bandwidth**, B_{co}, is a measure of the range of frequencies over which the channel can be considered flat (i.e. it passes all spectral components with approximately equal gain and linear phase [7]) and it is proportional to the inverse of delay spread. If the bandwidth of the transmitted signal is $B \ll B_{co}$ fading across the signal bandwidth can be considered constant and we can refer to it as **flat fading**. On the other hand, if $B \gg B_{co}$, different frequency components of the signal are affected by decorrelated fading resulting in what is called **frequency selective fading** [4].

Fading is a very critical phenomenon that causes detrimental effects on the quality of the communication. A technique to overcome this problem is **diversity**. Its principle is simple: if the transmitter and the receiver units are connected together via statistically independent channels, the probability that all these channels experiences simultaneously a fading dip is much lower than the probability that a single channel does it [8]. If the signal received through these channels are efficiently combined, the quality of the communication can be largely improved. If the channels are not independent, i.e. there is correlation between them, the effectiveness of diversity decreases. This can be measured through the correlation coefficient:

$$\rho_{xy} = \frac{E\left\{xy^*\right\} - E\left\{x\right\} E\left\{y\right\}}{\sigma_x \sigma_y} \tag{1.7}$$

where x and y are the random variables representing the two signals and σ is the standard deviation. Four main types of diversity are employed: space, time, frequency and polarization.

Spatial diversity is the simplest method. It takes advantage of using multiple antennas at transmit and/or at receive side. The key point is to have the antennas distant enough to receive decorrelated signals (with the trade-off that they have to fit on the size of the terminal, of course). An important channel parameter that is related to spatial diversity is the root mean square angular spread, i.e. the larger the spread the lower the spacing between the antennas to have decorrelated signals. For a generic angle ψ, it can be evaluated in the following way:

$$\sigma_\psi = \sqrt{\frac{\int \left|e^{j\psi} - \mu_\psi\right|^2 APS\left(\psi\right) d\psi}{\int APS\left(\psi\right) d\psi}} \tag{1.8}$$

where APS is the angular power spectrum and the average angle μ_ψ is

$$\mu_\psi = \frac{\int e^{j\psi} APS\left(\psi\right) d\psi}{\int APS\left(\psi\right) d\psi} \tag{1.9}$$

Temporal diversity takes advantage of the time-variance of the channel. Two replicas of the signal can be considered uncorrelated if they arrive in a time interval greater than $1/2f_m$, where f_m is the maximum Doppler frequency. The Doppler effect is the change of frequency of the impinging wave due to the speed of the mobile terminal. The maximum Doppler frequency is:

$$f_m = f_c \frac{v}{c} \tag{1.10}$$

where f_c is the carrier frequency and v is the mobile terminal speed.

Frequency diversity exploits the fact that, if a signal is transmitted at two frequencies with a spacing greater than the coherence bandwidth of the channel (B_{co}), the fading of the two received signals can be considered decorrelated.

The propagation environment may produce a depolarization of the transmitted signal. Hence a receiver with dual-polarized antennas may profit from polarization diversity. The advantage of this technique is the possibility to co-locate two orthogonally polarized antennas obtaining almost independent fading. The drawback is that cross-polarized channels may yield a higher average attenuation depending on the polarization properties of the channel, degrading the effectiveness of diversity.

1.1.2 Channel models

Channel measurements are costly and time consuming. Hence, to plan or design a wireless communication system, the propagation channel is often simulated thanks to channel models. These models fall under the following main categories: empirical, stochastic and deterministic.

Empirical channel models are directly obtained by extensive channel measurements in typical propagation scenarios. Statistical analysis is performed on the measurements to obtain a set of prediction equations. Generally speaking, empirical models are used in macrocell scenarios to predict narrow-band characteristics of the channel, mainly path loss. In this case, typical input parameters are: type of environment (e.g. urban, sub-urban, rural etc.), building heights, antenna heights, frequency. One of the most popular macrocell empirical models is the Okumura-Hata [9]. Its formulation is the following:

$$L_{dB} = A + B \log(d) - C \tag{1.11}$$

where d is the distance between the base station and the mobile terminal, A and B are parameters that depend on the frequency and base station height, while C depends on the frequency, the mobile terminal height and the type of propagation environment (urban, sub-urban and open area). This model is based on measurements done in Tokyo and it is limited between 0.2 and 2 GHz. Empirical models are available also for picocell indoor scenarios, e.g. the multi-wall COST231 model [10] that considers number and type of walls and floors crossed. The main advantage of such models is their simplicity together with the low computation time. On the other hand, there is little or no physical insight in these models, their parameters (e.g. frequency) are normally limited to a quite narrow range and they are strongly related to the measurement environment from which they are derived, e.g. the urban environment of the Hata model is the one in Tokyo that is very different from typical European one.

The second type of channel model is the stochastic one, where the channel is described through its statistical parameters. These models are not directly derived by measurements, but typical measurement scenarios are used to derive their parameters. They are generally more complex than empirical ones, but they can provide a much more detailed description of the channel characteristics. A classical example is the Saleh-Valenzuela model for indoor propagation [11], where the multipath propagation is described in terms of cluster of paths with similar delay of arrival and the impulse response of the channel is defined as:

$$h\left(\tau\right)=\sum_{l=0}^{L}\sum_{k=0}^{K}\beta_{kl}e^{j\theta_{kl}}\delta\left(\tau-T_l-\tau_{kl}\right) \tag{1.12}$$

where β_{kl} is the gain of the k^{th} ray of the l^{th} cluster, T_l is the delay of arrival of the l^{th} cluster and τ_{kl} is the delay of arrival of the k^{th} ray measured from the beginning of the l^{th} cluster. Within each cluster the power is assumed to have an exponential decay, while the delay of arrival of each path inside the cluster and the relative delay of the clusters themselves are assumed to be Poisson distributed.

Another important family of stochastic models is the one that goes under the name of Geometry-Based Stochastic Channel Models (GSCM). Here, it is the position of the scatterers and the properties of scattering interactions that are statistically modeled and consequently each propagation path intrinsically includes amplitude, delay and angular information [12]. The great advantages of such models, when compared with the ones presented so far, are their much higher relation to actual physical propagation and the fact that they can implicitly reproduce full channel characteristics, i.e. the double-directional channel described by the equation [13]:

$$h\left(\tau,\nu,\Omega_t,\Omega_r\right)=\sum_{k=0}^{K}\gamma_k\delta\left(\tau-\tau_k\right)\delta\left(\nu-\nu_k\right)\delta\left(\Omega_t-\Omega_{t,k}\right)\delta\left(\Omega_r-\Omega_{r,k}\right) \tag{1.13}$$

where τ is the delay of arrival, ν is the Doppler shift, Ω is the anglular information either at transmit or receive side and γ is the complex path attenuation. The latter information may also include polarization properties, i.e. be represented by the polarization matrix. A sub-group of GSCMs are the clustered models. A cluster, in this case, is a group of propagation paths with similar propagation parameters, in terms of angles and delay taken jointly [14]. The aim of these models is to directly characterize clusters, i.e. the location in space of clusters of scatterers but also the different parameter spreads that each cluster yields, rather than single propagation paths.

All the models presented to this point aim at representing, statistically or empirically, a wide range of propagation environments (i.e. outdoor urban or indoor office) with similar characteristics. In both cases, either for the derivation of the model or its parameterization, they rely on measurements carried out on specific scenarios. It is evident that the critical step of such approach is to establish a representative scenario where to carry out measurements. Then, a very important step in those kinds of models is the validation of the model derived, or the parameters extracted, in scenarios different from the original one (but of course within the same range of validity). Otherwise there is the risk of developing a model valid only in the electrical engineering offices of a certain university or in a particular neighborhood of a certain city.

This problem is not present in deterministic channel models where the validity is independent from the environment of application as they are based on the actual physical propagation of EM waves in a deterministic scenario, specified by its geometrical and electromagnetic characteristics. On the other hand, the results provided are specific to the site under consideration. Their accuracy is generally high, but it is directly related to the accuracy of the scenario representation. The major drawback of these models is the high computational effort required.

The most accurate deterministic methods are the ones that directly derive from the solution of Maxwell's equations, e.g. the Method of Moments (MoM) or the Finite Difference Time Domain (FDTD) method. Their complexity makes their utilization impractical in most large-scale propagation environments. The most commonly used family of deterministic models is the ray-based approach, that approximates Maxwell's equation following geometrical optics high-frequency criteria. Section 1.1.3 presents in more details these models.

1.1.3 Ray-Based propagation models

In a ray-based propagation model a ray represents the propagation of an EM wave and, consequently, it has the following properties:

- a position in space,
- a direction, i.e. from the source (real or virtual) towards the observation point,
- an amplitude,

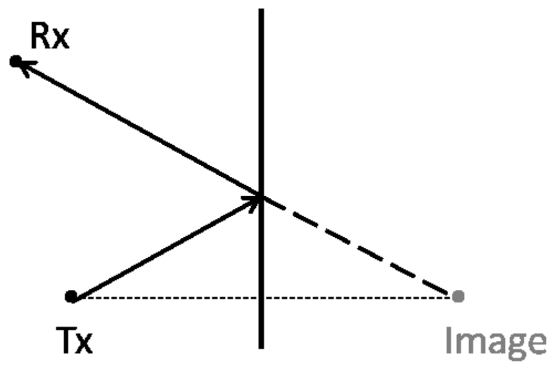

Figure 1.4: The method of images to find a reflection point in RT

- a phase,
- a polarization.

There are two types of ray-based deterministic propagation models: Ray-Tracing and Ray-Launching. The difference lies in the algorithm used to find paths between the source and the observation point [15].

In Ray-Launching, rays are, as the name says, launched from the transmitting position in all possible directions according to a pre-defined angular discretization. This method has a drawback if a point-to-point communication is considered. To collect the rays at receiver side, it is necessary to define an area of a certain extension, normally a sphere [16]. If this area is too small it may fail to collect some relevant rays while if is too large it may include rays that are not actually seen by the receiver [17]. Ray-Launching may be considered a suitable tool for wireless coverage prediction, where whole the propagation environment is divided into pixels over which the strength of the field needs to be evaluated.

On the other hand, geometrical optics (GO) is implemented in a ray-tracing (RT) algorithm according to the method of images. When visible light is reflected on a mirror, the rays coming from the source appear to originate from a point behind the mirror. This point is called the image of the source. This principle is applied in RT to find a reflection point, that is found intersecting the line connecting the observation point and the image with the surface on which reflection takes place. This principle is depicted in Fig. 1.4.

1.2 Introduction to Geometrical Optics

Geometrical optics is a high frequency approximation that can be used to describe the propagation of electromagnetic waves. In a high frequency technique, despite the name, there is no general frequency boundary that assesses its validity. The validity of the method depends on the problem to which it has to be applied. In particular for GO, it is possible to state that it is applicable at given frequency if the size of the scatterer is large when compared to the wavelength [18].

In GO, propagation is described in terms of rays, but it has to be clear that a ray is just a model for the path taken by EM radiation emitted by a source, not the actual emission. Each ray is perpendicular to the local wavefront [19], therefore collinear with the wavevector.

The main property of a ray is that of being a straight line. It is possible to derive this property from the principle that can be considered one of the basis of GO: *Fermat's Principle.* Fermat stated that the path taken by a ray of light between two points is the path that can be traversed in the least time. The modern and generalized form is the following:

Generalized Fermat Principle. *A ray traveling from one point to another will follow the path which corresponds to a stationary value, i.e. a maximum, a minimum or an inflection point, of the optical path length.*

Considering that in a homogeneous medium the time taken along a straight path is minimum compared to any other one, the property is demonstrated. A direct consequence of *Fermat's Principle* is the reversibility of a path, i.e. if a path traveling from A to B is a minimum, the same holds for the reverse path from B to A. Another property of GO rays is the mutual independence. If several rays are crossing a medium at the same time in different directions, the path of any ray is the same as if it would have been alone [20].

In practical GO applications a ray will intersect obstacles, i.e. a boundary between two media characterized by different refraction indices, thus generating two possible interactions:

- reflection,
- refraction

as depicted in Fig. 1.5.

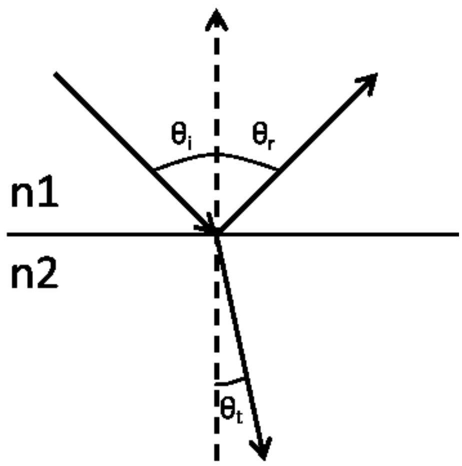

Figure 1.5: Illustration of reflection and refraction mechanisms when a ray impinges on a boundary between two media characterized by different refraction indices

1.2.1 Reflection

Reflection, or specular reflection to distinguish it from diffuse reflection, is that interaction for which a surface acts as a mirror with the impinging ray, reflecting it in a single direction. This is defined by the *Law of Reflection*, that states:

Law of Reflection. *The incident ray, the reflected one and the normal to the surface at the reflection point are coplanar and the angle of incidence equals the angle of reflection.*

This law is a direct consequence of *Fermat's Principle* that can also be interpreted as saying that, among all points on a surface, the one that contributes to the reflection is the point for which the path that connects it to the source and the observation point is a stationary point. Geometrically speaking, reflection can be easily summarized as it follows:

$$\theta_i = \theta_r \tag{1.14}$$

where θ_i is the angle of incidence and θ_r is the angle of reflection.

1.2.2 Refraction

Refraction is the change of direction of a ray due to the transition from two media with different refraction indices n. Refraction is governed by the well known *Snell's Law*, that puts in relation the sines of the angles of incidence and refraction with the refraction indices of the two media in the following way:

$$\frac{\sin\theta_i}{\sin\theta_t} = \frac{n_2}{n_1} \tag{1.15}$$

where θ_t is the angle of refraction and n_1 and n_2 are the refraction indices in the medium of the impinging ray and of the refracted ray respectively. Also this law follows directly *Fermat's Principle*, considering that the refraction index is inversely proportional to the phase velocity of a wave in the medium.

Let us consider the case of an EM wave propagating on a medium denser than the one on which it impinges, i.e. $n_1 > n_2$. According to Eq. 1.15 the sine of the angle of transmission is directly proportional to n_1/n_2, that may lead to $\sin\theta_t$ exceeding unity. It is clear, then, that it is possible to define a critical incident angle for which $\sin\theta_t = 1$ and $\theta_t = \pi/2$. Defining this critical angle as

$$\theta_{ic} = \arcsin\frac{n_2}{n_1} \tag{1.16}$$

for $\theta_i \geq \theta_{ic}$ there is total internal reflection, i.e no propagative transmission into the medium characterized by n_2.

1.2.3 Diffraction or where Geometrical Optics fails

Let us consider an impenetrable obstacle and an emitting source. GO, in this situation, only permits direct and reflected rays. Thus, there will be a region, masked by the obstacle, where the direct rays cannot arrive and another region reachable with direct rays but not with reflected rays. The boundaries of these regions are called Incident Shadow Boundaries (ISB) and Reflected Shadow Boundaries (RSB) respectively. In Fig. 1.6 the grey squares zone is the incident field shadow region, while the one with grey lines is the reflected field shadow region. This led to the conclusion that GO fields are strongly discontinuous at the shadow boundaries and are equal to zero inside the incident field shadow region. A basic electromagnetic rule states that an EM field must be smooth and continuous everywhere and it is known that it is not equal to zero in the shadow region. GO, as it has been defined, fails to model in an accurate way the propagation in presence of an obstacle in its shadow region and at the shadow boundaries. For these reasons, an extension of GO is needed.

Knowing that diffraction is responsible for the fields in the shadow region, a Geometrical Theory of Diffraction (GTD) was proposed by Keller [21]. GTD states that diffraction can be caused by rays impinging

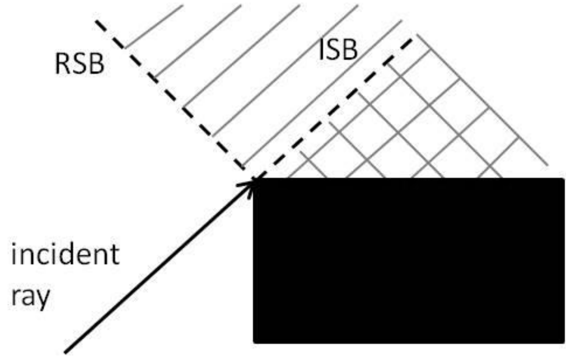

Figure 1.6: Incident ray and shadow boundaries

on edges, vertices and also curved surfaces. A diffracted ray, that follows Fermat's principle, is then generated. The following laws of diffraction are derived accordingly.

Law of Edge Diffraction. *A diffracted ray and the corresponding incident ray make equal angles with the edge at diffraction point and they lie on opposite sides of the plane normal to the edge at diffraction point.*

Law of Vertex Diffraction. *A diffracted ray and the corresponding incident ray may meet at any angle at the vertex of a boundary surface.*

Law of Surface Diffraction. *An incident ray and the resulting surface diffracted ray in the same medium are parallel to each other at diffraction point and lie on opposite sides of the plane normal to the ray at diffraction point.*

While GTD is able to predict a non-zero field in the incident shadow region, it has still a major drawback. It becomes singular in the region, called transition region, across the shadow boundaries. In [22], the Uniform Theory of Diffraction (UTD), a solution that compensates for the discontinuities at the shadow boundaries, was firstly presented. A transition function was introduced so that its multiplication with the GTD diffraction coefficients keeps the field continuous also at the boundaries, making the diffraction theory valid everywhere in space, i.e. uniform.

1.3 Diffuse reflection

Specular reflection, as defined in section 1.2.1, directs the energy of a ray in a single direction. This may happen only in case of a wave that impinges on a perfectly smooth surface. Consequently, it is possible to say that if the surface is rough it will spread the energy of an incident wave in multiple directions [23]. This also means that, following this definition, the same surface may be rough or smooth depending on the frequency of the impinging wave. Hence, it is necessary to define a criterion to distinguish the two possibilities. A surface can be considered smooth if it generates scattered waves with a very small phase difference between each other [3]. This may lead to the well known Rayleigh criterion for a rough surface

$$\Delta h > \frac{\lambda}{8 \cos \theta_i} \tag{1.17}$$

where Δh is the height of the roughness, that produces the phase difference. This equation shows also that the diffuseness of scattering depends also on the angle of incidence θ_i.

1.4 Electromagnetics for Geometrical Optics

Maxwell's equations are the laws that govern the behavior, within a medium, of electric and magnetic fields in time and space. They describe how charges and currents behave as sources and how a time variant electric or magnetic field generates its correspondent. In a region without any source, it is possible to express the equations in frequency domain, in a homogeneous medium, as it follows:

$$\nabla \cdot \mathbf{E}\left(r,\omega\right) = 0 \tag{1.18}$$

$$\nabla \cdot \mathbf{H}\left(r,\omega\right) = 0 \tag{1.19}$$

$$\nabla \times \mathbf{E}\left(r,\omega\right) = -j\omega\mu\mathbf{H}\left(r,\omega\right) \tag{1.20}$$

$$\nabla \times \mathbf{H}\left(r,\omega\right) = j\omega\epsilon\mathbf{E}\left(r,\omega\right) \tag{1.21}$$

where $\epsilon = \epsilon_0\epsilon_r$ and $\mu = \mu_0\mu_r$ are, respectively, the permittivity and permeability of the medium expressed with respect to their value in free space. In the context of wireless propagation $\mu = \mu_0$ as we deal with non-magnetic media. The characteristic impedance of a medium is defined as $\zeta = \sqrt{\mu_0/\epsilon}$. From Eq. 1.20 and 1.21 it is possible to derive the Helmholtz wave equation

$$\nabla^2\mathbf{E}\left(r,\omega\right) + k^2\mathbf{E}\left(r,\omega\right) = 0 \tag{1.22}$$

where $k = \omega\sqrt{\mu_0 \epsilon}$ is the wavenumber. The velocity of a point of constant phase on the wave (phase velocity) is $v = 1/\sqrt{\mu_0 \epsilon}$.

When a dielectric medium has a conductivity, σ, different from zero it is called lossy medium. In this case Eq. 1.21 can be rewritten as:

$$\nabla \times \mathbf{H}(r, \omega) = -\sigma \mathbf{E}(r, \omega) - j\omega\epsilon\mathbf{E}(r, \omega) \tag{1.23}$$

To have a notation similar to the one for lossless media, an effective dielectric constant, ϵ_e, is introduced and can be written as:

$$\epsilon_e = \epsilon - j\sigma/\omega \tag{1.24}$$

This generates a complex effective wavenumber, $k_e = \omega\sqrt{\mu_0 \epsilon_e}$ that can be also written as $k_e = \beta - j\alpha$, where α is the attenuation factor and β is the oscillation factor.

One of the crucial points of Maxwell's theory of elecromagnetism states the energy travels from one position in space to another as a wave. Different types of waves can be defined. The most simple one is the uniform plane wave, that is the one that has planar surfaces of constant phase. Plane waves are transverse electromagnetic (TEM) waves, i.e. both the electric and the magnetic fields are orthogonal with the direction of propagation $\hat{s}$ and the relation between them is:

$$\mathbf{H} = \frac{1}{\zeta}\hat{s} \times \mathbf{E} \tag{1.25}$$

By analogy, cylindrical and spherical waves are those which equiphase surfaces are concentric cylinders and spheres. A plane wave is a physical abstraction but, in many practical applications, an EM wave can be considered plane in localized regions of space, i.e. at large distance from the source where the longitudinal component of the field is irrelevant and only the transverse ones are significant.

EM problems should be studied by solving Maxwell's equations applying ad-hoc initial and boundary conditions, but only in few cases they can be solved exactly [24]. The Luneberg-Kline asymptotic expansion for a high frequency field in an isotropic medium free of sources can be written as [18]:

$$\mathbf{E}(r, \omega) \sim e^{-jk\Psi(r)} \sum_{n=0}^{\infty} \frac{\mathbf{E}_n(r)}{(jw)^n} \tag{1.26}$$

where $\sim$ means equal in an asymptotic sense and $\Psi(r)$ is the phase function. Ideally when ω, so the frequency, tends to infinite the only significant term is the one for $n = 0$, that is called GO field.

$$\lim_{\omega \to \infty} \mathbf{E}(r, \omega) = e^{-jk\Psi(r)}\mathbf{E}_0(r) \tag{1.27}$$

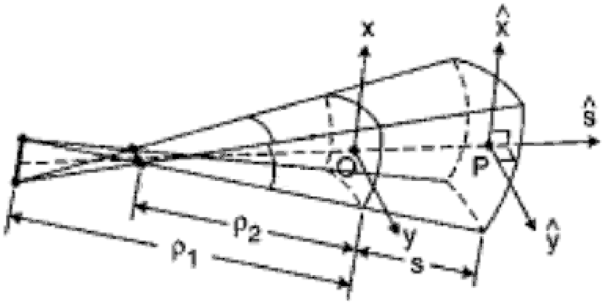

Figure 1.7: Narrow astigmatic ray tube [18]

By mathematical manipulation of Eq. 1.27 (see [18]), it is possible to obtain the eikonal equation

$$|\nabla\Psi\,(r)|^2 = 1 \tag{1.28}$$

that has at least three solutions, that are planar, spherical and cylindrical surfaces.

The Poynting vector

$$\mathbf{S} = \mathbf{E} \times \mathbf{H}^* \tag{1.29}$$

express the magnitude and direction of the power flow per square meter, i.e. the power density. If this is applied to the GO fields and through mathematical manipulations, it is possible to derive

$$\hat{s} = \nabla\Psi \tag{1.30}$$

that is the direction of propagation of a GO ray. Rays that are close to an axial ray form a ray tube [25]. Considering that there is no power flow in a direction transverse to each ray of the tube, there is conservation of energy along the cross section of the tube.

Fig. 1.7 shows the geometry of a narrow astigmatic ray tube, i.e. an infinitesimally narrow ray tube surrounding a central ray of direction $\hat{s}$. Corresponding with point O and point P there are the equiphase surfaces $\Psi\,(O)$ and $\Psi\,(P)$, respectively. The reference surface $\Psi\,(O)$ has ρ_1 and ρ_2 as principal radii of curvature. For homogeneous isotropic media, where the rays are straight lines normal to the surfaces of constant phase, the expression of phase continuation along a ray tube is

$$e^{-jk\Psi(P)} = e^{-jk\Psi(O)}e^{-jks} \tag{1.31}$$

and in a similar way, the expression of amplitude continuation is

$$\mathbf{E}\,(P) = \mathbf{E}\,(O)\sqrt{\frac{\rho_1\rho_2}{(\rho_1+s)\,(\rho_2+s)}}e^{-jks} \tag{1.32}$$

with

$$A(s) = \sqrt{\frac{\rho_1 \rho_2}{(\rho_1 + s)(\rho_2 + s)}} \tag{1.33}$$

called spreading factor. It is possible to note that, when $s = -\rho_1$ or $s = -\rho_2$, the GO field prediction diverges and the ray tube converges on a line or a surface. The locus of points where this happens is called caustic. If the assumption of plane wave is made, i.e. the equifase surfaces are planes, the radii of curvature ρ_1 and ρ_2 tend to infinite and, accordingly to Eq. 1.33, $A(s) \to 1$. Then, the GO field, in case of plane wave ray tube, can be written as:

$$\mathbf{E}(P) = \mathbf{E}(O) e^{-jks} \tag{1.34}$$

If a spherical wave is taken in consideration, $\rho_1 = \rho_2 = \rho$. The spreading factor is reduced to

$$A(s) = \frac{\rho}{\rho + s} \tag{1.35}$$

Finally, in lossless homogeneous media, GO fields $\mathbf{E}$ and $\mathbf{H}$ are mutually perpendicular and also perpendicular to $\hat{s}$, thus it is possible to say that they are locally plane even if, in general, they are not necessary uniform plane waves.

1.4.1 Polarization of an electromagnetic wave

The polarization of an electromagnetic wave is a vector that describes the motion in time of the field vector at a fixed point in space [26].

The most generic type of polarization is the elliptical one, where the electric field vector moves along an ellipse in any plane perpendicular to the direction of propagation, that is called plane of polarization. Two possible polarization states can be associated to an elliptical polarization, right-hand or left-hand, depending on the sense of rotation of the electric field. Elliptical polarization can be seen as formed by two vectors with different amplitudes and out of phase by a generic angle δ. In the particular case when the two vectors have equal amplitude and $\delta = \pi/2$, the polarization is said to be circular as the ellipse degenerates into a circle. The most simple type of polarization is linear, i.e. when the electric field moves on a straight line in time. In this case the two cartesian components, in which the field can be decomposed, are in phase.

A common way to express the two components is, accordingly to a spherical coordinate system (see Fig. 1.8), in terms of field along $\hat{\theta}$ and

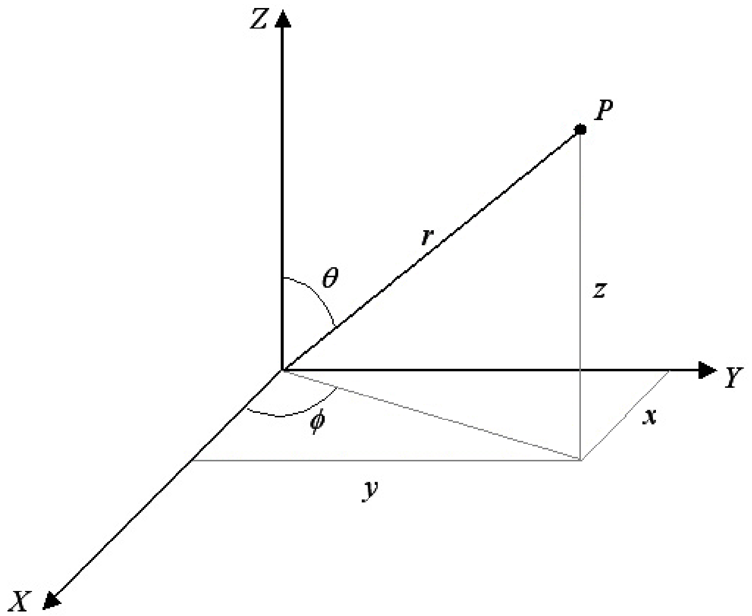

Figure 1.8: Spherical coordinates

along $\hat{\phi}$, that are orthogonal to the direction of propagation ($\hat{\rho}$, in the spherical system).

$$\mathbf{E} = E_\theta \hat{\theta} + E_\phi \hat{\phi} \tag{1.36}$$

The spherical unit vectors can be expressed in terms of cartesian coordinates in the following way:

$$\begin{bmatrix} \hat{\rho} \\ \hat{\theta} \\ \hat{\phi} \end{bmatrix} = \begin{bmatrix} \sin\theta\cos\phi & \sin\theta\sin\phi & \cos\theta \\ \cos\theta\cos\phi & \cos\theta\sin\phi & -\sin\theta \\ -\sin\phi & \cos\phi & 0 \end{bmatrix} \begin{bmatrix} \hat{x} \\ \hat{y} \\ \hat{z} \end{bmatrix} \tag{1.37}$$

A depolarizing medium is one that affects the polarization of the EM wave traveling in it by changing its direction or even its type. In RT depolarization happens mainly as a consequence of an interaction between the wave and a scatterer. Considering the plane containing the vector normal to the scatterer at the scattering point, $\hat{n}$, and the vector representing the direction of propagation, the field can be decomposed in two components, one parallel and the other perpendicular to this plane.

$$\mathbf{E} = E_\perp \hat{e}_\perp + E_\parallel \hat{e}_\parallel \tag{1.38}$$

Accordingly to this decomposition a depolarization matrix

$$[D] = \begin{bmatrix} D_{\perp\perp} & D_{\perp\parallel} \\ D_{\parallel\perp} & D_{\parallel\parallel} \end{bmatrix} \tag{1.39}$$

can be defined to evaluate the field after the interaction. When $D_{\perp\parallel} = D_{\parallel\perp} = 0$ the depolarizing medium is said to be symmetric.

If it is assumed that there is a preferred polarization state, this can be taken as reference. Thus, the field can also be decomposed in terms of the reference polarization state, called copolarized, and its orthogonal state, called cross-polarized.

$$\mathbf{E} = E_{co}\hat{e}_{co} + E_{xp}\hat{e}_{xp} \tag{1.40}$$

According to this decomposition, a figure of merit of the behavior of the propagation channel in terms of polarization can be introduced. It is called Cross-Polarization Discrimination (XPD), it is normally evaluated in dB and it is defined as:

$$XPD|_{\mathrm{dB}} = 10\log_{10}\frac{|E_{co}|^2}{|E_{xp}|^2} \tag{1.41}$$

1.4.2 Antenna fundamentals

An antenna is a device used to radiate or receive radio waves. Radiation is generated by accelerated charges or time-varying currents, thus a radiating antenna is such a device conceived to cause these phenomena in an efficient and desired way. Moreover, taking advantage of the Lorentz reciprocity theorem, antenna characteristics are the same if considered as radiating or receiving.

Antenna properties are defined through a large number of parameters [27]. One of the most important is the **radiation pattern** that is defined as the graphical representation of the radiation properties as a function of the direction in space, in Volts and in terms of (θ, ϕ) coordinates. A radiation pattern cut is the 2-D representation of the intersection between the 3-D pattern and a specific plane. Two orthogonal cuts, e.g. E-plane and H-plane or θ cut and ϕ cut, are normally utilized to describe the radiation properties. The radiation pattern can be isotropic, if the radiation is equal in all the directions, omnidirectional, if the radiation is equal in all directions only in one specific cut, and directional, if the radiation is mainly directed in one specific direction. In Fig. 1.9 an example of omnidirectional pattern is presented.

In a directional radiation pattern, the main lobe is the portion of pattern surrounding the direction of maximum radiation and the side

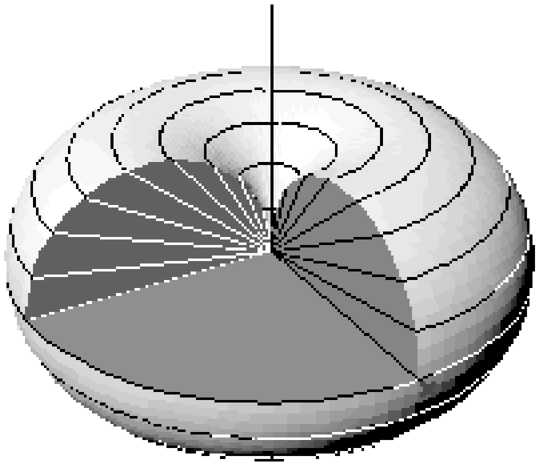

Figure 1.9: Example of a 3-D radiation pattern

lobes are the ones in directions other than the main one. As the side lobes represent radiation in undesired directions, a parameter is defined to express the ratio (in dB) between the biggest side lobe and the main lobe and it is called the **Side Lobe Level**. Another parameter directly related to the pattern is the **Half-Power Beam Width** (HPBW) that is defined as the angle, in a cut that contains the maximum of radiation, between the two directions that have half of the power with respect to the maximum.

The **radiation intensity**

$$U(\theta, \phi) = r^2 S(r, \theta, \phi) \tag{1.42}$$

where S is the Poynting vector, represents the power radiated per solid angle. The **directivity** is the ratio between the radiation intensity in a generic direction and the radiation intensity U_0 of an isotropic antenna with the same total radiated power, taken as reference. Thus, it follows:

$$D(\theta, \phi) = \frac{U(\theta, \phi)}{U_0} = \frac{4\pi U(\theta, \phi)}{P_{rad}} \tag{1.43}$$

where P_{rad} is the total radiated power. The **efficiency** e of an antenna is the ratio between the total radiated power and the power absorbed, thus it is a metric that takes into account the losses of the antenna system. A parameter similar to the directivity is the **gain**, that is defined as the ratio between the radiation intensity in a generic direction and the radiation intensity in case the absorbed power is radiated isotropically.

It follows that

$$G(\theta, \phi) = eD(\theta, \phi) \tag{1.44}$$

The **effective area** of a receiving antenna is a metric to evaluate the capability to capture the power of the impinging wave. It is defined as the ratio between the available power at the receiving antenna and the power density of the plane wave impinging from a specific direction.

$$A_e(\theta, \phi) = \frac{P_r}{S_i(r, \theta, \phi)} \tag{1.45}$$

The (maximum) effective area is related to the (maximum) directivity, D_0, in the following way:

$$A_{em} = e\frac{\lambda^2}{4\pi}D_0 \tag{1.46}$$

Let's consider a transmitting antenna and a receiving one that is placed in the far field of the transmitting one,

$$r > \frac{2D^2}{\lambda} \tag{1.47}$$

where D is the maximum dimension of either of the two antennas. The transmitted power density is:

$$S_t(r, \theta_t, \phi_t) = e_t\frac{P_t D_t(\theta_t, \phi_t)}{4\pi r^2} \tag{1.48}$$

while the effective area of the receiving antenna is:

$$A_r(\theta, \phi) = e_r D_r(\theta_r, \phi_r) \tag{1.49}$$

Then, the received power is just $S_t A_r$. From this considerations it follows the well-known Friis Equation:

$$\frac{P_r}{P_t} = G_t(\theta_t, \phi_t) G_r(\theta_r, \phi_r)\left(\frac{\lambda}{4\pi r}\right)^2 \tag{1.50}$$

The free space pathloss, already presented in Section 1.1.1, derives directly from this equation.

The **polarization** of a transmitting antenna in a given direction is the polarization of the wave transmitted in that direction by the antenna, while the polarization of a receiving antenna is the one of a plane wave incident from a given direction that yields the maximum available power at the antenna terminals [26]. By reciprocity, the polarization properties of an antenna are the same if it is employed for transmitting or receiving purposes. It is important to underline that the polarization properties of an antenna may change significantly depending on the direction of radiation (or reception) and the nominal polarization is only the one in the direction of maximum radiation. The polarization mismatch factor is defined as:

$$\eta_p = |\hat{\rho}_t \cdot \hat{\rho}_r^*|^2 \tag{1.51}$$

where $\hat{\rho}_t$ is the polarization of the impinging wave on the receiving antenna and $\hat{\rho}_r$ is the polarization of the receiving antenna in the direction of the impinging wave.

Additional losses are due to reflections generated by the mismatch between the antenna and the transmission line which feeds the antenna. The impedance mismatch factor is defined as:

$$\eta_i = \left(1 - |\Gamma_t|^2\right)\left(1 - |\Gamma_r|^2\right) \tag{1.52}$$

where Γ is the voltage reflection coefficient.

Then, a more general form of Eq. 1.50 can be written as:

$$\frac{P_r}{P_t} = G_t\left(\theta_t, \phi_t\right) G_r\left(\theta_r, \phi_r\right) \left(\frac{\lambda}{4\pi r}\right)^2 \eta_p \eta_i \tag{1.53}$$

The **bandwidth** of an antenna is the range of frequencies around the nominal one for which its characteristics (e.g. input impedance, pattern, beamwidth) fullfill its specifications, i.e. the values are within an acceptable value of the nominal ones.

1.5 State of the art in Ray-Tracing

RT is probably the most common deterministic propagation tool. It is less complex than electromagnetic full-wave methods, but more accurate than a simple empirical model. In this section, an overview of the state of the art of RT is presented.

The intrinsic characteristics of a RT algorithm invest this tools with a high degree of flexibility towards the application scenario. In literature it is possible to find several contributions both for outdoor [28, 29, 30, 31, 32, 33, 34, 35], and indoor scenarios [36, 37, 38, 39, 40, 41, 42].

The most simple RT tools are the 2-D ones [42], where the propagation is assumed to take place in a single plane, e.g. the horizontal or azimuth plane. If the transmitting and receiving antennas are at the same height and only a rough analysis of the channel characteristics is needed, this could be already a sufficient approximation. The following step consists in hybrid techniques where the tracing of rays in vertical and horizontal 2-D planes is combined to produce 3-D paths [28, 36]. Often also launching techniques, described already in Section 1.1.3, are referred to as RT [29, 34]. The most common implementation is, in any case, the full 3-D RT, where propagation is described in the whole environment under investigation, interactions can happen in the 3-D space and 3-D antenna radiation patterns are employed.

Another point that may differentiate RT implementations is the basic element used to describe the environment, i.e. buildings in outdoor scenarios or walls and furniture in indoor scenarios. For example, [37] and [38] use facets, while in [43] polygons are used. In the RT tool described in this thesis, the basic element is a rectangular parallelepiped, that may represent a building in outdoor scenarios and a 3-D wall or the horizontal surface of a table in indoor scenarios.

Concerning the type of interactions implemented, all algorithms are based on GO and UTD and consequently consider reflection and diffraction in addition to LOS propagation. Tools that are used in indoor scenarios have implemented also penetration or wall transmission. Most advanced RT tools also include a model for diffuse scattering. The most common is the one presented in [44], that is implemented in [29, 30, 32] in outdoor scenarios or in [38] in indoor scenarios. Another possible implementation is the one of [39], where diffuseness is generated by randomly distributed scattering points. In [45], scattering by vegetation elements is also included in the interactions implemented in a RT tool.

In principle, the output of a 3-D RT algorithm is able to provide any type of information on the channel: narrow and wide band, electromagnetic and statistic, static and mobile. A brief overview of what kind of results can be found in literature is now presented. Pathloss or received power prediction is the common base of nearly all the works on RT. The capabilities of these tools to predict it accurately is therefore well established. If the focus is kept on narrowband characteristics, much less explored with RT is the polarization behavior of the channel. In [36] pathloss in cross-polar channels is investigated in an indoor scenario, apparently providing even better accuracy than in co-polar ones. In [46] the importance to implement diffuse scattering to correctly predict the polarization behavior of the channel is proven in an outdoor scenario and in [29] it is validated while predicting the performance of a polarization MIMO system.

Moving to wideband channel characteristics, RMS delay spread is a very common metric estimated using RT. Some examples are [31, 32, 33, 35] in outdoor scenarios and [36, 40, 41] in indoor scenarios. RT is generally less accurate in predicting this metric. The limited number of interactions that can be implemented, to have a reasonable computation time, together with the limitation of the area modeled within the tool tend to generate delay spreads that underestimate the values extracted from measurements used for validation. Power delay profiles can also be put in comparison between simulations and measurements [28, 33, 36, 40].

While angular characteristic of the channel can be easily determined with a 3-D RT algorithm, the validation of such metric with measurement is quite complex. It needs the use of ad-hoc measurement campaigns and high-resolution algorithms to extract the directional properties of the channel. Works that present this kind of analysis are [30, 32, 41, 47]. Due to the limitations of the scenario database modeling, RT shows a reduced richness concerning multi-path propagation with respect to actual propagation. For this reason also angular properties represent a critical metric to predict with such tools.

As anticipated, RT is able to determine also the characteristics of a mobile channel. An example can be found in [30] where Doppler shift, Doppler spread and fading distribution are predicted and validated. Statistical performances of a communication channel can also be evaluated from RT simulations. In [42] RT is used to estimate the capacity of a MIMO wireless system. In [39] BER of a MIMO multiband OFDM system is computed from measurements and simulations; when compared, the results show good agreement.

RT tools are also used in the study of emerging communication technologies. Some examples are:

- vehicular communications: in [48] car-to-car propagation is simulated to test antenna placements on vehicles,
- THz communications: in [49] RT simulations are compared with measurements at the frequency of 300 GHz,
- UWB communications: in [43] and [50] RT simulations at different frequency points are superimposed to model wide band channel properties.

1.6 Thesis contributions

The starting point of this thesis was a pre-existent RT software [1] which included LOS propagation, multiple reflection and diffraction and that was used to predict propagation behavior in outdoor scenarios. The goal of this work was to enhance its prediction capabilities implementing new propagation mechanisms, e.g. penetration, diffuse scattering and scattering by vegetation elements and, thus, significantly widening the application possibilities. The core of this thesis concerns the parameterization and validation of the advanced RT tool in different scenarios, both indoor and outdoor, and for different propagation metrics.

The contribution of this thesis can be summarized in the following points:

1. The parameterization of the diffuse scattering model in two indoor environments, a warehouse and a typical office. Despite the fact that its usage in indoor scenario is not novel, a thorough study of the behavior of diffuse scattering parameters is quite a novelty in such scenarios. Together with this, the prediction accuracy of the enhanced version of the RT tool, including penetration and diffuse scattering, is validated versus measurements, in terms of delay and polarization characteristics of the channels.

2. The parameterization of diffuse scattering in an outdoor campus scenario in terms of received power and its validation with measurement focusing on the polarization behavior of the channel.

3. One of the characteristics of diffuse scattering is its importance to accurately predict the polarization behavior of the channel. Nevertheless, at first, the model did not include any specific polarization model. In collaboration with the propagation group of University of Bologna, such a model is derived, parameterized and validated with measurements. The starting point is a campaign of ad-hoc measurements in single building outdoor scenarios, where scattering contributions can be separated from coherent components. Analyzing the extracted diffuse components leads to the derivation of the polarization model and its parameterization, depending on the characteristics of the building façade. Then, the diffuse scattering polarization model is validated with measurements in two different outdoor scenarios, the already presented campus scenario and a pedestrian street canyon scenario.

4. A novel model for scattering by vegetation elements is developed to take into account the presence of trees in outdoor environments. This intuitive and fast, in terms of computation time, ray-based model has been thought to be easily implemented in a RT tool. The model is parameterized and validated in the campus scenario, where it is employed together with empirical attenuation models for propagation in vegetation. A first attempt to extend the scattering by vegetation model with polarization behavior is also carried out.

5. Among the capabilities of a 3-D RT tool is the ability to intrinsically provide directional properties of the channel. Despite the fact that in literature it is possible to find comparison between RT and high-resolution parameter extraction results for coherent components, in this thesis, in collaboration with Université Libre de Bruxelles, the effort is focused in predicting the angular properties of diffuse scattering. In addition to this, the cluster behavior of the scattering component and its relationship with specular clusters can also be investigated with RT. This means that it is possible to use a RT prediction tool to replace measurements for parameterization of GSCMs.

1.7 Thesis outline

Chapter 2 describes the implementation of the propagation mechanisms that are used to simulate the interactions of rays with the environment in RT. Interaction types already present in the original version, e.g. reflection and diffraction, and newly implemented, e.g. penetration, diffuse scattering and contributions by vegetation, are described.

In Chapter 3, channel sounding techniques and architectures are discussed together with RT practical details, such as the computation time and the evaluation of errors with respect to measurements.

Chapter 4, on indoor RT simulations, is divided in two main parts. In the first part the prediction capabilities in terms of polarization and delay behavior of the channel are validated in two indoor scenarios: a warehouse and an office. In the second part the directional properties of the channel, with a specific focus on the ones of diffuse scattering, are tested comparing RT simulations and parameters extracted from measurements with a high resolution algorithm.

Chapter 5 is about the parameterization and validation of RT in an outdoor campus environment. Given the presence of trees in the scenario, the ad-hoc method to evaluate scattering by vegetation elements is tested in this scenario.

In Chapter 6, a polarization model for diffuse contributions scattered off building walls is proposed. The parameterization of the simple but effective model is done in ad-hoc single building scenarios. The model is then validated in two outdoor environments: a campus scenario and a street canyon.

Finally, Chapter 7 presents three examples of practical application or the advanced RT tool carried out during this thesis: simulations for localization purposes in indoor scenarios, simulations for the development of an algorithm for radio surveillance in industrial scenarios and the study of propagation in an airport environment.

2

Improved implementation of propagation mechanisms

In this chapter, we describe the implementation of the propagation mechanisms that are used to simulate the interactions of rays with the environment. This particular implementation of RT is written in C language to be run on UNIX stations.

The starting point was a classic 3-D RT software [1] that was taking into account line of sight propagation, specular reflection and diffraction. It was used to predict wide and narrow band propagation characteristics in outdoor scenarios. To enhance the prediction capabilities of the tool, several new features have been implemented, in particular diffuse scattering and penetration.

RT geometry is based on a cartesian coordinate system and the simulation environment is generated using perpendicular parallelepipeds. The input parameters of the tool are:

- frequency,
- position in space of transmit and receive antennas,
- 3-D radiation patterns of transmit and receive antennas,
- 3-D coordinates of the blocks simulating the propagation environment,
- permittivity and conductivity of the materials in the environment,
- parameters concerning the different propagation mechanisms, e.g. reflection order, scattering coefficients...

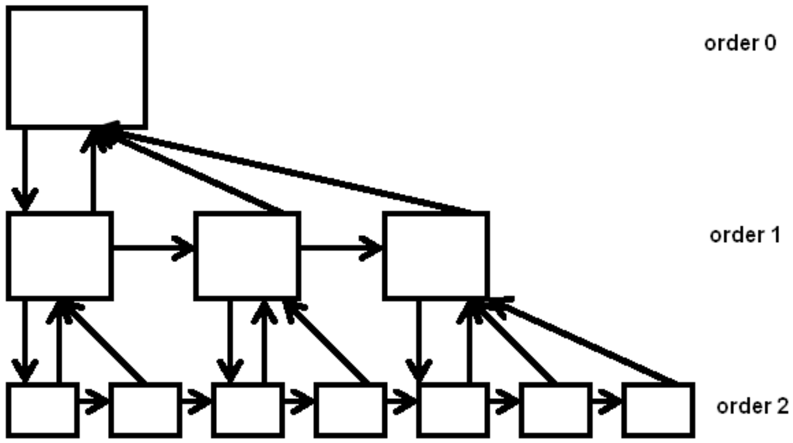

Figure 2.1: Scheme of the tree of images generation

2.1 Specular reflection

Specular reflection from a flat surface is implemented in RT following the method of image (see Section 1.1.3). In the first part of the code, a tree structure containing all the images is created. The root node of the structure is the position of the transmitter. The depth of the tree is set by the maximum order of reflection allowed. As first step, the images of the transmitter are generated with respect to each block surface visible by the source point, i.e. with normal unit vector facing towards the transmitter. These images are the nodes of first order. At order i, with $i > 1$, the images of the images of order $i - 1$ are generated in a similar way. At any order $i > 0$ each node is connected through a pointer to the *mother* node of order $i - 1$ from which it was generated and through another pointer to the following node of the same order, if there is any other. Moreover, at any order i excluding the last one, each node is connected through an additional pointer to the first node of order $i + 1$ that it generated. A simple scheme of the tree of images structure is presented in Fig. 2.1.

Once the tree is constructed, for each reflection order $i = 1, \dots, i_{max}$, with i_{max} maximum order of reflection, the rays are traced backwardly starting from each node of the tree at level i and until the root node is met. Each reflection point, relative to a certain node of the tree, is found by intersecting the line connecting the image point stored in that node and the destination point, i.e. either the receiver or a reflection point of the following order found at the precedent iteration, with the surface related to that node, i.e. to that image point.

According to Eq. 1.32 it is possible to write the GO reflected field at an observation point P with respect to the reflected field at the specular reflection point Q_r as:

$$\mathbf{E}(P) = \mathbf{E}_r(Q_r)\sqrt{\frac{\rho_{1r}\rho_{2r}}{(\rho_{1r}+s_r)(\rho_{2r}+s_r)}}e^{-jks_r} \tag{2.1}$$

where ρ_{1r} and ρ_{2r} are the radii of curvature of the reflected ray tube with reference Q_r and s_r is the distance between the reflection point and the observation point. In the hypothesis of incident spherical wave $\rho_{1i} = \rho_{2i} = s_i$, where s_i is the distance between the reference point and the reflection point. Moreover, considering that a flat surface has infinite radius of curvature $a = \infty$, it follows that $\rho_{1r} = \rho_{1i}$ and $\rho_{2r} = \rho_{2i}$. Then the spreading factor of the GO reflected field from a flat surface is reduced to:

$$A(s_i, s_r) = \frac{s_i}{s_i + s_r} \tag{2.2}$$

Reflection can be easily described adopting a ray-fixed coordinate system, in which the field is decomposed in two components: one parallel and the other perpendicular to the plane of incidence. The parallel unit vectors that identify the corresponding components can be evaluated, for the incident and reflected case respectively, as follows:

$$\hat{e}_{i\parallel} = \frac{\hat{s}_i \times (\hat{n} \times \hat{s}_i)}{|\hat{s}_i \times (\hat{n} \times \hat{s}_i)|} \tag{2.3}$$

and

$$\hat{e}_{r\parallel} = \frac{\hat{s}_r \times (\hat{n} \times \hat{s}_r)}{|\hat{s}_r \times (\hat{n} \times \hat{s}_r)|} \tag{2.4}$$

where $\hat{s}_i$ is the impinging wave direction, $\hat{s}_r$ is the direction of specular reflection and $\hat{n}$ is the unit vector perpendicular to the surface at the reflection point. Consequently, the perpendicular unit vectors can be evaluated as:

$$\hat{e}_{i\perp} = \hat{s}_i \times \hat{e}_{i\parallel} \tag{2.5}$$

and

$$\hat{e}_{r\perp} = \hat{s}_r \times \hat{e}_{r\parallel} \tag{2.6}$$

Considering that, according to the law of reflection, the reflected ray lies in the plane of incidence, i.e. the one containing the incident ray and the normal to the surface at the reflection point, it follows that $\hat{e}_{i\perp} = \hat{e}_{r\perp} = \hat{e}_{\perp}$.

Then, the GO reflected field at Q_r can be simply put in relation to the incident GO field at Q_r through the dyadic reflection coefficient $\overline{\overline{\mathbf{R}}}$

in the following way:

$$\mathbf{E}_r\left(Q_r\right) = \overline{\mathbf{R}} \cdot \mathbf{E}_i\left(Q_r\right) \tag{2.7}$$

The dyadic coefficient is a concise notation that includes the decomposition of the field in the ray-fixed coordinate system and the multiplication by the relative interaction coefficients. It can be written as [1]:

$$\overline{\mathbf{R}} = \hat{e}_{i\parallel}\hat{e}_{r\parallel}R_{\parallel} + \hat{e}_{\perp}\hat{e}_{\perp}R_{\perp} \tag{2.8}$$

The Fresnel reflection coefficients for the parallel and perpendicular components are:

$$R_{\parallel} = \frac{\epsilon_e \cos\theta_i - \sqrt{\epsilon_e - \sin^2\theta_i}}{\epsilon_e \cos\theta_i + \sqrt{\epsilon_e - \sin^2\theta_i}} \tag{2.9}$$

and

$$R_{\perp} = \frac{\cos\theta_i - \sqrt{\epsilon_e - \sin^2\theta_i}}{\cos\theta_i + \sqrt{\epsilon_e - \sin^2\theta_i}} \tag{2.10}$$

where θ_i is the angle of incidence and the effective permittivity ϵ_e is defined as in Eq. 1.24. Thus, according to Eq. 1.39, the depolarization matrix for reflection interaction can be written as:

$$[R] = \begin{bmatrix} R_{\perp} & 0 \\ 0 & R_{\parallel} \end{bmatrix} \tag{2.11}$$

2.2 Specular reflection on a curved surface

The core of the RT tool is the image database construction, that considers the environment formed by perpendicular parallelepipeds with flat surfaces. In addition to that, for a limited number of cases representing objects with a curved surface that cannot be represented as parallelepipeds, specular reflection on a smooth curved surface is implemented.

The starting point is Eq. 2.1 that is always valid, thus also for a curved surface. Considering a spherical impinging wave, $\rho_{1i} = \rho_{2i} = s_i$ holds true. The radii of curvature of the reflected ray tube, on the other hand, have to be calculated according to the surface under examination.

Let us consider a smooth portion of a 3D surface. At each point Q it is possible to define a set of principal planes, a pair of principal directions and a normal unit vector $\hat{n}$. The radii of curvature of the surface in these planes at Q are called principal radii of curvature at Q and are denoted as a_1 and a_2. A curve at Q may have different curvatures, depending on the normal plane that is taken in consideration. The

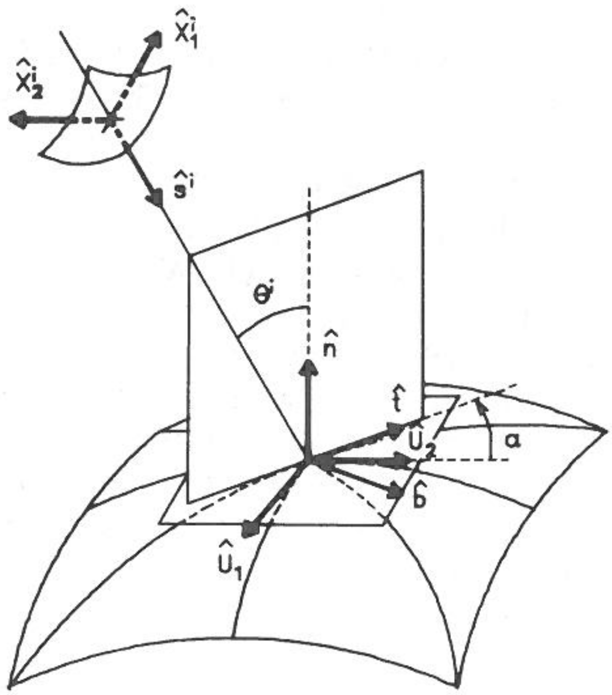

Figure 2.2: Surface-fixed coordinate system for reflection on a curved surface [18]

principal radii of curvatures are the minimum and maximum ones and the corresponding principal directions are perpendicular to each other. The principal direction unit vectors are denoted as $\hat{U}_1$ and $\hat{U}_2$. This surface-fixed coordinate system is shown in Fig. 2.2.

According to [18], for spherical wave incidence, the principal radii of curvature of the reflected wave can be evaluated as follows:

$$\frac{1}{\rho_{r1}} = \frac{1}{s_i} + \frac{1}{f_1} \tag{2.12}$$

$$\frac{1}{\rho_{r2}} = \frac{1}{s_i} + \frac{1}{f_2} \tag{2.13}$$

where

$$\frac{1}{f_{1,2}} = \frac{1}{\cos\theta_i}\left[\frac{\sin^2\theta_2}{a_1} + \frac{\sin^2\theta_1}{a_2}\right] \pm \pm\sqrt{\frac{1}{\cos^2\theta_i}\left[\frac{\sin^2\theta_2}{a_1} + \frac{\sin^2\theta_1}{a_2}\right]^2 - \frac{4}{a_1 a_2}} \tag{2.14}$$

It is clear to see that if $a_1 = a_2 \to \infty$ then $1/f_{1,2} \to 0$ and $\rho_{1r} = \rho_{2r} = s_i$, going back to the flat surface case. The angles θ_1 and θ_2 are the ones between the plane of incidence and the principal directions.

$$\theta_1 = \cos^{-1}\left(-\hat{n}\cdot\hat{U}_1\right) \tag{2.15}$$

$$\theta_2 = \cos^{-1}\left(-\hat{n}\cdot\hat{U}_2\right) \tag{2.16}$$

They can be expressed in terms of θ_i as it follows:

$$\sin^2\theta_1 = \cos^2\alpha + \sin^2\alpha\cos^2\theta_i \tag{2.17}$$

$$\sin^2\theta_2 = \sin^2\alpha + \cos^2\alpha\cos^2\theta_i \tag{2.18}$$

The angle α is the one between the plane of incidence and one of the principal planes of the surface at the reflection point Q_r and it is such that $\cos\alpha = \hat{U}_2\cdot\hat{t}$. The other tangent vector at Q_r, $\hat{b}$ is:

$$\hat{b} = \hat{t}\times\hat{n} = -\hat{n}\times\hat{s}_i \tag{2.19}$$

2.3 Diffraction

Three dimensional wedge diffraction [18] is also implemented in the RT tool in terms of UTD (see Section 1.2.3) and in the approximation of an infinite wedge. Only single interaction is considered.

As first step, all the wedges that are visible from the source point are stored in a database. For each wedge, which internal angle is α and external angle is $n\pi$, the program tries to determine the diffraction point Q_d. Following the law of diffraction, the angle β_{0i} formed by the incident ray with the edge is equal to the angle β_{0r} between the diffracted ray and the edge.

$$\beta_{0i} = \beta_{0r} = \beta_0 \tag{2.20}$$

The geometry for the determination of the diffraction point is shown in Fig. 2.3. By projecting the impinging and the diffracted ray on the edge, the similar triangles $\widehat{T_xQ_dA}$ and $\widehat{R_xQ_dB}$ are created. By this means, the line segments $\overline{AQ_d}$ and $\overline{BQ_d}$ can be determined and consequently the location of the point Q_d is found.

At this point, the UTD diffracted field can be evaluated. To simplify the calculations, an edge-fixed coordinate system has to be defined. The incident field is decomposed into $\hat{\beta}_0$ and $\hat{\xi}$ components, where ξ is the angle between one of the two faces of the wedge, taken as reference and called o-face, and the considered ray. If $\hat{t}$ is the unit vector tangential

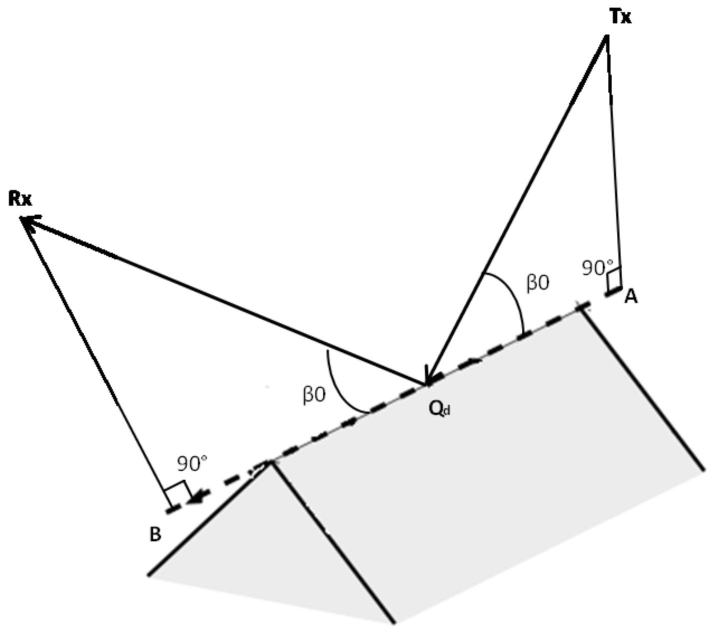

Figure 2.3: Geometry for the determination of the diffraction point

to the edge, $\hat{s}_i$ is the incidence direction and $\hat{s}_d$ is the diffracted ray direction, $\hat{\beta}_0$ and $\hat{\xi}$ can be evaluated as follows:

$$\hat{\xi}_i = \frac{\hat{s}_i \times \hat{t}}{\left|\hat{s}_i \times \hat{t}\right|} \tag{2.21}$$

$$\hat{\xi}_d = \frac{\hat{t} \times \hat{s}_d}{\left|\hat{t} \times \hat{s}_d\right|} \tag{2.22}$$

$$\hat{\beta}_{0i} = \hat{\xi}_i \times \hat{s}_i \tag{2.23}$$

$$\hat{\beta}_{0d} = \hat{\xi}_d \times \hat{s}_d \tag{2.24}$$

An example of edge-fixed coordinate system for diffraction on a 3-D wedge is shown in Fig. 2.4.

The diffracted field can be written as [22]:

$$\mathbf{E}_d\left(s\right) = \mathbf{E}_d\left(O\right)\sqrt{\frac{\rho_{1d}\rho_{2d}}{\left(\rho_{1d}+s\right)\left(\rho_{2d}+s\right)}}e^{-jks} \tag{2.25}$$

where $\rho_{1,2d}$ are the radii of curvature of the diffracted wave and O is the reference point from where the distance s originates (see Fig. 2.5). It

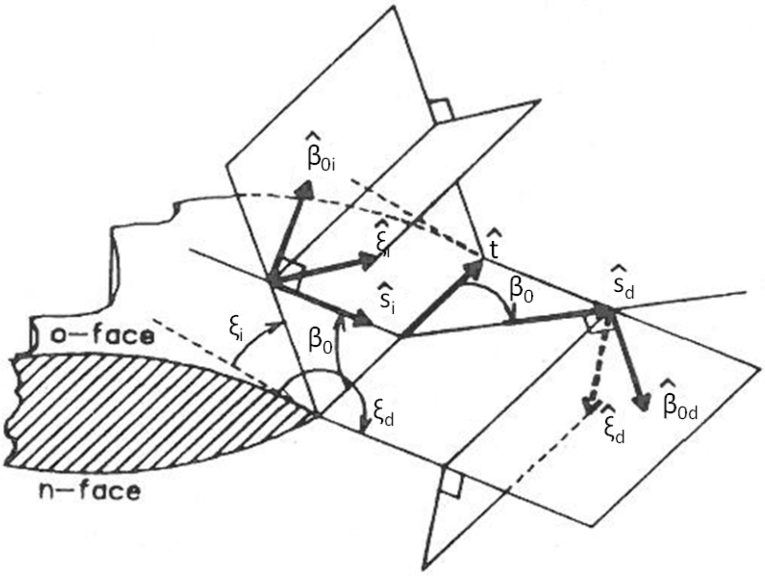

Figure 2.4: Edge-fixed coordinates geometry [18]

is possible to note that the wedge is a caustic, i.e. $\mathbf{E}_d\left(s=-\rho_{2d}\right)\rightarrow\infty$. For convinience, the reference point O is chosen to coincide with the diffraction point Q_d. As the diffracted field must be independent from the location of the reference point, $\lim_{\rho_{2d}\rightarrow 0}\mathbf{E}_d\left(O\right)\sqrt{\rho_{2d}}$ exists and, as the diffracted field is proportional to the incident field at the diffraction point, it is possible to write:

$$\lim_{\rho_{2d}\rightarrow 0}\mathbf{E}_d\left(O\right)\sqrt{\rho_{2d}}=\overline{\mathbf{D}}\cdot\mathbf{E}_i\left(Q_d\right) \tag{2.26}$$

where $\overline{\mathbf{D}}$ is the dyadic UTD diffraction coefficient, a concise notation to express the decomposition of the field in linear components and the relative interaction coefficients.

If a spherical incident wavefront is considered, $\rho_{1d}=s_i$ and the observation point P is at a distance s_d from the diffraction point, the edge-diffracted field can be evaluated in the following way [51]:

$$\mathbf{E}_d\left(P\right)=\overline{\mathbf{D}}\cdot\mathbf{E}_i\left(Q_d\right)\sqrt{\frac{s_i}{s_d\left(s_d+s_i\right)}}e^{-jks_d} \tag{2.27}$$

The dyadic UTD diffraction coefficient is:

$$\overline{\mathbf{D}}=-\hat{\beta}_{0i}\hat{\beta}_{0d}D_\beta-\hat{\xi}_i\hat{\xi}_d D_\xi \tag{2.28}$$

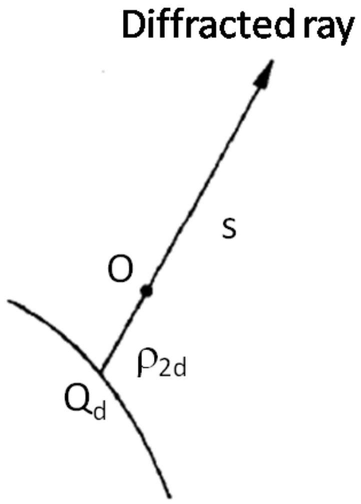

Figure 2.5: Edge diffracted ray

where

$$D_\beta = D_1 + D_2 + R_\parallel \left(D_3 + D_4\right) \tag{2.29}$$

and

$$D_\xi = D_1 + D_2 + R_\perp \left(D_3 + D_4\right) \tag{2.30}$$

The four terms that form the diffraction coefficients can be evaluated in the following way:

$$D_1 = \frac{-e^{-j\pi/4}}{2n\sqrt{2\pi k}\sin\beta_0} \cot\left(\frac{\pi + (\xi_d - \xi_i)}{2n}\right) F\left(kLa^+\left(\xi_d - \xi_i\right)\right) \tag{2.31}$$

$$D_2 = \frac{-e^{-j\pi/4}}{2n\sqrt{2\pi k}\sin\beta_0} \cot\left(\frac{\pi - (\xi_d - \xi_i)}{2n}\right) F\left(kLa^-\left(\xi_d - \xi_i\right)\right) \tag{2.32}$$

$$D_3 = \frac{-e^{-j\pi/4}}{2n\sqrt{2\pi k}\sin\beta_0} \cot\left(\frac{\pi + (\xi_d + \xi_i)}{2n}\right) F\left(kLa^+\left(\xi_d + \xi_i\right)\right) \tag{2.33}$$

$$D_4 = \frac{-e^{-j\pi/4}}{2n\sqrt{2\pi k}\sin\beta_0} \cot\left(\frac{\pi - (\xi_d + \xi_i)}{2n}\right) F\left(kLa^-\left(\xi_d + \xi_i\right)\right) \tag{2.34}$$

Functions $a^\pm$ are defined as

$$a^\pm\left(\xi_d \pm \xi_i\right) = 2cos^2\left(\frac{2n\pi N^\pm - (\xi_d \pm \xi_i)}{2}\right) \tag{2.35}$$

where $N^{\pm}$ are the integer that most nearly satisfy the equation:

$$2\pi n N^{\pm} - (\xi_d \pm \xi_i) = \pm\pi \tag{2.36}$$

$F(x)$ is the transition function that forces the GTD diffracted fields to remain bounded across the shadow boundaries, as it goes to zero in the same way as the GTD diffraction coefficients become singular.

$$F(x) = 2j\sqrt{x}e^{jx}\int_{\sqrt{x}}^{\infty} e^{-ju^2}du \tag{2.37}$$

Finally the parameter L, for a spherical wavefront, is:

$$L = \frac{s_i s_d}{s_i + s_d}\sin^2\beta_0 \tag{2.38}$$

2.4 Diffuse scattering

It is evident that, when we are dealing with real propagation scenarios, it is uncommon to find a perfectly smooth surface. Moreover, in classical urban or indoor scenarios it is not always possible to determine, even if only statistically, the roughness of a surface. If we also consider that diffuse scattering may arise also in case of smooth interface when the medium is inhomogeneous or layered (volume scattering), it is possible to conclude that a classic solution for scattering by a rough surface may not be suitable to be implemented in a RT tool. Another important issue for RT is the accuracy of the input database that describes the propagation environment. Not everything can be modeled and increasing the number of objects included affects significantly the computation time.

Combining all these points, it is possible to conclude that a model would be needed that parameterizes not only the roughness but also all the other deviations from the ideality represented by a database constituted by smooth surfaces, i.e. irregularities, inhomogeneities and small objects that cannot be modeled in the input database. The physics-based heuristic diffuse scattering model developed by the propagation group of University of Bologna defines an effective roughness [52] that takes into account all these characteristics.

2.4.1 Diffuse scattering vs. DMC

Before going through the implementation of the model itself, it may be important to spend few words on what is called Dense Multipath Component (DMC) and its relation with diffuse scattering. DMC is defined, from the experimental parameter extraction viewpoint, as the part of the channel that cannot be characterized by coherent components [53]. It is, in fact, obtained by subtracting the coherent part of the channel, evaluated with high-resolution algorithms (see Section 3.3), from the measured power delay profile. Recently, a lot of work has been done in characterizing DMC and it has been shown that it often represents a significant part of the transmitted power in wireless communications, for both outdoor [54] and indoor [55] environments. In conclusion, it is possible to say that DMC and diffuse scattering are two different definitions that aim to model the same phenomenon, the non-coherent part of the received signal. This contribution is both dense (a higher number of rays than the coherent ones) and diffuse (spread out wider than coherent rays both in time and space). Thus, it might be relevant to put in comparison these two models to assess the prediction capabilities of the diffuse scattering implementation.

2.4.2 The UniBo model for diffuse scattering

The implementation and the description of the effective roughness model for diffuse scattering [44] is presented in this section.

RT is a discrete model where the basic entity is a ray. Given this assumption, the diffuseness cannot be created in a continuous way but only adopting a discretization of the surfaces. Diffuse scattering is generated by dividing a surface into surface elements or tiles. A diffuse scattering ray is assumed to originate from the center of each surface element. The maximum size of each tile is set by the well known far-field condition [56]:

$$r > \frac{2D^2}{\lambda} \tag{2.39}$$

where r is the distance between the center of the element and the terminal and D is the dimension of the surface element. The discretization is obtained in the software by recursively dividing a surface until it meets this far-field condition. A rectangular surface is divided into four equal rectangles having in common the center of the original rectangle, unless the height of the rectangle is twice or more its width or viceversa. In this second case the rectangle is just divided vertically or horizontally, as exemplified in Fig. 2.6. For each new tile created, the far-field condition is checked again. It may be possible that the surface elements closer to the virtual transmitter do not meet this condition but the further ones do, leading to a subdivision of a surface into elements of different sizes.

A scattering coefficient S and a scattering pattern model are associated with each surface. The reflection reduction factor, R, sets the amount of energy subtracted by scattering from the specular reflection.

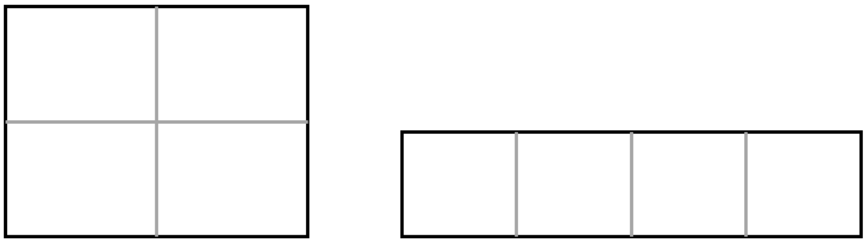

Figure 2.6: An example of subdivision of a normal tile on the left and of a tile whose width is more than twice its height on the right

The definition of the scattering coefficient implemented in this work is

$$S = \left.\frac{|\mathbf{E}_s|}{|\mathbf{E}_r|}\right|_{dS} \tag{2.40}$$

Following this definition, R can be evaluated as

$$R = \sqrt{1 - S^2} \tag{2.41}$$

The pattern models allow to estimate the amplitude of the scattered field. As the scattered wave is assumed incoherent, its phase is generated randomly with an uniform distribution.

Three possible patterns are associated with the effective roughness scattering model:

1. a Lambertian model, with the maximum in the direction perpendicular to the surface
2. a directive model, with the maximum in the direction of specular reflection
3. a backscattering model, similar to the directive model, but including a lobe towards the incident direction

Lambertian model

The radiation lobe of the Lambertian model has its maximum in the direction perpendicular to the surface. The amplitude of the scattered field from a surface element is

$$E_s^2 = K_0^2 S^2 \Gamma^2 \frac{dS \cos\theta_i \cos\theta_s}{\pi} \frac{1}{r_i^2 r_s^2} \tag{2.42}$$

where K_0 is a coefficient depending on the gain of the transmitting antenna and the transmitted power, Γ is the reflection coefficient, θ_i is the angle of incidence and θ_s is the angle of scattering direction.

Directive model

In the directive model, the scattering lobe is steered towards the direction of specular reflection. To achieve this it is possible to write the following expression for the amplitude of the scattered field from a surface element:

$$E_s^2 = E_{s0}^2 \cdot \left(\frac{1+\cos\psi_r}{2}\right)^{\alpha_r} \qquad \alpha_r = 1,\ldots,N \tag{2.43}$$

where ψ_r is the angle between the specular reflection direction and the scattering direction and α_r is a parameter that sets the width of the scattering lobe. The higher α_r, the narrower the lobe. The expression of the maximum amplitude E_{s0} is

$$E_{s0}^2 = K_0^2 S^2 \Gamma^2 \frac{dS\cos\theta_i}{F_{\alpha_r}} \frac{1}{r_i^2 r_s^2} \tag{2.44}$$

where

$$F_{\alpha_r} = \frac{1}{2^{\alpha_r}} \cdot \sum_{j=0}^{\alpha_r} \left(\begin{array}{c}\alpha_r\\ j\end{array}\right) \cdot I_j \tag{2.45}$$

I_j is then defined as:

$$I_j = \begin{cases} \frac{2\pi}{j+1} & \text{if } j \bmod 2 = 0 \\ \frac{2\pi}{j+1}\cdot f(\theta i) & \text{if } j \bmod 2 \neq 0 \end{cases} \tag{2.46}$$

and

$$f(\theta i) = \cos\theta_i \cdot \sum_{\omega=0}^{\frac{j-1}{2}} \left(\begin{array}{c}2\omega\\ \omega\end{array}\right) \cdot \frac{\sin^{2\omega}\theta_i}{2^{2\omega}} \tag{2.47}$$

Backscattering model

This model is similar to the directive one, but with an additional term that takes into account the backscattering phenomenon. In presence of large irregularities, such as balconies and columns, a peak in the scattering radiation may arise even in the incidence direction. The expression that describes this model is:

$$\begin{gathered} E_s^2 = E_{s0}^2 \cdot \left[\Lambda\left(\tfrac{1+\cos\psi_r}{2}\right)^{\alpha_r} + (1-\Lambda)\left(\tfrac{1+\cos\psi_i}{2}\right)^{\alpha_i}\right] \\ \alpha_i, \alpha_r = 1,\ldots,N;\ \Lambda \in [0,1] \end{gathered} \tag{2.48}$$

where α_i sets the width of the backscattering lobe and Λ is the repartition factor between the amplitudes of the two lobes. The expression of the maximum amplitude E_{s0} is

$$E_{s0}^2 = K_0^2 S^2 \Gamma^2 \frac{dS\cos\theta_i}{F_{\alpha_i,\alpha_r}} \frac{1}{r_i^2 r_s^2} \tag{2.49}$$

where

$$F_{\alpha_i,\alpha_r} = \frac{\Lambda}{2^{\alpha_r}} \cdot \left[\sum_{j}^{\alpha_r} \begin{pmatrix} \alpha_r \\ j \end{pmatrix} \cdot I_j \right] + \frac{(1-\Lambda)}{2^{\alpha_i}} \cdot \left[\sum_{j}^{\alpha_i} \begin{pmatrix} \alpha_i \\ j \end{pmatrix} \cdot I_j \right] \quad (2.50)$$

and I_j as in Eq. 2.46.

Polarization of a diffuse scattering ray

Even if diffuse scattering plays an important role in the prediction of the polarization behavior of the channel, no specific model was available for the polarization behavior of the diffuse scattering interaction itself, at the time of its first implementation in UCL tool. As a first attempt, the scattered power is equally divided between the perpendicular and the parallel component in the following way:

$$\mathbf{E}_s = \frac{1}{\sqrt{2}} E_s \hat{e}_{s\parallel} e^{j\psi_\parallel} + \frac{1}{\sqrt{2}} E_s \hat{e}_{s\perp} e^{j\psi_\perp} \quad (2.51)$$

where $\psi_\parallel$ and $\psi_\perp$ are the random phases, generated with a uniform distribution.

The model, as presented in Eq. 2.51, has been used in all results with the exception of the ones presented in Chapter 6, where the polarization model is re-defined (see Section 6.1.4) exploiting specific measurements carried out to investigate the polarization behavior of diffuse scattering.

2.5 Penetration

In outdoor scenarios, penetration through buildings is normally neglected in RT for two main reasons: the significant attenuation due to this interaction and the difficulty to model the interior of buildings, i.e. the difficulty to predict the field associated to a ray that emerges from a building after penetration. On the other hand, when we are dealing with indoor scenarios, the implementation of penetration becomes essential. In many simulation environments the two terminals can be in different rooms, thus completely separated by internal walls and doors. If penetration is not implemented, situations where no ray is predicted arriving at the receiver may occur frequently.

For this reason, in this section, a penetration model that uses the well-known oblique incidence transmission coefficients, both at the incoming and outgoing boundaries is used to evaluate the transmitted component of the field. For simplicity, only the direct transmitted field is considered, while the multiple reflections inside the dielectric medium

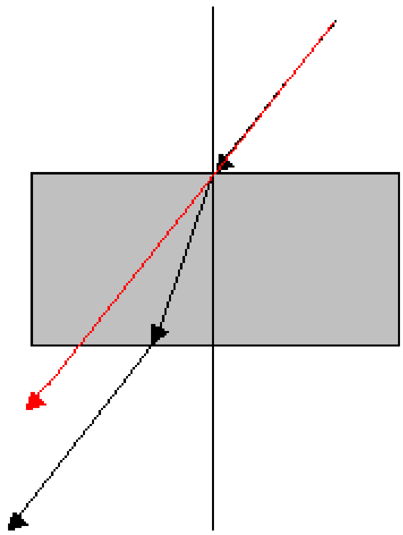

Figure 2.7: Penetration scheme: the path of a ray is not modified by the interaction

are discarded. In addition to this, a simple approximation, not to affect the image database construction on which the ray tracing tool is based, is made: the path of a ray that undergoes penetration is not modified by this interaction. This means that the output point and the length of the path are evaluated as if they formed a straight line as depicted in Fig. 2.7. However, the correct values of the angles are computed to evaluate the transmission coefficients. The possibility of total internal reflection is also considered (see Eq. 1.16).

A penetration loss is evaluated for the propagation into the block, depending on the electric properties of the medium crossed. Accordingly, the field at the observation point P can be evaluated in the following way:

$$\mathbf{E}(P) = \overline{\mathbf{T}}_{in} \cdot \overline{\mathbf{T}}_{out} \cdot \mathbf{E}(O) \frac{e^{-jk(s_1+s_2)} e^{-jk_p s_p}}{s} \tag{2.52}$$

where $\overline{\mathbf{T}}_{in}$ and $\overline{\mathbf{T}}_{out}$ are the dyadic transmission coefficients, s is the total length of the path, s_p is the length of the section of path undergoing penetration, s_1 is the distance between the transmitting point and the incoming penetration point, s_2 is the distance between the outgoing penetration point and the observation point and k_p is the propagation constant in the lossy medium, where the penetration occurs. At each interface the dyadics are formed by the perpendicular polarization Fresnel transmission coefficient by [57]:

$$T_{\perp} = \frac{2\cos\theta_i}{\cos\theta_i + \sqrt{\epsilon_{e2}/\epsilon_{e1} - \sin^2\theta_i}} \tag{2.53}$$

and by the parallel polarization Fresnel transmission coefficient by [57]:

$$T_{\parallel} = \frac{2\sqrt{\epsilon_{e1}/\epsilon_{e2}}\cos\theta_i}{\cos\theta_i + \sqrt{\epsilon_{e1}/\epsilon_{e2}}\sqrt{1-(\epsilon_{e1}/\epsilon_{e2})\sin^2\theta_i}} \tag{2.54}$$

where ϵ_{e1} is the effective permittivity of the medium before the interface and ϵ_{e2} is the effective permittivity of the medium after the interface.

Also in this case, it is possible to express, according to Eq. 1.39, the depolarization matrix that can be written as:

$$[T] = \begin{bmatrix} T_{\perp} & 0 \\ 0 & T_{\parallel} \end{bmatrix} \tag{2.55}$$

2.5.1 Attenuation by vegetation

A different approach has been chosen to model penetration through vegetation. Trees are highly inhomogeneous and cannot be modeled as blocks where propagation is studied with oblique incidence transmission coefficients and dielectric permittivity and conductivity. Although in some studies [58] a theoretical approach has been carried out to analyze penetration loss due to trees, the forward transmission through vegetation is generally dealt with empirical methods, whose parameters are derived from measurements. This section provides a review of the most useful models and describes the implementation of trees in RT.

The Weissberger modified exponential decay model [59] estimates the excess attenuation due to the presence of trees with full foliage as a function of frequency and penetration distance. The model covers a frequency range between 230MHz and 95GHz and a penetration depth up to $400m$. Its formulation is the following:

$$L = \begin{cases} 1.33 f^{0.284} d^{0.588} & 14 < d \leq 400 \\ 0.45 f^{0.284} d & 0 < d \leq 14 \end{cases} \tag{2.56}$$

where f is the frequency in GHz, d is the length of the portion of path undergoing penetration in meters and L is the excess loss in dB.

A similar model is the Fitted ITU-R model [60]. It is valid in the frequency range between 11GHz and 20GHz and it expresses the excess

Table 2.1: Summary of specific attenuation coefficients by single tree

Reference	Atten. [dB/m]	In Leaf	Freq. [GHz]
Cavdar et al. [63]	1.3	yes	1.6
de Jong and Herben [45]	1.1	yes	1.9
	0.8	no	
Horak and Pechac [64]	1	yes	2
	0.6	no	
ITU-R [65]	[1 . . . 2]	yes	[1 . . . 4]

attenuation as:

$$L = \begin{cases} 0.37 f^{0.18} d^{0.59} & \text{out of leaf} \\ 0.39 f^{0.39} d^{0.25} & \text{in leaf} \end{cases} \tag{2.57}$$

where f is the frequency in MHz, d is the length of the portion of path undergoing penetration in meters and L is the excess loss in dB. The main difference with respect to the Weissberger model is the capability to distinguish between in leaf and out of leaf conditions. An alternative solution to take into account the absence of leaves is given in [61], where the specific attenuation coefficient for leafless trees is found to be 20% smaller than the one for trees with full foliage.

While these models are generally used for long penetration distances, i.e. forests or highly vegetated areas, it has been shown that the attenuation coefficient in dB/m might be higher for single tree scenarios or short penetration distances [62]. Table 2.1 shows a summary of the specific attenuation by single tree retrieved from literature.

As these results are valid at a single frequency, it is important to include some additional frequency scaling consideration. In [62] the following formula has been introduced:

$$L\left(f_2\right) = L\left(f_1\right)\sqrt{\frac{f_2}{f_1}} \tag{2.58}$$

where L is the attenuation coefficient expressed in dB. This equation is obtained for UHF and L-Band frequencies, but validated also for S-Band. Instead, in [66] the following scaling equation has been found valid between L-Band and K-Band:

$$L\left(f_2\right) = L\left(f_1\right) e^{1.5\left[\left(\frac{1}{f_1}\right)^{0.5} - \left(\frac{1}{f_2}\right)^{0.5}\right]} \tag{2.59}$$

In [58], an analytical polarization dependent model for attenuation by the canopy of a tree has been derived. The specific attenuation coefficient for the θ component it is:

$$L_{\theta\theta} = 91 f \chi_i \rho_c \frac{\pi h r_c}{\sin\theta_i}\left(\frac{1}{2}\cos^2\theta_i I_1 + \sin^2\theta_i I_2\right) \tag{2.60}$$

while for the ϕ component is:

$$L_{\phi\phi} = 45.5 f \chi_i \rho_c \frac{\pi h r_c}{\sin\theta_i} I_1 \tag{2.61}$$

where f is the frequency in GHz, χ_i is the imaginary part of $\chi = \epsilon_e - 1$, ρ_c is the density of branches in the canopy, h is the length of the branch, r_c is the radius of the branch and θ_i is the angle of incidence. The coefficient I_1, that depends on the inclination angles of the branches, is defined as:

$$I_1 = \frac{1}{2}\left[1 - \frac{1}{\psi_{max} - \psi_{min}}\cos\left(\psi_{max} + \psi_{min}\right)\sin\left(\psi_{max} - \psi_{min}\right)\right] \tag{2.62}$$

where ψ_{min} and ψ_{max} are, repsectively, the minimum and maximum inclination angle of the branches in the canopy. The coefficient I_2 is defined as:

$$I_2 = 1 - I_1 \tag{2.63}$$

2.5.2 Building penetration

At the beginning of this section, it was said that building penetration is usually neglected in RT outdoor scenarios. There are some special cases when it might be necessary to take into account this mechanism, e.g. for low frequencies, compatibly with the validity of GO approximation, i.e. when the wall attenuations are less penalizing.

In this section, a simple and intuitive building penetration model is presented. The goal of this model is to evaluate the excess attenuation of a path undergoing building penetration, neglecting the multipath effects generated by the multiple interactions with the elements forming the building. The model is divided in three parts:

- attenuation due to external walls,
- attenuation due to floor crossings,
- additional specific attenuation for indoor environment.

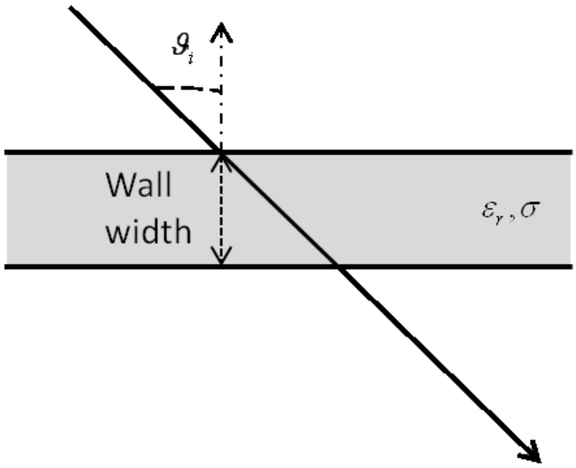

Figure 2.8: Scheme of the wall penetration geometry

Wall penetration

The idea behind the wall penetration model is very simple. Given the dielectric properties and the width of the wall as input parameters (see Fig. 2.8) and calculating the length of the path across the wall as

$$d_w = w_w / \cos\theta_i \tag{2.64}$$

the attenuation is evaluated as $e^{-\alpha d_w}$, according to the propagation in lossy medium. While crossing a building a ray encounters two exterior walls, so the same procedure is applied twice, considering that the normal unit vector is known within the RT for each block surface.

Floor penetration

The number of floor separations crossed by a ray is determined by evaluating the number of floors in the building, the height of the building, both given as input parameter, and the z-coordinate of the two points where the ray intercepts the building. Once this number is known, the attenuation coefficient for each separation can be evaluated in the same way as the one for the wall, if it is considered that the unit vector normal to the surface is oriented as $\pm\hat{z}$ depending on the orientation of the ray.

Indoor specific attenuation

An additional attenuation factor has to be taken into account to consider the loss due to propagation inside a building. In this model a log-distance

Table 2.2: Summary of weaknesses of pre-existent models for scattering by trees

Reference	Weakness
de Jong [45]	Not fully 3-D and not fully polarized
Lin [68]	Semi-exact solution for a trunk above a ground plane, with plane wave hypothesis and complex formulation of the scattered field
Karam [69]	Scattering by cylinder small compared to wavelength → not suitable for GO based RT
Torrico [58]	Forward scattering is used to evaluate specific attenuation by trees

path loss has been considered. Its formulation is the following:

$$L_i\,[\mathrm{dB}] = 10\gamma \log_{10}(d_i) \tag{2.65}$$

where γ is the path loss exponent. If the excess attenuation has to be considered the path loss exponent has to be modified as $\gamma_e = \gamma - 2$. Path loss exponent are extracted from measurements and there is a wide selection of literature that propose different values of γ depending on the environment and frequency. As an example, in [67] a path loss exponent of $\gamma = 3.2$ is found for office buildings at 914MHz.

2.6 Scattering by vegetation elements

In this section, a model to evaluate scattering by tree branches is presented. While several contributions can be found in literature on scattering by vegetation [45, 58, 68, 69], this model aims to be simple and easily implementable in a RT tool. Table 2.2 presents a summary of the main reasons why a newly developed model was preferred over pre-existent ones for implementation in RT.

2.6.1 Cylinder geometry

Tree branches are modeled as cylinders with a circular base. Their geometry can be defined by the following parameters:

- the center of the cylinder of coordinates (x_c, y_c, z_c),
- the length of the cylinder h,
- the radius of the cylinder r,

- the orientation of the cylinder in space, given by the unit vector $\hat{a}$.

To simplify the model, a local coordinate system is associated with each branch. Let $\hat{u}$, $\hat{v}$ and $\hat{w}$ be the new set of coordinates having the center of the cylinder as origin. The axes are chosen in the following way:

$$\begin{cases} \hat{w} = \hat{a} \\ \hat{u} : \ \hat{w} \cdot \hat{u} = 0 \\ \hat{v} = \hat{w} \times \hat{u} \end{cases} \tag{2.66}$$

The first equation lets the axis of the cylinder have a vertical orientation. Given the geometry of the circular cylinder, any couple of unit vectors that forms a coordinate system with the first one are a valid choice, so they are chosen accordingly. At this point, the parametric equation of the cylinder can be written as:

$$\begin{cases} u = r\cos\theta \\ v = r\sin\theta \\ w = h \end{cases} \tag{2.67}$$

2.6.2 Determination of the scattering point

Before evaluating the scattering contribution, it is necessary to determine the scattering point. The first step is to verify if scattering is possible, that is when the source and receiving points are not on the opposite side of the cylinder.

In literature it is found that the center of the cylinder can be considered as the origin of the scattering interaction [70]. This is in accordance with the theory of diffuse scattering, where the center of a surface element is the origin of the interaction. As the center of the cylinder is not on its surface, the scattering point is found by projecting on the surface of the cylinder the path connecting the receiver to the transmitter through the center of the cylinder. This is done by intersecting the line perpendicular to the Tx-Rx direction and passing from the center with the surface of the cylinder. Clearly this generates two intersection points. The closer one to the Tx-Rx path becomes the scattering point (u_s, v_s, w_s). A scheme of this operation is depicted in Fig. 2.9.

In addition to this, it is necessary to verify that that w_s is comprised between the height limits of the cylinder. If it falls outside those limits, no scattering contribution is given by the cylinder under examination.

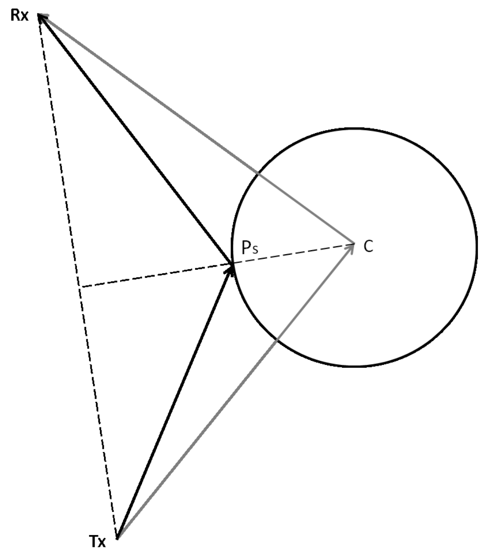

Figure 2.9: Individuation of the scattering point on the cylinder

Finally, the parameter θ of the scattering point on the cylinder can be evaluated as follows

$$\theta = \arctan\left(v_s/u_s\right) \tag{2.68}$$

2.6.3 Evaluation of the scattered field

As the attempt is to evaluate the scattered field by tree branches starting from the GO reflected field, the scattering interaction has to be compatible with the rules of GO. For this reason the branches with radius smaller than the wavelength are discarded.

In the first instance, let us consider the possibility that the receiver and the transmitter are specular with respect to the scattering point. In that case, specular reflection on a curved surface is taking place and the point on the cylinder is a reflection point. The spreading factor for a wave reflected on a cylinder is given by:

$$A\left(s_r\right) = \sqrt{\frac{\rho}{\rho + s_r}} \tag{2.69}$$

where s_r is the distance between the reflection point and the receiver and ρ is the principal radius of curvature of the reflected wavefront ($\rho_{r2} \rightarrow \infty$). The radius of curvature can be evaluated as:

$$\frac{1}{\rho} = \frac{1}{s_i} + \frac{1}{f_1} \tag{2.70}$$

where s_i is the distance between the reflection point and the source and

$$f_1 = \frac{a_1 \cos\theta_i}{\sin^2_{\theta_2}} \tag{2.71}$$

where θ_i is the angle of incidence and a_1 and θ_2 are computable given the geometry of the problem [18]. Accordingly, the reflected field at the observation point is

$$\mathbf{E}_r\left(P_{Rx}\right) = \overline{\mathbf{R}} \cdot \mathbf{E}_i\left(P_s\right) A\left(s_r\right) e^{-jks_r} \tag{2.72}$$

where P_{Rx} and P_s are the observation and the reflection point respectively and $\overline{\mathbf{R}}$ is the classical dyadic reflection coefficient.

In general, the scattering direction is not going to coincide with the specular direction. For this reason the scattered field in a generic direction is obtained multiplying the reflected field by a reduction coefficient dependent on the angle between the scattering direction and the specular direction. Three different laws are implemented to evaluate the coefficient S_r.

- a cosine law: $S_r = \frac{1+\cos\psi_r}{2}$,
- an exponential law: $S_r = e^{-\psi_r}$,
- a linear law: $S_r = 1 - \psi_r/\pi$

where ψ_r is the angle between the specular and scattering direction. Fig. 2.10 presents the plot of the different laws.

Concerning the polarization behavior of the scattering from vegetation, as no information is available, it is assumed that the scattered field is totally depolarized. Then:

$$\mathbf{E}_s = \frac{1}{\sqrt{2}} E_r C_r \hat{e}_r + \frac{1}{\sqrt{2}} E_r C_r \hat{e}_{xp} \tag{2.73}$$

where $\hat{e}_r$ is the polarization that the reflected field would have and $\hat{e}_{xp}$ is the polarization orthogonal to $\hat{e}_r$.

2.7 Antenna implementation in Ray-Tracing

Depending on the context, transmitting and receiving antennas may or may not be considered part of the wireless communication channel. Channel measurements clearly have to be done with specific antennas. Removing their contribution is possible and it can be done using high resolution algorithms (see Section 3.3), but it is a complex and time-consuming operation. One of the great advantages of a full 3-D RT tool

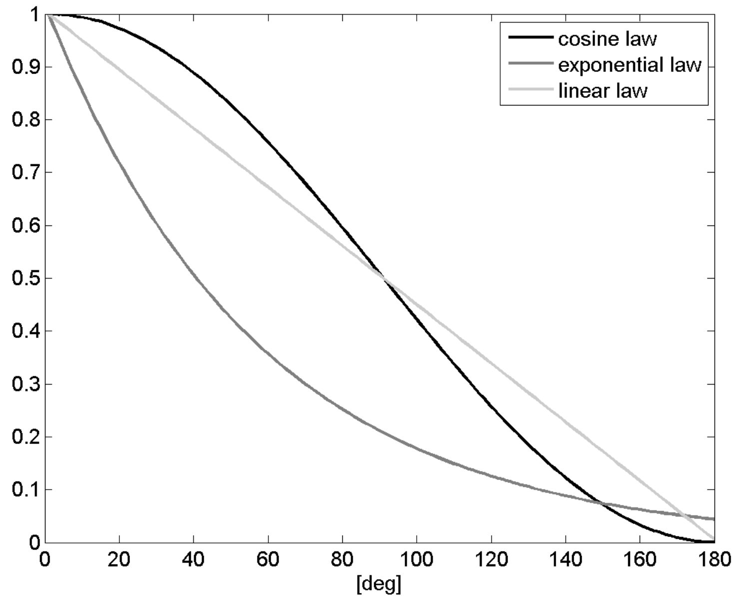

Figure 2.10: Individuation of the scattering point on the cylinder

is its extreme flexibility towards antenna implementation. Considering that for each ray the direction of departure and the one of arrival are intrinsically known by the RT, any antenna with known radiation properties can be implemented. Antenna contribution can be also removed or not considered, in a straightforward way.

At transmit side, a complex 3-D vector is generated knowing the radiation and polarization properties of the antenna in the direction of propagation of the ray. At receive side, the complex 3-D vector representing the impinging wave is projected on the vector representing the fully polarized radiation properties of the receiving antenna in the direction of arrival of the ray.

A specific type of antenna implemented in the RT tool is a generic dipole of length L which normalized radiation pattern is:

$$\mathbf{f}(\theta) = j \frac{cos\left(\frac{kL}{2}\cos\theta\right) - \cos\frac{kL}{2}}{\sin\theta}\hat{\theta} \tag{2.74}$$

More generally, any antenna which radiation pattern is available can be implemented. For example, assuming tabulated f_θ and f_ϕ components, the pattern in the ray direction (θ_r, ϕ_r) is:

$$\mathbf{f}(\theta_r, \phi_r) = f_\theta(\theta_r, \phi_r)\hat{\theta} + f_\phi(\theta_r, \phi_r)\hat{\phi} \tag{2.75}$$

3

Measurements and simulations: practicalities

3.1 Channel sounding

Channel measurements are a very important part of the study of wireless communications. In particular for RT, they are used to validate the tool altogether or specific models implemented in it. The set of measurement techniques used to evaluate channel characteristics is called channel sounding.

The principle of channel sounding is straightforward. A known signal is transmitted and the properties of the wireless channel are estimated from the received signal. The transmitted signal should have the following properties [8]:

- large bandwidth: to achieve good delay resolution,
- uniform spectral density: to achieve uniform performances at all frequencies under test,
- low peak-to-average ratio: to have an optimal usage of the power amplifier,
- large time-bandwidth product: to improve the SNR,
- an adequate duration: i.e. long to improve the time-bandwidth product, but not longer than the coherence time of the channel.

Consequently, the most common waveforms used for channel sounding are the following [71]:

- a chirp signal: a signal in which the frequency increases (or decreases) with time,

- a multi-tone signal: it has flat spectrum and low peak-to-average ratios can be obtained,
- a pseudo-noise sequence: deterministically generated, but with characteristics similar to a random sequence; it has good time-bandwidth product and each of its elements is called chip.

A crucial issue for sounding techniques is synchronization between transmitter and receiver units. Frequency offsets between the local oscillators at the two terminals can create phase rotations and a consequent slide of the impulse response delay. When possible, i.e. short range indoor measurements, the two units can be connected through a coaxial cable or fiber-optic cables where a synchronization signal is sent. In most of the measurement scenarios this is not possible. Sounding equipments are often employed with atomic clocks that provide stable frequencies and that can be synchronized at the beginning of the campaign.

In a channel sounder, the transmitter normally sends pulses periodically repeated with a period T. When a time variant channel has to be measured the choice of this parameter is of great importance. On one side it has to be smaller than the coherence time of the channel, set by the Doppler frequency related to the maximum mobile speed v_{max}, i.e. $T \leq c/(2f_c v_{max})$. On the other side, the period has to be longer than the maximum excess delay expected from the channel, $T \geq \tau_{max}$, to avoid overlapping from contiguous pulses.

Channel measurements can be carried out also using a Vector Network Analyzer (VNA), that is able to evaluate the matrix S composed by scattering parameters of a device under test. If transmitting and receiving antennas are connected to it, the wireless channel can be the actual device and S_{21} represents its transfer function. The transmitted signal is a step frequency continuous wave. While channel sounders work at a fixed predetermined frequency, the great advantage of a VNA is the flexibility of the center frequency f_c and also of the bandwidth. On the other hand the two main disadvantages are a slow acquisition rate (only static measurements are possible) and the inevitable co-location of the transmitter and receiver, that limits its usage for short-range indoor measurements.

3.2 The ElektroBit channel sounder

The ElektroBit channel sounder is composed by two units, as shown in Figs. 3.1 and 3.2: a transmitter unit and a receiver unit, which is composed by two modules, one of which is the data acquisition module.

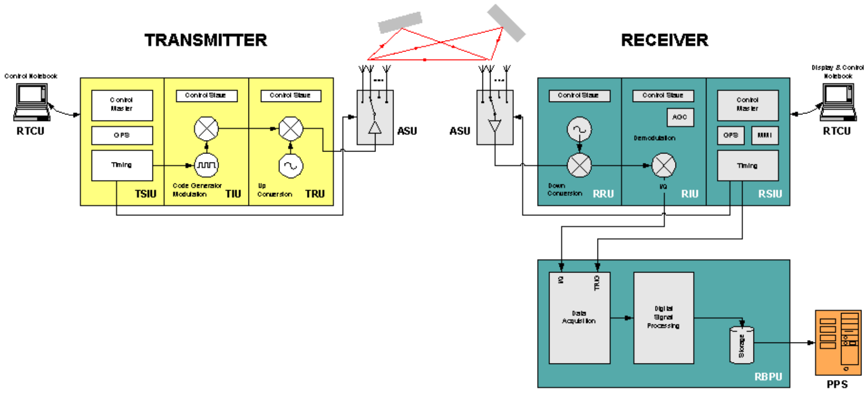

Figure 3.1: ElektroBit channel sounder architecture [72]

Each unit is controlled by the user with a laptop computer through a LAN connection. At transmit side, a pseudo-noise sequence is generated and used to modulate the transmitted signal that is up-converted to radio frequency from an intermediate frequency. Specularly, at receive side, the received signal is down-converted and demodulated into I/Q format. This channel sounder can be used for MIMO measurements as it includes fast switches that can connect multiple antennas to each unit.

A crucial step in all measurement campaigns where the two units, Tx and Rx, are separated is the synchronization of the local oscillators, which employ Rubidium clocks. In the ElektroBit channel sounder, it takes place in two steps: the synchronization in a strict sense, where the relative phase rotation is minimized by tuning the atomic clocks, and the time-tag synchronization, where a common absolute time reference is given to the two units. The synchronization is kept for long time, but phase drifts can be present also after synchronization. These may generate linear phase variations in a static environment, e.g. the one presented in Fig. 3.3, that have to be corrected in post-processing. In Clock-Keep Alive (CKA) mode, it is possible to move the sounder without external power supply and without losing synchronization.

Another important concept is the one of timing, shown in Fig. 3.4. The basic unit is the chip, which represent one symbol of a code. The chip rate is the metric that controls the timing. The higher the chip rate the better the delay resolution of the measured impulse response. The delay sampling resolution can be evaluated as:

$$\tau_{resolution} = \frac{1}{f_{chip} \times N_{sc}} \tag{3.1}$$

where N_{sc} is the number of samples per chip. The chip rate is limited

Figure 3.2: ElektroBit channel sounder picture

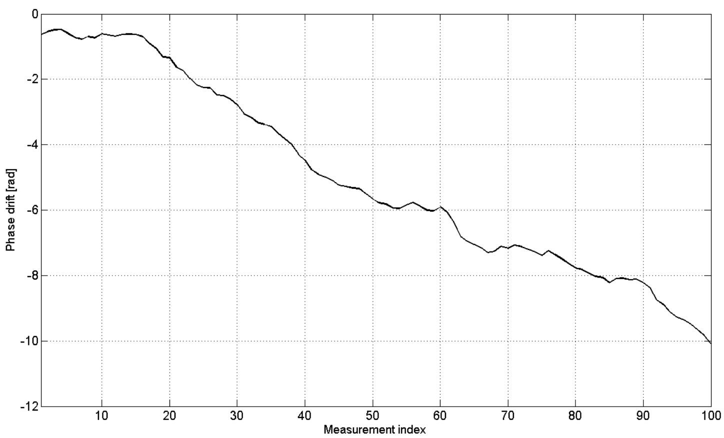

Figure 3.3: Linear phase drift of LOS component in static environment

by the bandwidth, as $f_{chip} = BW/2$. Each transmitted code is formed by several chips. The length of a code has to be longer than the maximum measurable delay in the propagation scenario but shorter than the Doppler period, i.e. the time for which the channel can be considered constant. Longer codes also produce higher processing gain, thus improving the dynamic range. The measurable excess delay is:

$$\tau_{excess} = \frac{N_{chips}}{f_{chip}} \tag{3.2}$$

where N_{chips} is the code length in chips. For each transmitting antenna, a number of codes equal to the receiving antenna plus one is transmitted. The supernumerary code serves as guard, needed to let the transmitter switch to the next antenna in the sequence. When all the receive and transmit antennas are scanned, the acquisition cycle, which represents the measured channel at a certain time, is concluded. For each acquisition cycle, the number of codes is:

$$N_{codes} = N_{Tx}\left(N_{Rx} + 1\right) \tag{3.3}$$

The Doppler frequency of the time-varying channel has to be sampled according to the Nyquist criterion, where a sample is represented by a full cycle. The minimum channel sampling rate is evaluated as:

$$f_{cs} = \frac{v_m + 2v_s}{\lambda} N_\lambda \tag{3.4}$$

where v_m is the maximum speed of the mobile terminal, v_s is the maximum speed of the scatterers and N_λ is the number of wished channels per wavelength. In case of measurements in a scenario with a very high Doppler frequency, the cycles can be measured in bursts, i.e. during part of the time cycles are measured and during the rest data are stored on the disk, without taking measurements.

Input parameters can be introduced in the channel sounder via the laptop connection with the help of an easy-to-use set-up wizard. Fig. 3.5 shows an illustrative screenshot of the wizard. Table 3.1 presents all the input parameters to be defined before the measurements and their acceptable values.

Before starting the data acquisition, a calibration measurement is required. This consists in measuring a well-known channel that normally is an attenuator of given attenuation back-to-back connected to the units via the measurement cables. This produces the system response that can be used in post-processing to compensate for system and cable losses. The calibration impulse response, an example in Fig.

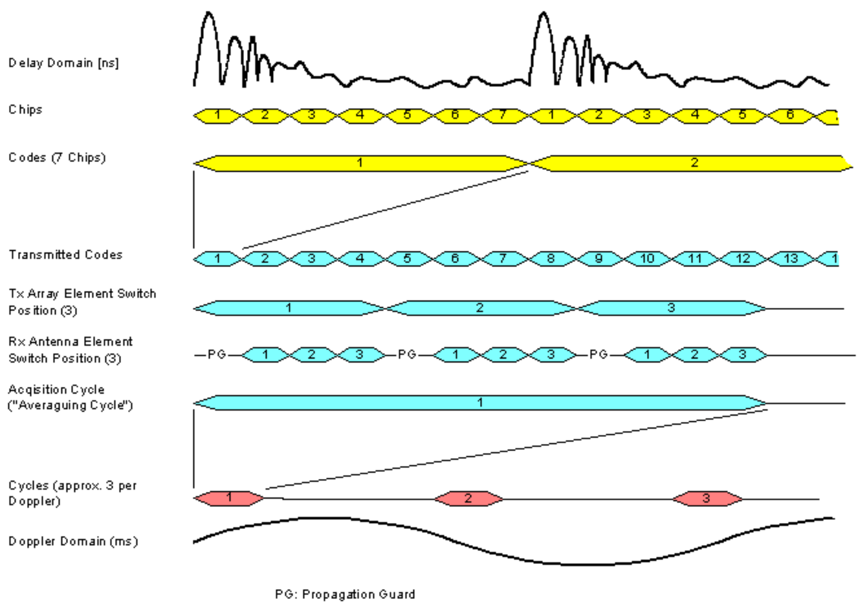

Figure 3.4: ElektroBit channel sounder timing concepts [72]

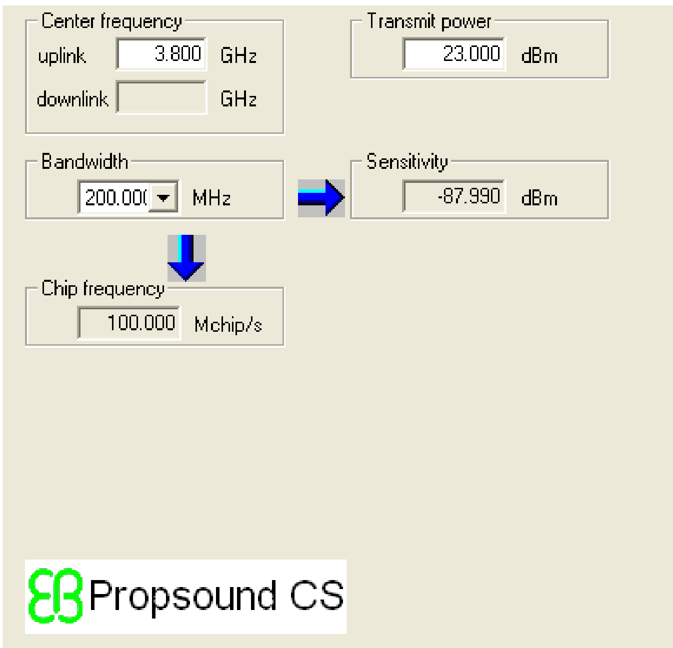

Figure 3.5: Channel sounder set-up wizard screenshot

Table 3.1: Input parameters for the ElektroBit channel sounder

Carrier frequency	from 3.5 to 4.2GHz
Bandwidth	from 1.5 to 200MHz
Transmit power	default value 23dBm
Number of samples per chip	from 1 to 10
Max. path length	Sets the min. code length in chips
Number of Tx antennas	from 1 to 8
Number of Rx antennas	from 1 to 8
Max. mobile/scatterer speed	Sets the min. channel sample rate

3.6, after normalization, can also be chosen to represent the filter of the system and then used to do the convolution with the discrete response of the RT tool.

3.3 Parameter estimation with high resolution algorithms

The development of MIMO systems that employ diversity multiplexing techniques requested a detailed knowledge of channel characteristics in terms of delay, polarization, angles and Doppler parameters. For this reason, signal processing techniques have been developed or adapted to estimate those propagation parameters from measurement campaigns.

The first thing to be noted is that channel measurements need to yield enough resolution in the specific parameters of interest. The most interesting case concerns directional and polarization information, i.e. the employment of arrays of antennas. The following three array techniques can be used [8]:

- real arrays, where each antenna is connected to a dedicated modulation or demodulation chain,
- multiplexed arrays, where multiple antennas are connected to a unique chain through a fast switch,
- virtual arrays, where a single antenna is mechanically moved in diffrent positions.

If a system with N receiving antennas is considered, it is necessary that during the acquisition of N measurements the propagation environment has to be considered static. In real arrays, measurements are done simultaneously, at the cost of a complex architecture. With virtual arrays

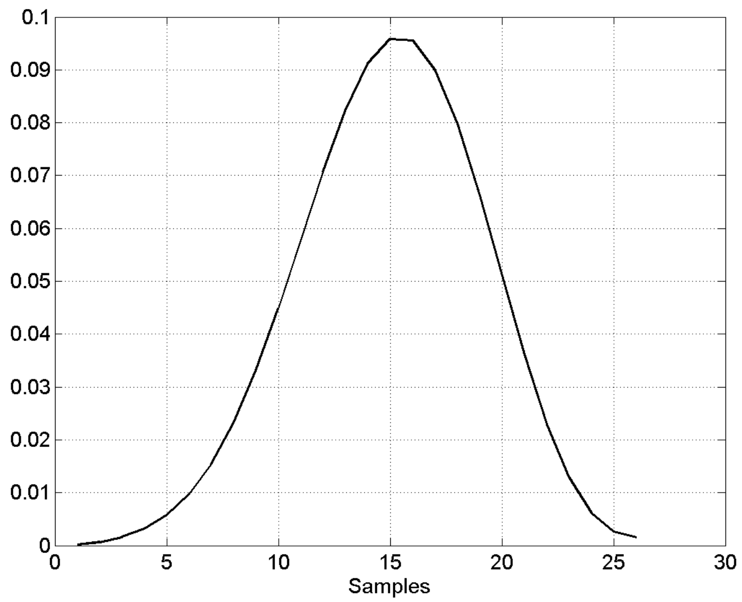

Figure 3.6: Calibration impulse response

only measurements in static environments are possible as the time employed to mechanically scan all the array positions is much larger than the coherence time of any time-variant channel. Multiplexing arrays are a trade-off between complexity and velocity of acquisition.

A first class of parameter estimators is the one based on beamforming [73], a technique to spatially filter the received signal. Its capability to discriminate propagation directions depends on the effective aperture of the array, thus on the number of elements. On the other hand, high resolution algorithms in the strict sense overcome this limitation at the cost of a higher computational complexity.

Among the most common, there is MUSIC algorithm [74] that estimates the number of propagation paths, their strength and their directions of arrival exploiting the eigenstructure of the covariance matrix. ESPRIT [75] is a subspace-based estimator with reduced complexity with respect to MUSIC one. In its original form was employed for azimuth estimation, i.e. in case of linear arrays, but it has been extended also for delay and elevation estimation.

The most successful high resolution algorithm is probably SAGE [76], a maximum-likelihood based estimator which, in his improved version (called ISIS) [77], is able to extract from measurement the joint angular-delay-Doppler characteristics of propagation paths as well as their polarization matrix. Another advantage of this method is the capability to work also with contributions with small amplitude. The output information of SAGE high resolution algorithm for each ray are:

- delay of arrival τ
- azimuth of departure ϕ_d
- azimuth of arrival ϕ_a
- polarization matrix $\Gamma = \begin{bmatrix} \gamma_{\theta\theta} & \gamma_{\theta\phi} \\ \gamma_{\phi\theta} & \gamma_{\phi\phi} \end{bmatrix}$

where in matrix Γ, the directional properties of Tx and Rx antennas are de-embedded and the component $\gamma_{\psi\xi}$ represents the transfer function of the considered ray for ψ-polarization at the Rx side and ξ-polarization at the Tx side, where ψ and ξ identify the two orthogonal, linear polarization states.

Finally, RIMAX [71] is another maximum likelihood estimator with the advantage of jointly evaluating specular and diffuse component parameters and that is also able to inherently provide the variance of the parameters as measure of their reliability.

3.4 Evaluation of channel metrics in measurements and simulations

The most common channel metrics used in this thesis are recalled at the beginning of this section. The power delay profile is defined as:

$$P_h(\tau) = E\left\{|h(t,\tau)|^2\right\} \tag{3.5}$$

where the expectation is taken over time, by assuming ergodicity. The RMS delay spread is defined as:

$$\tau_{rms} = \sqrt{\frac{\int_0^{\tau_{max}} (\tau - \tau_m)^2 P_h(\tau)\, d\tau}{\int_0^{\tau_{max}} P_h(\tau)\, d\tau}} \tag{3.6}$$

where τ_m is the mean delay. The narrowband power is evaluated as:

$$P_r = E\left\{|h(t)|^2\right\} \tag{3.7}$$

where

$$h(t) = \int_0^{\tau_{max}} h(t,\tau)\, d\tau \tag{3.8}$$

Cross-polar discrimination, instead, is evaluated as:

$$XPD = \frac{P_{co}}{P_{xp}} = \frac{E\left\{\left|h_{co}\left(t\right)\right|^2\right\}}{E\left\{\left|h_{xp}\left(t\right)\right|^2\right\}} \tag{3.9}$$

where h_{co} and h_{xp} are the impulse responses of the co-polar and cross-polar channels respectively and the expectation is again taken over time.

All the measurement campaigns presented in this thesis have been carried out in static environments. Multiple realizations of the same channel (typically 100 with the ElektroBit channel sounder) are recorded and the expected value of the channel impulse response is evaluated over these realizations to reduce the noise level. To have a fair comparison, as RT does not model noise, this is removed from measurements applying a thresholding method. The threshold is set as the maximum value of the part of impulse response preceding the LOS, where it can be supposed there is only noise.

To mitigate fading effects, one of the following actions is taken:

- in SISO scenarios, measurements and simulations are taken in multiple positions in the vicinity of the nominal one,
- in MIMO scenarios, multiple antennas are used both in measurements and simulations in place of multiple positions,
- in specific scenarios, virtual arrays are used in measurements with the help of automatic positioners.

Then, channel metrics are evaluated taking the expectation over multiple spatial (or antenna) realizations.

3.5 On the evaluation of errors in Ray-Tracing predictions

The validation is a crucial part of the development of a RT tool. Validation means comparison with measurements in selected scenarios. The difference between measurements and their simulated predictions can be expressed in terms of errors. For this reason, it is important to define how these errors can be evaluated.

If N measurement values M_i are assumed, together with their relative prediction values P_i, one can define several types of error. In this thesis, even when not specified, the error is always evaluated taking into account the absolute value of the difference between the real value and its estimation. Thus, the mean absolute error is:

$$e_{ma} = \frac{\sum_{i=1}^{N} |M_i - P_i|}{N} \tag{3.10}$$

while the root mean squared error (RMSE) is:

$$e_{rmse} = \sqrt{\frac{\sum_{i=1}^{N} (M_i - P_i)^2}{N}} \tag{3.11}$$

On the other hand, it is common to find in RT literature the mean error evaluated with its sign as:

$$e_m = \frac{\sum_{i=1}^{N} (M_i - P_i)}{N} \tag{3.12}$$

While this definition contains inherently information whether the prediction underestimate or overestimate the measurement in its sign, it tends to even out errors of different orientation, which in some case it might lead to an incorrect representation of the quality of the prediction. Defining the standard deviation of an error e as:

$$\sigma = \frac{\sum_{i=1}^{N} (e_i - \overline{e})}{N} \tag{3.13}$$

where $\overline{e}$ is the mean error, the relation between a mean error and the RMSE is the following:

$$e_{rmse} = \sqrt{\sigma_m^2 + e_m^2} = \sqrt{\sigma_{ma}^2 + e_{ma}^2} \tag{3.14}$$

where σ_m and σ_{ma} are the standard deviations for the mean and mean absolute errors respectively.

As an example, let us consider the fictional values of delay spread presented in Fig. 3.7 together with their fictional RT predictions. Table 3.2 presents a summary of errors evaluated with different definitions. When considering Eq. 3.14, all the definitions are equivalent, but their relation has to be clear in mind when comparing errors evaluated in different ways as a low mean error, when it is not evaluated in terms of absolute values, may not mean good accuracy. For this reason it looks more appropriate to express the errors in term of either the mean absolute error or the RMSE to have a better understanding of the prediction quality.

It can be significant, but it is also not very common in RT literature, to evaluate a relative error, i.e. a percentage error with respect to the

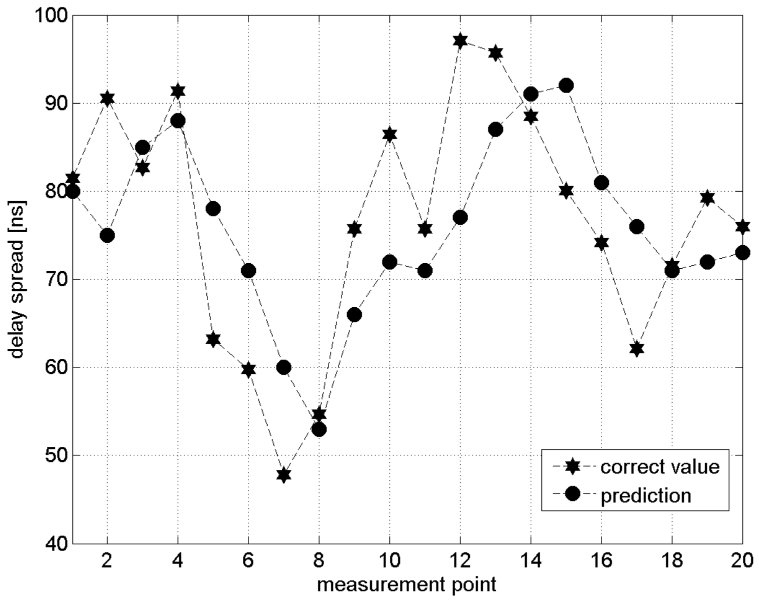

Figure 3.7: Fictional delay spread values for the comparison of error definitions

Table 3.2: Summary of errors from different definitions on fictinoal delay spread values

	Error [ns]	Standard Deviation [ns]
Simple Mean Error	0.8	10.3
Mean Absolute Error	8.3	5.8
RMSE	10	

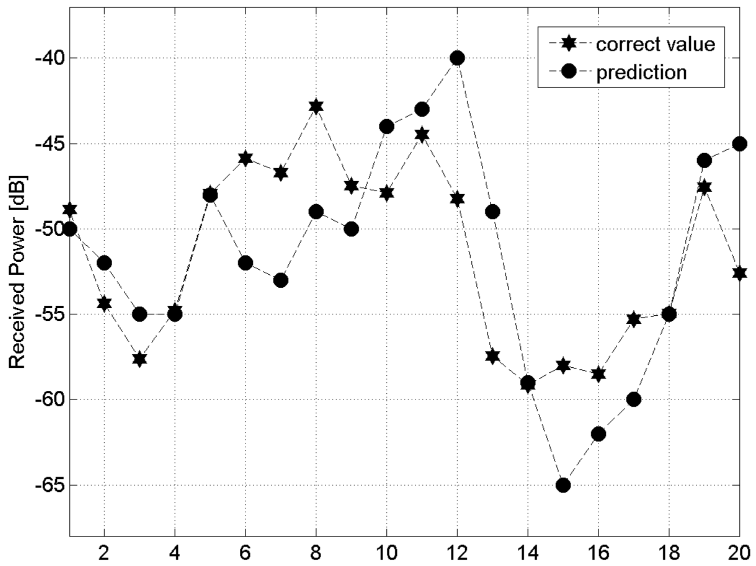

Figure 3.8: Fictional received power values, in dB, for the comparison of error definitions

measured value. The evaluation of the prediction quality may be significantly different if an error of 8ns is made on a delay spread of 80ns or on a delay spread of 10ns. Here the mean relative error (MRE) is defined as:

$$e_{mre} = \frac{1}{N}\sum_{i=1}^{N}\frac{|M_i - P_i|}{|M_i|} \tag{3.15}$$

For the example of Fig. 3.7, MRE is 11%.

A particular attention has to be given to the error evaluation of quantities normally expressed in dB, e.g. received power or XPD. As this scale is already a relative one, the errors can be directly evaluated on the curves in dB. Fig. 3.8 presents fictional values of received power and their prediction. Table 3.3 shows, in analogy with what it has been done before, the different error evaluations together with standard deviations. The conclusions are altogether similar with the ones drawn previously.

3.6 Ray-Tracing computation time

In this section, test RT simulations are run on a Sun Ultra 25 UNIX station with a processor frequency of 1.34GHz to evaluate the compu-

Table 3.3: Summary of errors from different definitions on fictional received power values

	Error [dB]	Standard Deviation [dB]
Simple Mean Error	0.1	4.8
Mean Absolute Error	3.7	2.9
RMSE	4.7	

tation time of UCL RT tool with different input parameters. Two test scenarios, an indoor and an outdoor one, are used for these simulations. Obviously, the computation time depends on the specific deployment of the scenario, so the aim of this section is only to give a general idea on how the different mechanisms and the complexity of the scenario impact on the simulation time.

Indoor scenario

The first scenario used for these tests is a typical office scenario, as depicted in Fig. 3.9. Twelve measurement positions are considered and the computation times are the result of an average of different values related to those positions. Half-wavelength dipoles at a frequency of 3.8GHz are used to model the antennas both at transmit and receive side. Fig. 3.10 shows the computation times in a logarithmic scale for maximum reflection order from 1 to 5. Simulations consider also LOS and single diffraction in addition to reflection. When the maximum reflection order is equal to n, reflections with orders $1, 2, \ldots, n-1, n$ are simulated. Various level of complexity of the scenario are also tested:

- 17 blocks, that correspond to an empty office, i.e. only walls, floor and ceiling are considered,
- 25 blocks, where all the major furniture, i.e. cupboards and table, is included in the database,
- 20 blocks, in case when only the furniture that is in the same room as the mobile terminal is considered.

When a maximum order of reflection equal to 5 is chosen, only simulations in a scenario with 17 blocks can be run, resulting in an impractical computation time of approximately 15 minutes. In the more complex cases the program exceeds the usable memory. A maximum of three reflections is normally a good trade-off between prediction accuracy and computation time, that can be limited in the order of few seconds.

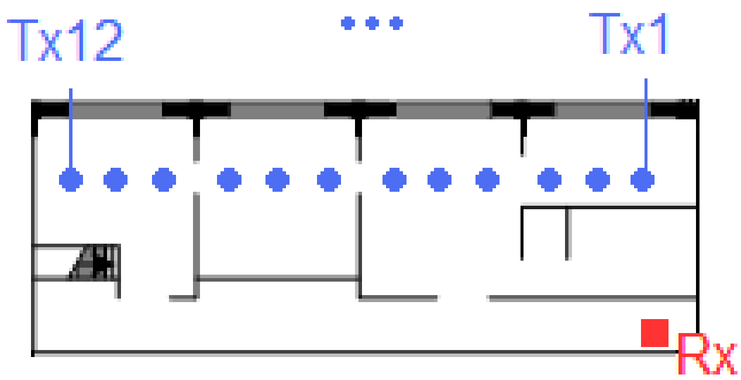

Figure 3.9: Indoor scenario for RT speed test simulations

Fig. 3.11 shows the computation time when diffuse scattering is introduced in the simulations. The maximum order of reflection is fixed to 3. The comparison is between simulations with no scattering, with single bounce scattering and scattering preceded or succeeded by a reflection. Also in this case, the three different levels of accuracy in the database description in terms of number of blocks are considered. Results show that single bounce scattering does not compromise the computation time, that is approximately doubled. A significant increase in computation time has to be taken into account if a reflection is included before or after the scattering interaction. If a maximum order of reflection equal to 4 is considered, adding single bounce scattering increases the computation time from 87s to 102s, in the 20 blocks scenario.

Outdoor scenario

Speed tests for the RT algorithm are run also in a typical urban outdoor scenario. Fig. 3.12 shows a 2-D map of the environment. Buildings are supposed to have a height between 5m and 15m, the base station is placed at a height of 20m and the mobile terminal is moving in twelve different positions at a height of 1.7m. Two levels of scenario complexity are tested:

- a simplified map with 16 blocks surrounding the terminal positions, in black in the map,
- a full map with all the 30 blocks in the environment.

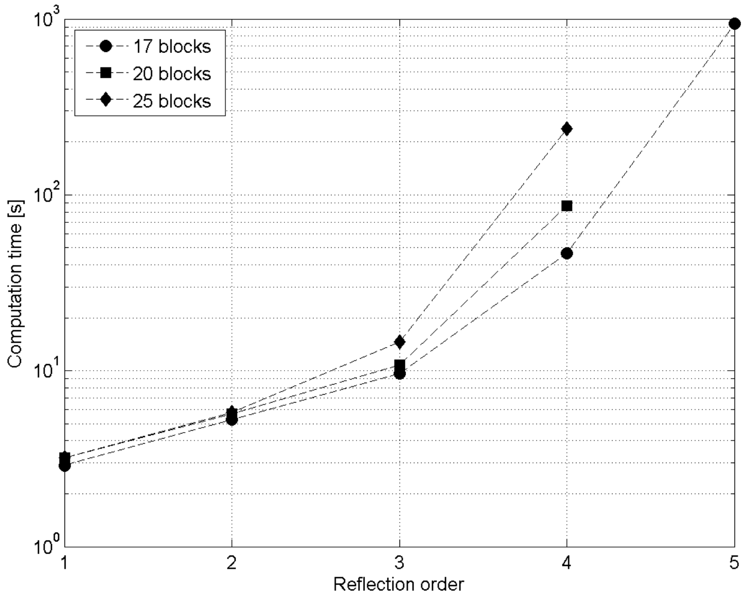

Figure 3.10: Computation time vs. reflection order and number of blocks in indoor scenario

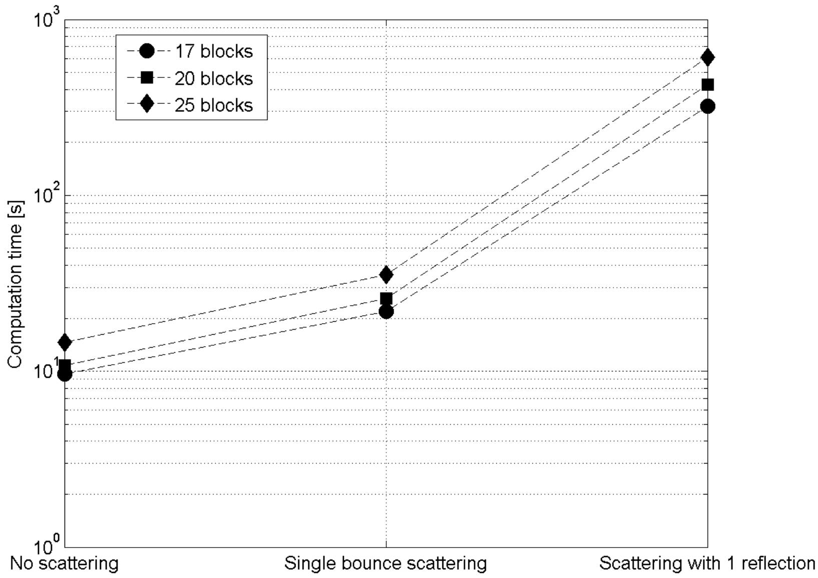

Figure 3.11: Computation time vs. diffuse scattering order and number of blocks in indoor scenario

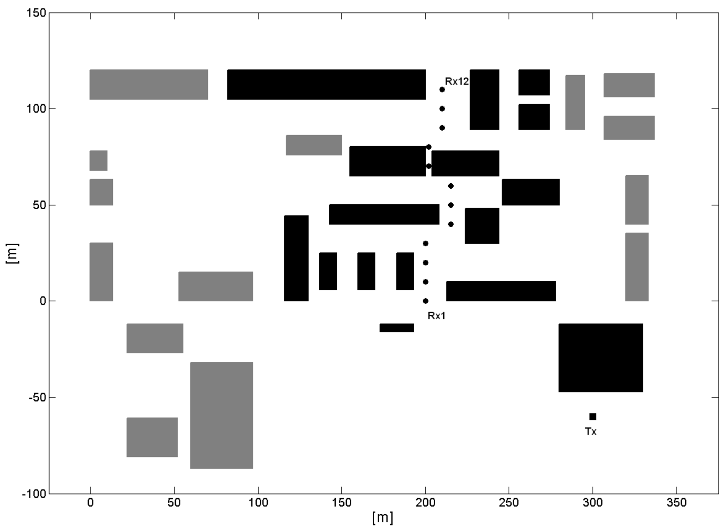

Figure 3.12: Outdoor scenario for RT speed test simulations

In a similar way with what it was presented in the indoor scenario, Fig. 3.13 shows the computation times in log-scale for maximum reflection order from 1 to 4. The conclusions are in all similar, but in this case the divergence between the curves representing the full and simplified scenarios for higher orders is even more evident, making feasible the use of fourth order reflections only when a simplified map is considered.

Fig. 3.14 shows the computation times when scattering is included in addition to a maximum order of reflection equal to 3. Also in the outdoor case, the introduction of single bounce scattering increases the computation time only by few seconds, while introducing another interaction before or after scattering affects it in a significant way.

3.6.1 Relevance of simplified maps and propagation mechanisms

It is not easy to say by looking at the computation time alone if it is relevant to use the simplified or the full map or if it is necessary to use mechanisms of high orders, that need most of the computational effort. For this reason, in this section, the relevance in terms of received power is tested with the different map configurations and mechanism complexities. The scenarios used for the simulations are the ones presented in the previous section, bearing in mind that this relevance may vary significantly depending on the specific scenario, much more than

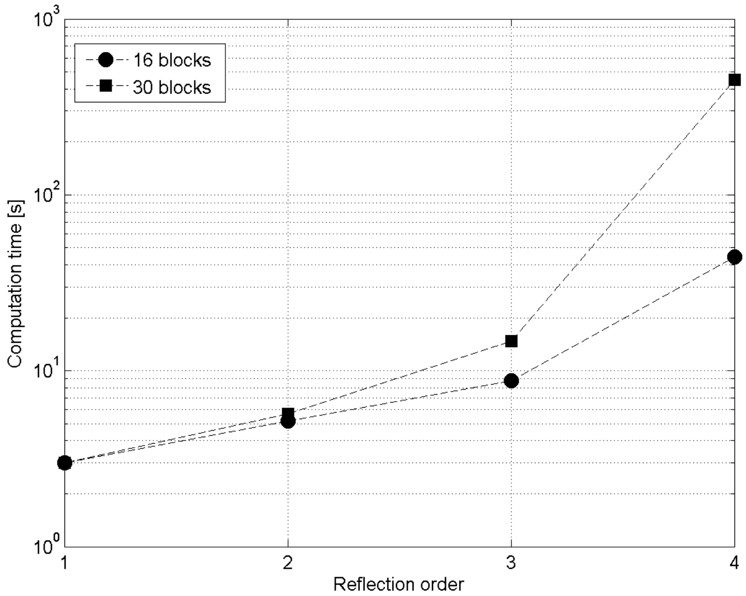

Figure 3.13: Computation time vs. reflection order and number of blocks in outdoor scenario

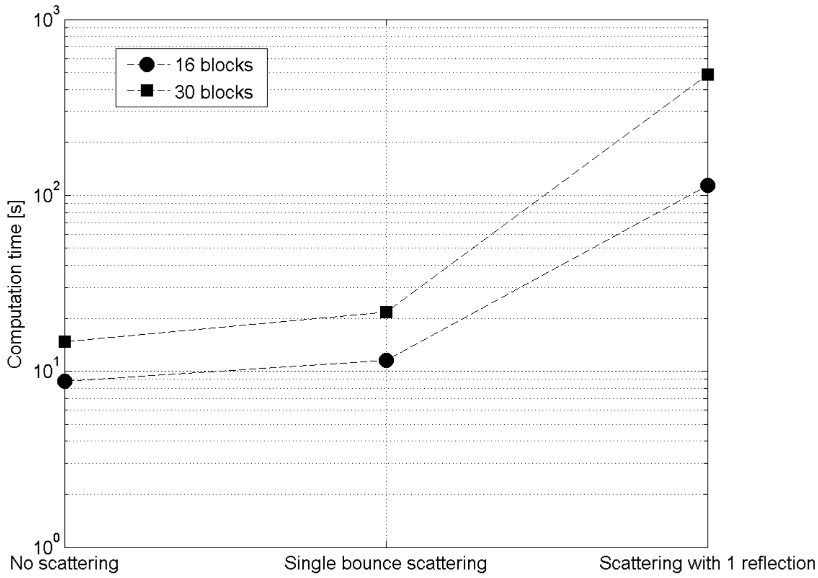

Figure 3.14: Computation time vs. diffuse scattering order and number of blocks in outdoor scenario

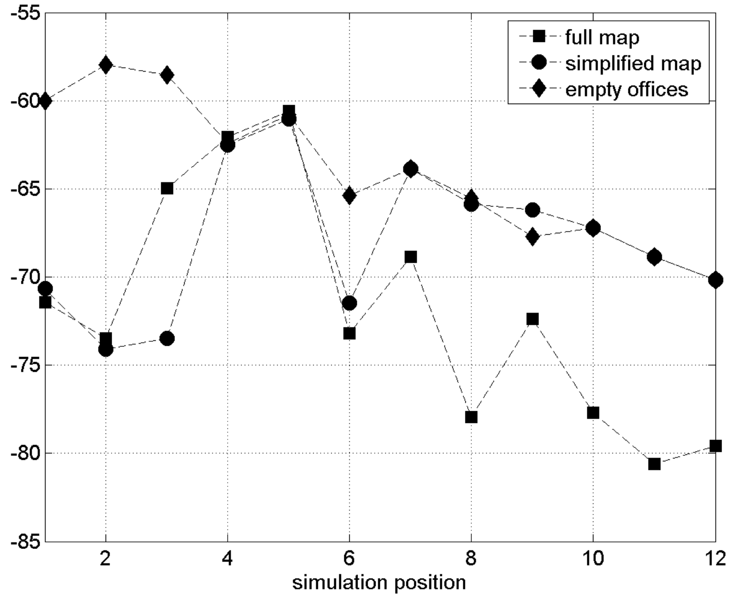

Figure 3.15: Comparison of simulated received power in indoor scenario for different levels of details in the map

the computation time.

Firstly, the feasibility to use a simplified map is tested both in indoor and outdoor scenarios. Fig. 3.15 shows the result in the indoor case and Fig. 3.16 in the outdoor one. The results show an evident difference. In the outdoor scenario, the heuristic selection of relevant buildings shown in Fig. 3.12 produces results similar to the ones with a full map, thus it is meaningful to use a simplified map to reduce the computation time. On the other hand, in the indoor scenario, removing the furniture from the input database introduce differences up to 15dB with respect to the full database. Even considering a compromise, as taking into account only local furniture, is not always feasible, as shown by the results. In fact, some piece of furniture in a room may block or attenuate rays directed to the mobile terminal in another room.

In Figs. 3.17 and 3.18 present a similar test on simplified maps for delay spread, in indoor and outdoor scenarios respectively. To the contrary of what it has been seen for received power, delay spread seems to be marginally affected by a simplification of the input scenario in indoor environment, while a not negligible difference is present in the outdoor one. This can be explained by the fact that delay spread can significantly be affected by multi-path contributions with an elevated delay.

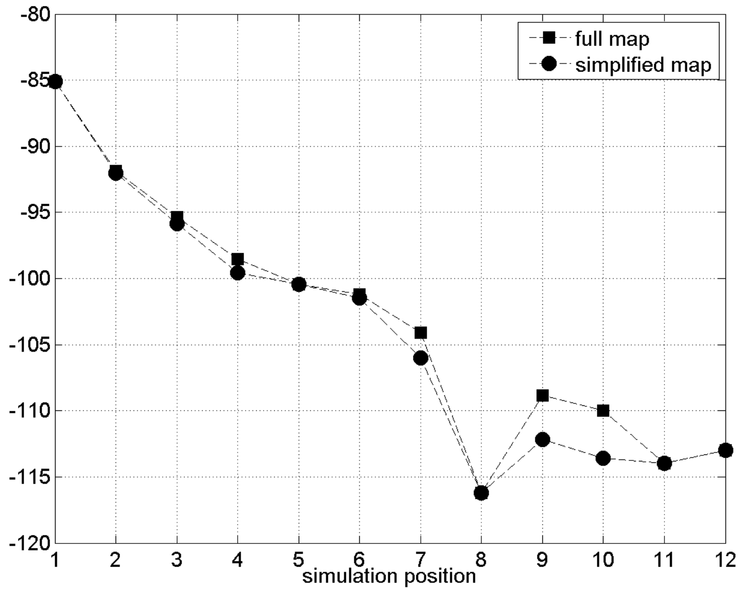

Figure 3.16: Comparison of simulated received power in outdoor scenario for full or simplified map

In the outdoor scenario, the simplified map excludes buildings further away from the terminals that could generate rays yielding a modest amplitude but a high delay. On the other hand, the semplification in the indoor scenario does not affect the size of the simulated scenario, as it is reduced decreasing its accuracy (e.g. not including furniture in the database).

As it is verified in the previous section, the computation time increases significantly when a maximum order higher than 3 is considered or when diffuse scattering is combined together with a single reflection.

The starting point of the following results is simulations with LOS, single diffraction, a maximum reflection order of 4, single bounce diffuse scattering and scattering combined with a single reflection. If the maximum order of reflection is decreased to 3, as shown by Fig. 3.19 and Fig. 3.20 for indoor and outdoor scenarios respectively, the received power is almost not affected. Reflections with an order higher than 3 may have some effect on wide-band characteristics of the channel, e.g. delay spread, but generally speaking the increase in computation time does not correspond to a worthwhile increase in accuracy.

The effect of scattering is presented in Figs. 3.21 and 3.22 for indoor and outdoor case respectively, when full maps are considered. Reduc-

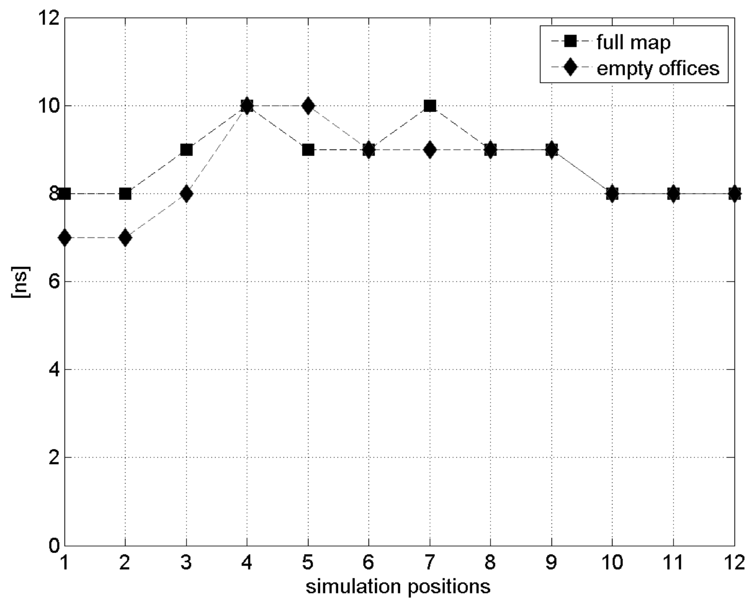

Figure 3.17: Comparison of simulated delay spreads in indoor scenario for full or simplified map

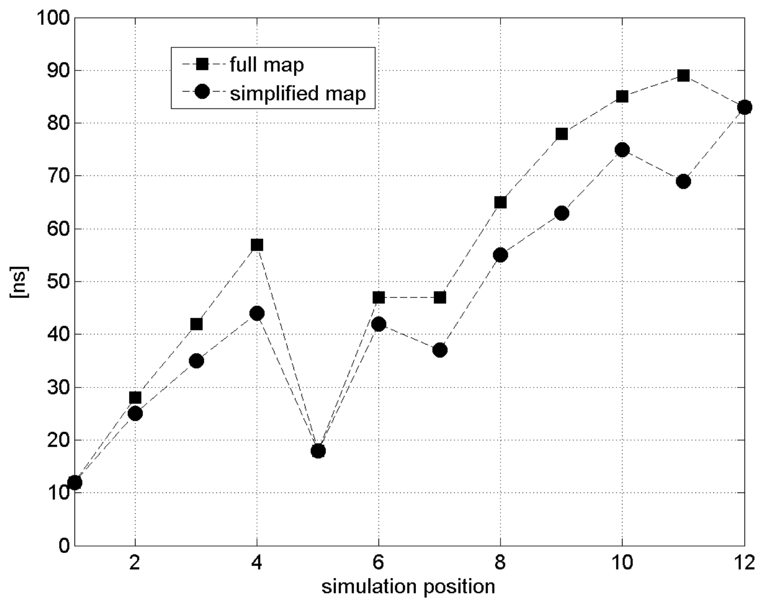

Figure 3.18: Comparison of simulated delay spreads in outdoor scenario for full or simplified map

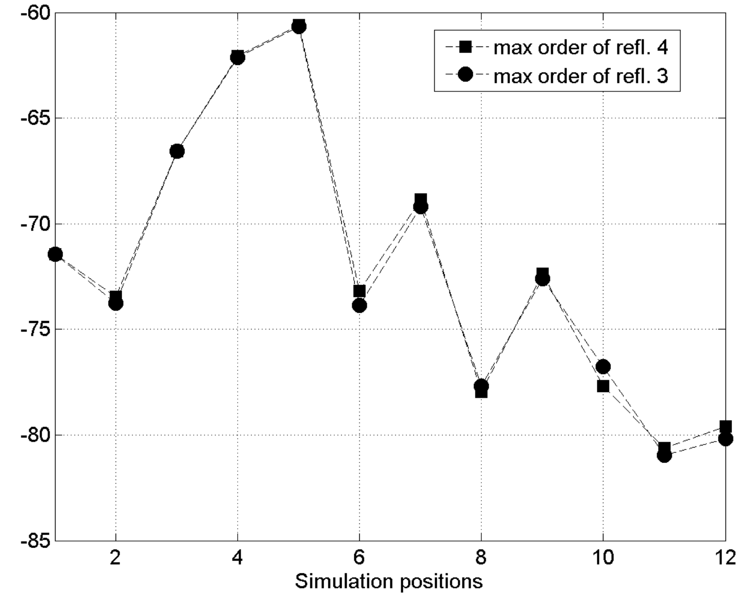

Figure 3.19: Effects on received power of fourh order reflections in indoor scenario

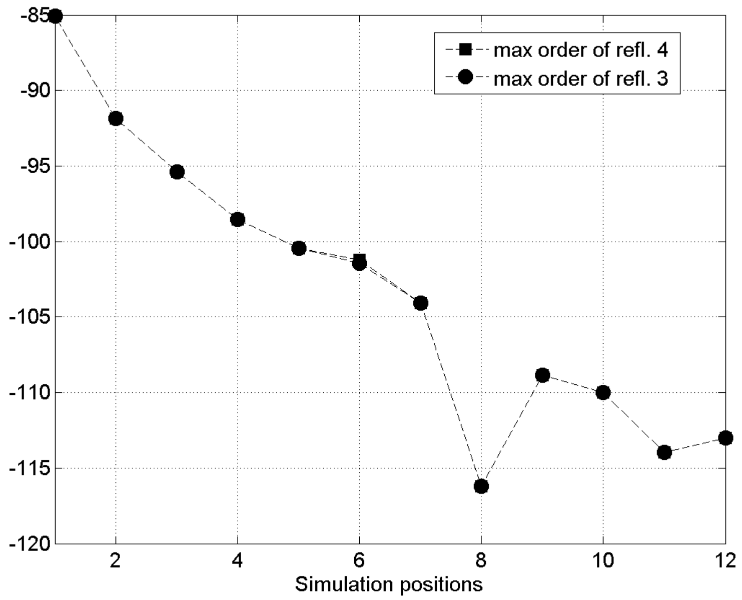

Figure 3.20: Effects on received power of fourh order reflections in outdoor scenario

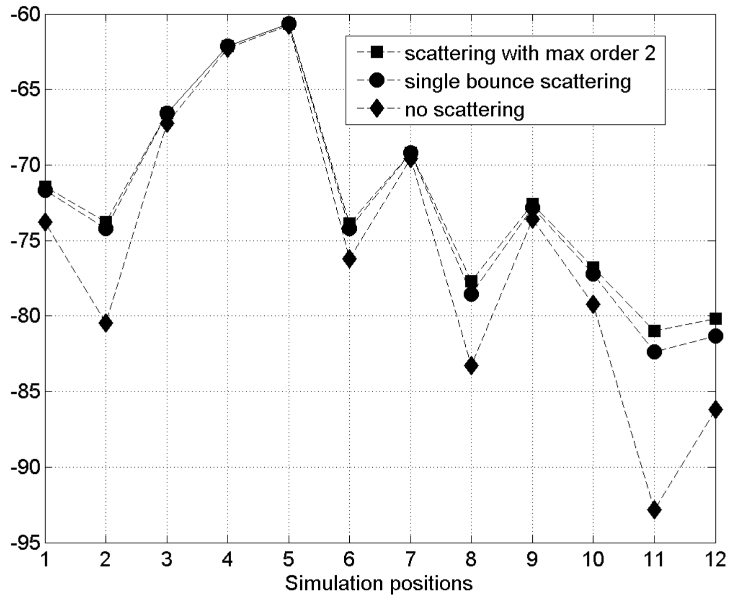

Figure 3.21: Effects on received power of different orders of diffuse scattering in indoor scenario

ing scattering order to single bounce only subtracts from the received power 0.5dB in the indoor scenario and 1dB outdoor scenario. It is more relevant than fourth order reflections but still not very significative. It probably start to be when wide-band characteristics are evaluated. The presence of single bounce scattering, instead, makes a great difference. This is particularly true in the outdoor case where, considering the environment and the position of the mobile terminal, propagation is dominated by diffuse scattering (only few coherent rays are predicted) with the exception of the first postion, where there is a strong LOS.

In conclusion, it is possible to state that, normally, using LOS, single diffraction, a maximum order of reflection equals to 3 and single bounce scattering is enough and this reduces significantly the computation time with respect of situations where higher orders mechanisms are considered. From these preliminary tests, it is also possible to conclude that a simplified map, if chosen wisely, does not affect the prediction in outdoor environment, but it has to be considered carefully in indoor ones, where it may produce relevant errors with respect to the full map.

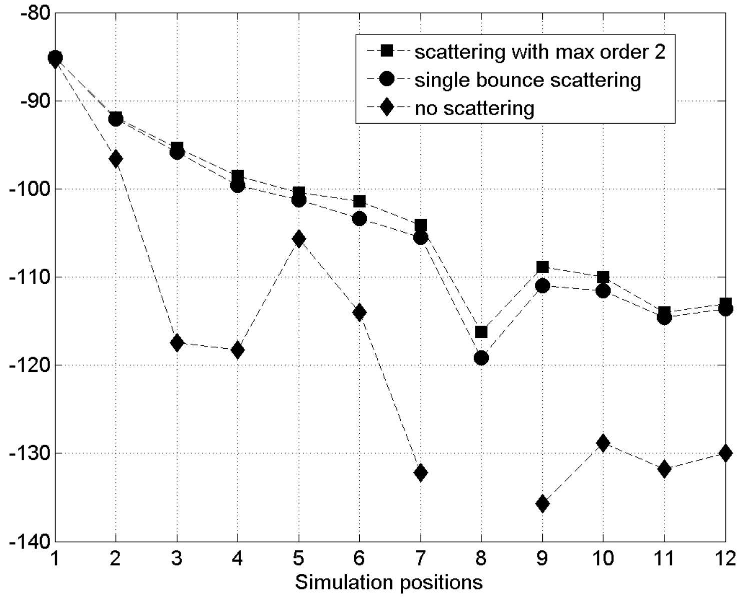

Figure 3.22: Effects on received power of different orders of diffuse scattering in outdoor scenario

3.6.2 Speed-up techniques for Ray-Tracing

The computational complexity of RT is its major drawback, for this reason it is possible to find in literature several techniques to speed-up RT algorithms. Those techniques can be divided in two major groups: the ones operating on the input database and the ones operating on the rays.

The first category includes those techniques which objective is to simplify the complexity of the scenario geometry used as input to run a RT tool. An example can be seen in [56], where an algorithm to identify the significant buildings that contribute to propagation in an urban scenario is presented. The relevant blocks are the ones that falls in at least one of the following categories:

- the ones inside a given elliptic area with the two terminals as foci,
- the ones that can be directly seen by the terminals,
- any other relevant, for its position and shape, building.

In an image theory based RT, the power related to each ray is evaluated in the final part of the calculations, when most of the computational effort is already spent. Hence, it is difficult to decide *a priori* whether a ray is relevant or not. In [56], the field generated by a path related to an image is estimated thanks to a test ray, if the estimation falls below a given threshold, it is discarded. In [28] an illumination zone, i.e. the area related to a given image in which successive images could generate a vaild path, is defined and can reduce significantly the computation time. For indoor environments, in [78], a figure of merit, called degree of visibility, is introduced to discriminate different rays. This figure is equal to the number of blocks that obstructs a path; if a ray yield a degree of visibility that exceeds a given threshold is discarded.

4

Ray-Tracing parametrization and validation in indoor scenarios

In this chapter, the advanced RT, described in Sections 2.5 and 2.4.2 respectively, is validated with measurements in two indoor scenarios [79] with specific focus on penetration and diffuse scattering models. While in outdoor scenarios transmission trough buildings is normally neglected [80], penetration has to be accounted for when an indoor one is considered. This mechanism is particularly important in absence of LOS or when the terminals are positioned in different rooms. On the other hand, in situations when the communication takes place along the horizontal plane, it can be expected that the few oblique rays modeled by RT (e.g. the ones reflected by the floor or the ceiling), even when including penetration, might again not be able to predict the polarization behavior [81]. An important role in the polarization behavior of a channel is played by diffuse scattering, however only few results [82] can be found on its implementation for indoor scenarios. Characterizing the polarization behavior of the channel is important as this information can be used to exploit polarization diversity or polarization multiplexing depending whether orthogonal polarization states are correlated or not.

The first propagation scenario investigated in this chapter is a warehouse. Only few contributions can be found in literature on industrial environments for RT [83] or for general propagation studies [84]. Nevertheless, the analysis of propagation in such environments become more and more important with the increase of wireless systems deployed to control storage or industrial processes. The second scenario, instead, is a classical office one.

In Section 4.3, the prediction capabilities of the RT tool in terms of the angular spreads and spectra of the propagation channel are tested. The main focus is on the angular behavior of diffuse scattering that is studied by comparing RT simulations with experimental data extracted from measurements with an high resolution algorithm in an office scenario.

4.1 Prediction of frequency and polarization selectivity in a warehouse scenario

4.1.1 Measurement description

Measurements were carried out at Transport Pierre in Wavre (Belgium) in a warehouse of approximately 300 m^2 with metallic and wooden containers for the storage of furniture. Building's walls and columns are made of concrete. Fig. 4.1 shows the plan of the warehouse and the position of the receiving (Rx) and transmitting (Tx) antennas. The Rx position is fixed, while Tx is placed in ten different positions that proceed in a clockwise direction from the position labeled Tx_1 to that of Tx_{10}. The scenario was kept static during the measurements. The antennas used for making measurements are linearly polarized, with an azimuth omnidirectional pattern in the frequency range between 800 MHz and 2.5 GHz. The horizontal polarization has been obtained by manual rotation of the antennas. Measurements have been recorded with a SISO Channel Sounder at a frequency of 1.9 GHz with a bandwidth of 80 MHz [85]. The elevation pattern of the antennas at that frequency can be found in [86]. No information on the crosspolar pattern of the antenna is provided by its manufacturer, but measurements of crosspolar discrimination of the antenna have been performed in anechoic chamber. The mean value is 8.2dB with a standard deviation of 6.7dB over all angles.

4.1.2 Simulation results

The simulated 3D environment is created taking into account constituent parts of buildings (i.e. walls, ceiling and floor) and major objects present in the scenario (i.e. the containers). Unless otherwise stated, a maximum of three reflections and a single diffraction are utilized. Diffuse scattering is also included by considering a maximum of two interactions in the simulations. It means that single scattering and scattering before

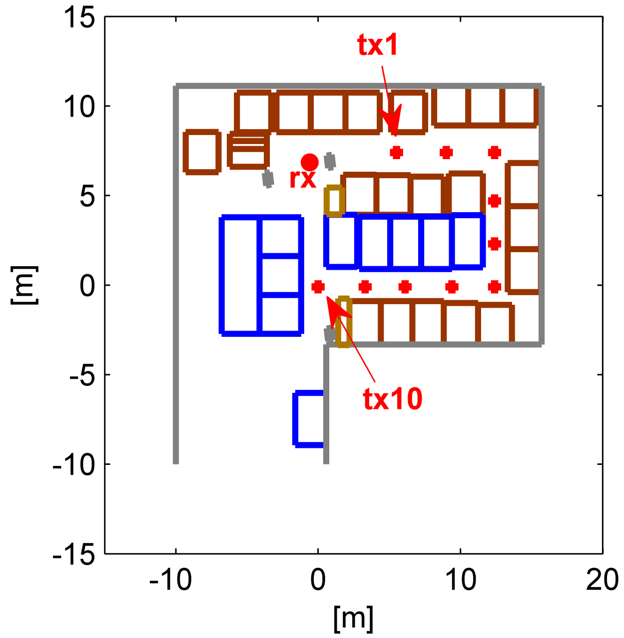

Figure 4.1: Plan of Transport Pierre warehouse where measurements were conducted

Material	ϵ_r	σ $[S/m]$
Concrete walls	8	0.09
Wood	2	0.002

Table 4.1: Material properties at 2 GHz for warehouse scenario

or after a single reflection are included. Penetration is also included unless otherwise stated. Modeling this scenario has been a challenging task, given the presence of a great number of minor objects, e.g. small boxes on top of the containers. Most of them could not be modeled into the input database.

The nominal permittivity, ϵ_r, and conductivity, σ, of the materials present in the warehouse are shown in Table 4.1 [10].

As first step, only penetration is implemented in the RT tool and XPD prediction accuracy is tested with measurements. Fig. 4.2 shows the results of this comparison. It is evident that, despite a small improvement with respect to the results when penetration is not implemented, simulations don't match with measurements with the exception of position 10 that is in LOS conditions. This can be partially explained by considering the row of metallic containers that separates the two ter-

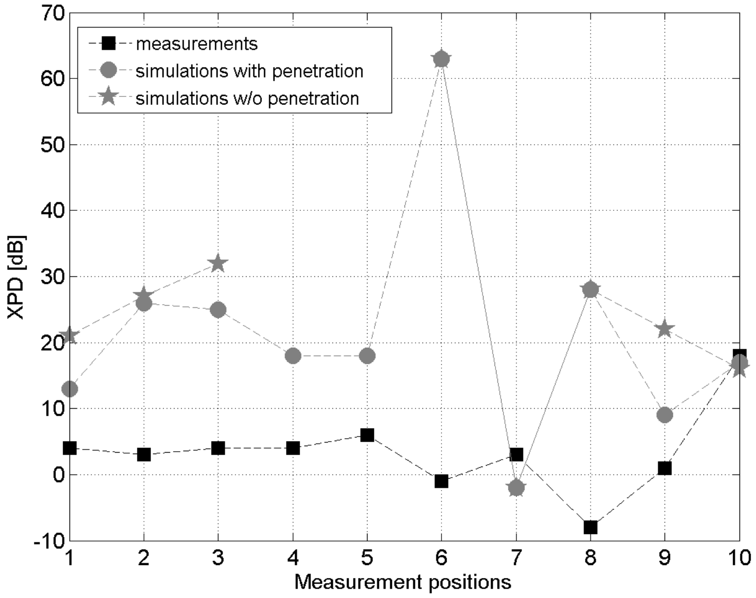

Figure 4.2: Comparison of XPD simulation results with measurements in warehouse scenario when only penetration is implemented

minals when they are in opposite corridors of the warehouse, i.e. the scenario where penetration could have been significant.

Following these considerations, diffuse scattering implementation is tested. The sensitivity of delay spread and XPD with different values of diffuse scattering coefficient S and different scattering pattern models has been tested. The Lambertian model and three directive models, distinguished by α_r values, are considered. It has to be remembered that the higher α_r the narrower the scattering lobe. Table 4.2 shows mean errors in XPD prediction for each value of the scattering coefficient and for each pattern model. The row entitled *Pattern Error* refers to the average error for each pattern model over the different values of S. The column entitled *S Error* is the analogue for the scattering coefficients. A similar comparison has been made for delay spread results. Table 4.3 shows the relative mean errors for delay spread prediction, with respect to the measured delay spread value in each location.

The following conclusions can be drawn from these preliminary results:

- the Lambertian model gives the best results in predicting both XPD and delay spread in this environment,

Table 4.2: Crosspolarization Mean Error in Warehouse Scenario

	Lambertian	$\alpha_r = 2$	$\alpha_r = 3$	$\alpha_r = 4$	S Error
$S = 0.2$	5.1	4.9	4.1	5.8	5
$S = 0.3$	4.3	5.3	6.9	5.3	5.4
$S = 0.4$	3.3	5.6	7.6	4.8	5.3
Pattern Error	4.2	5.3	6.2	5.3	

Table 4.3: Delay Spread Relative Mean Error in Warehouse Scenario

	Lambertian	$\alpha_r = 2$	$\alpha_r = 3$	$\alpha_r = 4$	S Error
$S = 0.2$	0.36	0.35	0.36	0.37	0.36
$S = 0.3$	0.33	0.35	0.36	0.36	0.35
$S = 0.4$	0.33	0.34	0.35	0.36	0.345
Pattern Error	0.34	0.347	0.357	0.363	

- for XPD, the improvement with a Lambertian model is significant while for delay spread is less important,
- scattering coefficient variations do not influence greatly the prediction errors,
- considering Lambertian model, the higher S the lower the errors.

Then, for the following results a Lambertian pattern model with $S = 0.4$ has been chosen. Table 4.4 summarizes the errors and relative standard deviations for this model. The choice of a Lambertian model, where the amplitude of the scattered ray does not depend on the direction of the impinging wave, can be also justified by considering the peculiarity of the scenario. In this case scattering is mainly due to smaller objects that could not be modeled rather than roughness or irregularities in the surfaces. This may be the reason for the Lambertian behavior of the scattering rays.

Fig. 4.3 shows the comparison between measurements and simulations for XPD. The mean prediction error after the scattering implementation is 3.3 dB as shown in Table 4.4. The improvement after diffuse scattering is taken into account is evident. It is possible to conclude that

	Mean Error	Standard Deviation
XPD [dB]	3.3	2.3
Delay Spread [ns]	6.9	4.4

Table 4.4: Summary of the mean prediction errors in warehouse scenario

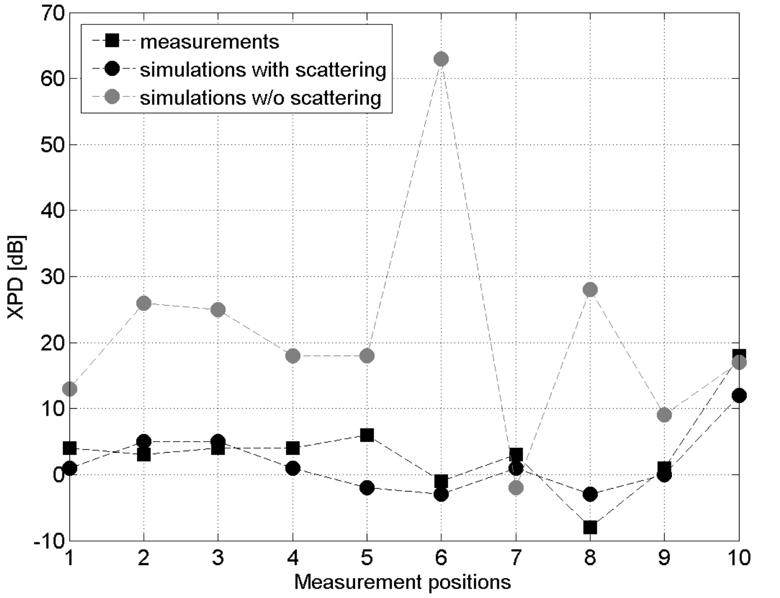

Figure 4.3: Comparison of XPD simulation results with measurements in warehouse scenario

this particular mechanism is the one responsible for the elevated level of power transferred from one polarization to the orthogonal one in this scenario.

Fig. 4.4 shows the comparison between measurements and simulations for delay spread. There appears to be an improvement in the prediction error, mainly in deep non line of sight (NLOS) positions (between 5 and 8). Nevertheless, the measurements are generally underestimated by simulations. To verify a possible improvement in delay spread prediction, the maximum number of reflections has been increased from three to four. The outcome is that there is no significant improvement in the prediction. Moreover, the increase of the maximumt order of reflection incurs in impractical computational times.

4.2 Prediction of frequency and polarization selectivity in an office scenario

4.2.1 Measurement description

This measurement campaign has been performed in an office environment at the Université Libre de Bruxelles (ULB). A floor plan of the

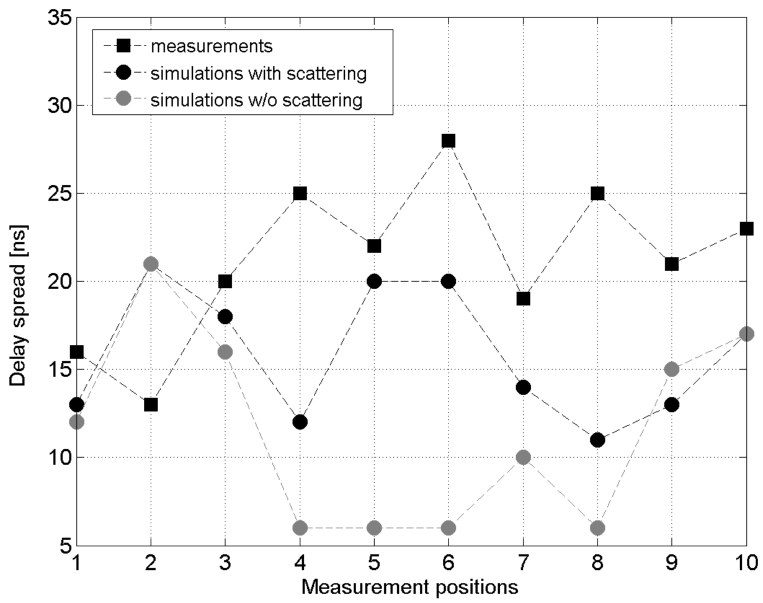

Figure 4.4: Comparison of delay spread simulation results with measurements in warehouse scenario

measurement environment is given in Figure 4.5. The door between Tx and Rx locations remained closed for all the measurements to avoid line-of-sight conditions.

At each measurement location, a 2-level virtual uniform planar array (2L-VUPA) was realized by using an automatic positioning device, yielding a $10 \times 10 \times 2$ virtual array. The elements of the planar array were spaced by $\lambda/3$, and the two levels of the 2L-VUPA were spaced by 1.2λ. The Rx antenna was a tri-pole antenna, composed of three perpendicularly polarized short linear antennas. The θ- and ϕ-radiation patterns of the three antennas of the tri-pole have been measured in an anechoic chamber [87] and the 3D plots are shown in 4.6. The Tx was a vertically polarized log-periodic antenna, which XPD is larger than 15 dB.

At each position of the 2L-VUPA, the frequency response was measured simultaneously on the three Rx antennas with a 4-port VNA. The central working frequency of the VNA was 3.6 GHz, with a bandwidth of 200 MHz. The measurements were performed at night, so that the environment remained entirely static between measurements.

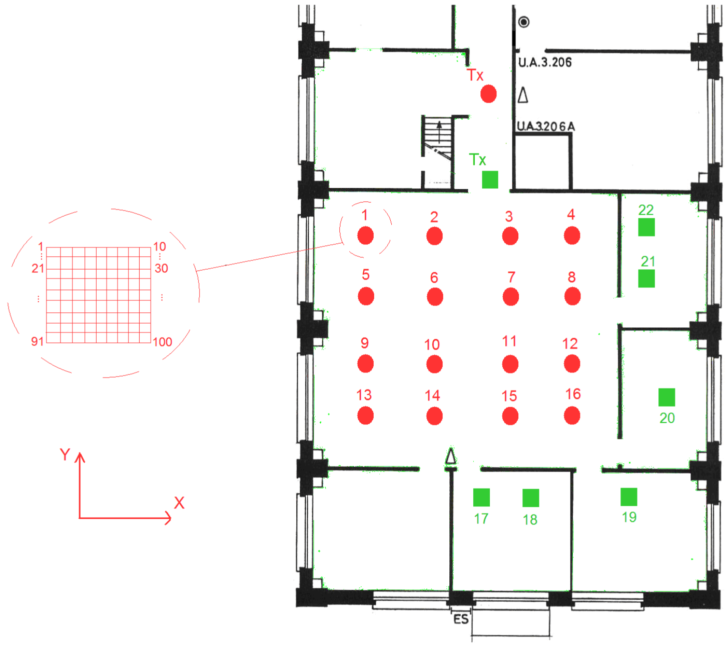

Figure 4.5: Floor plan of the office environment

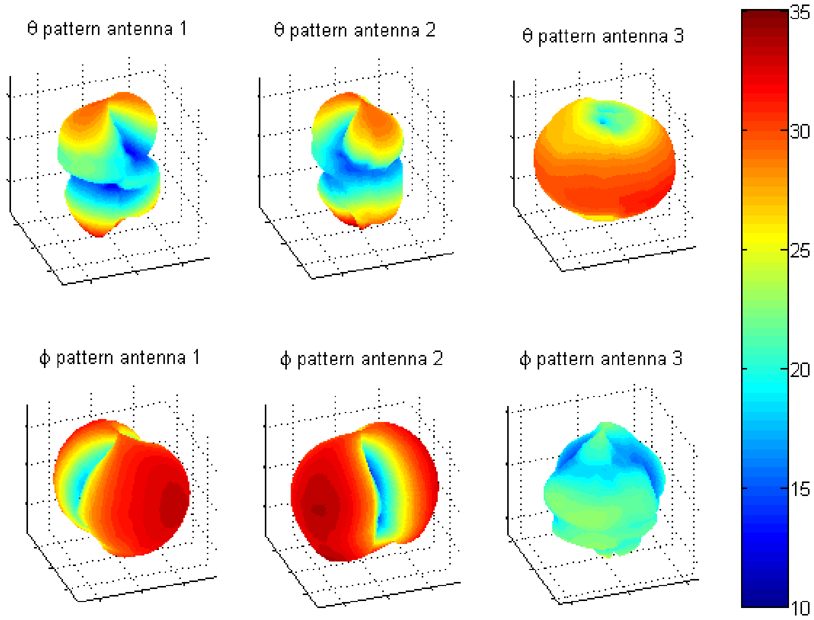

Figure 4.6: Radiation patterns of the tripole antenna

Table 4.5: Materials Properties at 3.6 GHz for office scenario

Material	ϵ_r	$\sigma\,[S/m]$
Brick	4.5	$1 \cdot 10^{-2}$
Concrete	7	$4 \cdot 10^{-3}$
Drywall	2.3	$1 \cdot 10^{-5}$
Glass	4	-
Wood	2	$2 \cdot 10^{-3}$

Table 4.6: Crosspolarization Mean Error [dB] in Office Scenario

	Lambertian	$\alpha_r = 2$	$\alpha_r = 3$	$\alpha_r = 4$	S Error
$S = 0.2$	6.5	6.3	5.7	5.8	6.1
$S = 0.3$	5.7	6.2	5.4	5.7	5.5
$S = 0.4$	6.6	5	6.6	4.8	5.7
Pattern Error	6.3	5.8	5.9	5.4	

4.2.2 Simulation results

The measurement scenario consists of a main hall, surrounded by offices. The rooms are filled with tables and furniture, and the walls are composed partly of drywalls and partly of brick walls. The labs and offices are also surrounded by several windows.

Table 4.5 shows the permittivity, ϵ_r, and conductivity, σ, values of the materials present in the propagation scenario at 3.6 GHz [88, 89, 90, 91].

It is important to note that without the implementation of penetration, no results could be obtained in any position since the Rx and Tx are always separated by a door or a wall. Unless otherwise stated, for XPD evaluations, at Rx side the antenna oriented along $\hat{x}$ is considered, referring to the coordinate system shown in Fig. 4.5.

By analogy with the warehouse scenario, Table 4.6 shows the variations of XPD mean error with the scattering parameters. The columns entitled α_r refer to a directive pattern model with the relative lobe width. Table 4.7 shows delay spread relative mean errors for each value of the scattering coefficient and for each pattern model.

Looking at Table 4.7, it is clear that in this scenario the choice between different scattering coefficients and models does not influence significantly the prediction error for delay spread. This error is, in any circumstance, about 30%. Considering XPD prediction, it is possible to conclude that the choice of S does not change the error significantly, but on the other hand directive models with an higher value of α_r seem to

Table 4.7: Delay Spread Relative Mean Error in Office Scenario

	Lambertian	$\alpha_r = 2$	$\alpha_r = 3$	$\alpha_r = 4$	S Error
$S = 0.2$	0.29	0.3	0.29	0.3	0.295
$S = 0.3$	0.29	0.3	0.3	0.32	0.303
$S = 0.4$	0.3	0.31	0.29	0.3	0.3
Pattern Error	0.293	0.303	0.293	0.307	

	Error	Standard Deviation
XPD [dB]	4.8	3.7
Delay Spread [ns]	5.8	4.7

Table 4.8: Summary of the mean prediction erros in office scenario

perform better. Following the results of the sensitivity test on scattering parameters, the chosen model is a directive model with $\alpha_r = 4$ and $S = 0.4$. Table 4.8 shows a summary of errors and relative standard deviations when this model is considered. By contrast of what it has been said for the warehouse scenario, here the objects that are not modeled in the input database are few (e.g. chairs) and the irregularities are less evident. Thus, a directive model as best match seems reasonable. Simulated results with and without the implementation of diffuse scattering are now presented to validate the model. If scattering is not included, no ray is predicted arriving at the Rx in positions 20 and 21.

Fig. 4.7 shows the comparison between measurements and simulations for XPD. The results show a general improvement when scattering is included in the simulations. In particular the improvement is significant in the first two rows of measurements in the hall (positions 1 to 8) and in the offices (positions 17 to 22). On the other hand, in the last two rows of measurements (positions 9 to 16) in the hall, the accuracy is not improved significantly when diffuse scattering is included. The mean prediction error is 4.8 dB as shown in Table 4.6. Fig. 4.8 shows the XPD comparison where at Rx side the antenna along $\hat{y}$ is considered (in the previous results it was the one along $\hat{x}$). Conclusions similar to the ones presented for the other polarization of Rx antenna may be drawn. The difference is that the mean prediction error, when scattering is included, drops to 3.3dB with a standard deviation of 2.7dB. Moreover in this case, the software without scattering fails also in some NLOS positions in the main hall.

Fig. 4.9 shows the comparison between measurements and simulations for delay spread. The results show that including scattering does not improve significantly the prediction accuracy, except in the last three

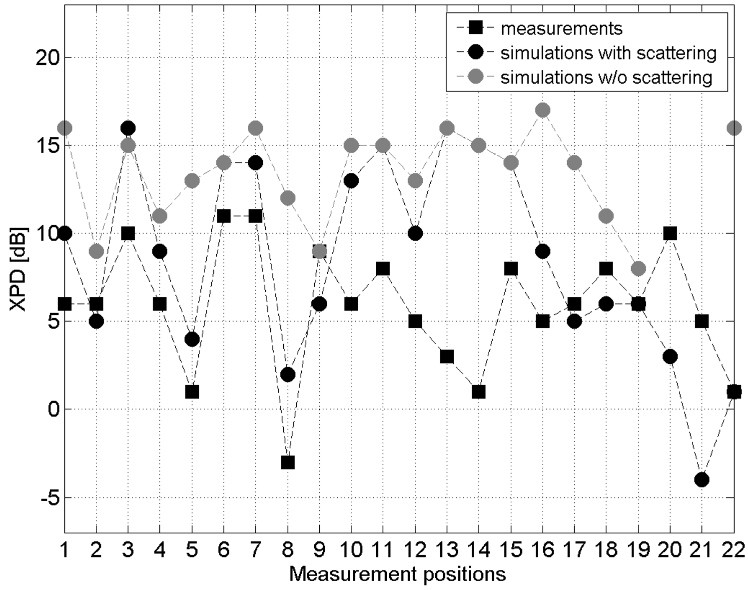

Figure 4.7: Comparison of XPD simulations results and measurements in office scenario

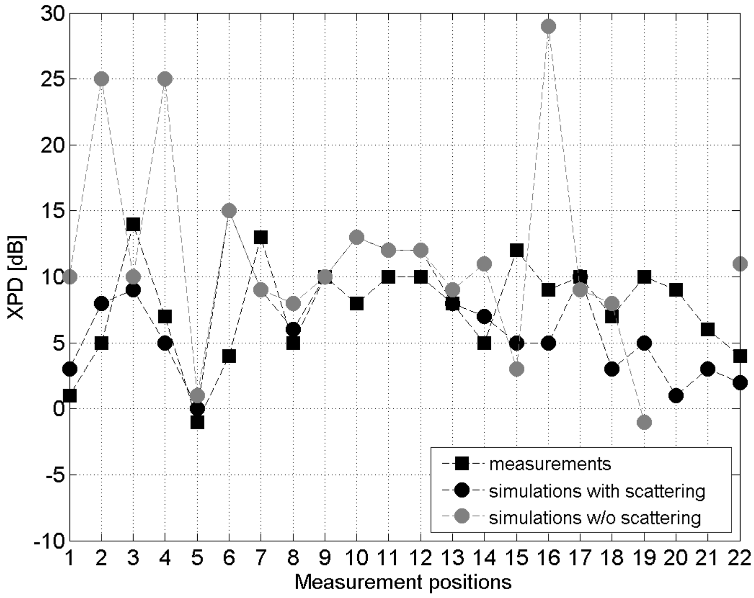

Figure 4.8: Comparison of XPD simulations results and measurements while considering the Rx antenna along $\vec{y}$

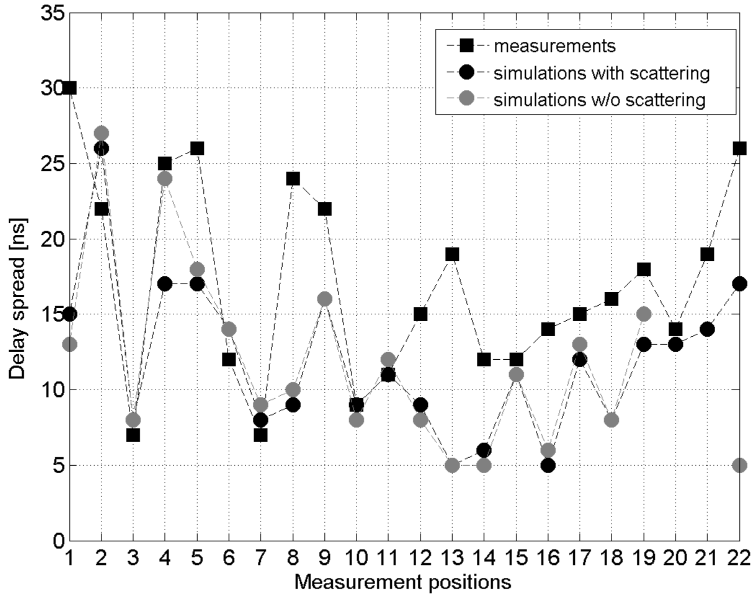

Figure 4.9: Comparison of delay spread simulations results and measurements in office scenario

positions, that can described as deep NLOS, where RT without scattering fails to predict any ray, or a significant number of rays, arriving at the Rx. As in the warehouse scenario, to verify a possible improvement in delay spread prediction, the maximum number of reflections has been increased from three to four. This results in an improvement but minimal and present only in few locations. The relative mean error decreases by 2% whereas the computation time increases by 300%.

4.3 Prediction of directional selectivity

In this section, the prediction capabilities of the RT tool in terms of angular spreads and spectra are tested [92]. A specific focus is dedicated toward the angular behavior of diffuse scattering. A measurement campaign and the related parameter estimation, carried out in [13] to parameterize and validate a Polarized-Diffuse-Directional stochastic channel model, has been exploited to achieve this goal. While doing this, the consistency of the two different approach to model the incoherent part of the channel, diffuse scattering and DMC (see Section 2.4.1), is verified. In the last part of this section the cluster behavior of the scattering component and its tight correlation with specular clusters is investigated

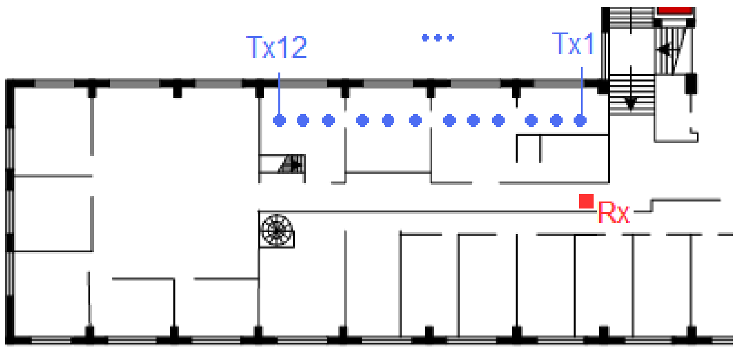

Figure 4.10: Plan of the office scenario with measurement positions

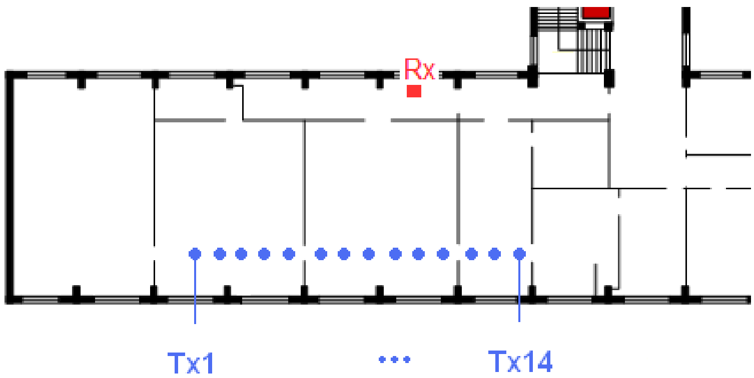

Figure 4.11: Plan of the laboratory scenario with measurement positions

through RT simulations.

4.3.1 Measurement setup

A measurement campaign was conducted in an indoor scenario and two types of indoor environments were considered: an office and a laboratory, as depicted respectively in Fig. 4.10 and Fig. 4.11. In the office scenario the BS was placed in the corridor and the MT was placed in four different offices (between 11 and 24 m^2). The offices were equipped with tables, chairs and closets. In the laboratory scenario, the BS was placed in the corridor and the MT was placed in three different rooms (between 25 and 75 m^2). The labs were wide open rooms, equipped with rows of tables and chairs, and some closets against the walls. For practical reasons the receiver was the BS and the transmitter was the MT.

Measurements were carried out with the ULB/UCL ElektroBit MIMO channel sounder. The receiver was composed of an 8-element dual-polarized uniform linear array, that was placed at the BS side. The array elements were $+45/-45$-dual polarized patch antennas. The MT was composed by a system of three perpendicular linear antennas [87], which was moved with an automatic positioning device to create a virtual $5 \times 5 \times 5$ uniform cubic array. The advantage of such an antenna system is that it is isotropic (i.e. there are no nulls in the radiation pattern of the antenna system). The measurements were recorded by night with no people in the building, so the environment was kept entirely static between measurements. The transmitter and the receiver were connected to share a common clock, in order to avoid sounder phase drift between different elements of the virtual array. The channel sounder was operated at a center frequency of 3.6 GHz and with a bandwidth of 200 MHz. Transmit power was 23 dBm with a code length of 1023 chips, and 8 samples per chip.

4.3.2 Parameter extraction

The specular multipath components (MPCs) were extracted from the data by means of the well-known SAGE high-resolution algorithm [93]. To determine the correct number of MPCs, a large number is first used to keep all significant multipath, but only MPCs with a SNR higher than 6 dB are kept for further analysis [93]. Note that since a linear array was used at the BS, only the azimuth angle was estimated at this side.

The DMC impulse response in delay and angular domains was obtained by subtracting the contribution of the specular MPCs from the measured impulse response. The spectrum of the DMC in the joint transmit/receive angular and delay domains was then extracted using Bartlett's beamforming. Its formulation is the following [94]:

$$h\left(\theta, \phi, \tau\right) = \frac{\sum_{i=1}^{N} h_i\left(\tau\right) B_i\left(\theta, \phi\right) W_i}{\sqrt{\sum_{i=1}^{N} \left|B_i\left(\theta, \phi\right) W_i\right|^2}} \tag{4.1}$$

where $h\left(\theta, \phi, \tau\right)$ is the spatio-temporal spectrum, N is the number of elements, B_i represents the array response of element i and W_i is a Chebyshev window function to reduce sidelobes.

4.3.3 Simulation setup

The description of the scenarios to be simulated, i.e. walls, ceiling, floor and major furniture (tables, desks and closets) is characterized in the

Table 4.9: Dielectric properties of materials

Material	ϵ_r	$\sigma\,[S/m]$
Concrete	6	0.08
Wood	2.1	0.05
Brick	4	0.005
Tiles	3.6	0.002
Drywall	2.4	0.004

input database. The dielectric properties of the materials used in the input database are shown in Table 4.9 [91, 95].

Concerning the specular (or coherent) components, LOS, reflection (with a maximum of three interactions in the chain) and single diffraction are considered. Single bounce scattering and scattering in combination with a single reflection are included in all simulations. A random phase, uniformly distributed, is associated with each diffuse ray. Hence, for each channel simulation, the result is averaged over five realizations to overcome the randomness. A small number of realizations is used because, in the worst case, a standard deviation of $\approx 0.5°$ around the mean angular spread is found. We may, then, conclude that the random phase does not significantly influence the spreads. Penetration is also included for both specular and diffuse components. Finally, given the fact that the high resolution parameter extraction results are antenna de-embedded, no antenna is modeled in the RT tool, so that the comparison between simulations and experimental values is relevant.

The comparison between RT simulations and results obtained from measurements are presented in this section, using the angular spreads as validation metrics. The angular spread is defined as

$$\sigma = \sqrt{\frac{\sum_i P_i \mu_i^2}{\sum_i P_i}} \tag{4.2}$$

where P_i is the power associated with the i^{th} ray and μ_i is given by:

$$\mu_i = \angle e^{j\left(\psi_i - \angle\left(\sum_i P_i e^{j\psi_i}\right)\right)} \tag{4.3}$$

where $\angle$ denotes the argument, ψ_i is the specific angle (azimuth or elevation) on which the spread is calculated which is associated with the i^{th} ray.

It must be noted that at the receiver side, the use of a linear array of four dual-polarized antennas, results in a limited accuracy on the angle spreads extracted from measurements. In particular, no result can be extracted regarding the elevation of arrival (EoA), and the estimation for the azimuth of arrival (AoA) is limited to the main beam width, i.e. between 20° and 160°. The number of antennas limits the beamformer angular resolution, so that only 5° could be obtained for the DMC. The specular components were extracted with a high-resolution algorithm, which is less sensitive to the number of antennas. The precision of the SAGE algorithm was in this case set to 1°. The same resolutions have also been adopted for the RT simulations to have a fair comparison. In any case, given the above considerations, no comparison with measurements can be carried out for EoA, whereas the RT prediction for AoA had to be modified excluding the rays arriving from directions outside the main beam to have a fair comparison.

4.3.4 Diffuse scattering angular spreads

As stated at the beginning of this section, the main goal is to determine the prediction capabilities in terms of angular behavior of diffuse scattering. For this reason, the starting point is the comparison between simulated and extracted from measurements angular spreads of the incoherent part of the received signal.

In Section 4.2.2 a scattering coefficient $S = 0.4$ and a directivity $\alpha_r = 4$ were chosen as reference scattering parameters. A preliminary analysis of the results showed that this values yielded a systematic underestimation of the spreads extracted from measurements. For this reason, a sensitivity test on these two parameters has been carried out to understand the behavior of angular spreads with their variation. For simplicity reasons, the test has been done in one of the two scenarios, the laboratory, on azimuth spreads. At first the scattering coefficient has been fixed to $S = 0.4$. Fig. 4.12 shows the variation of the MREs with α_r. As could have been expected, decreasing α_r, i.e. increasing the width of the scattering lobe, increases the angular spreads and thus reduces the underestimation. Once $\alpha_r = 1$ is set, Fig. 4.13 shows the variation of the MRE with S. The explanation of the decrease of the error with S is less intuitive. Moreover, considering that the variation of the scattering coefficient affects in a significant way other channel characteristics, e.g. pathloss or cross-polarization discrimination, it has been decided to keep the original value of $S = 0.4$. Following these considerations, the simulated results presented in this section are made with scattering parameters $S = 0.4$ and $\alpha_r = 1$.

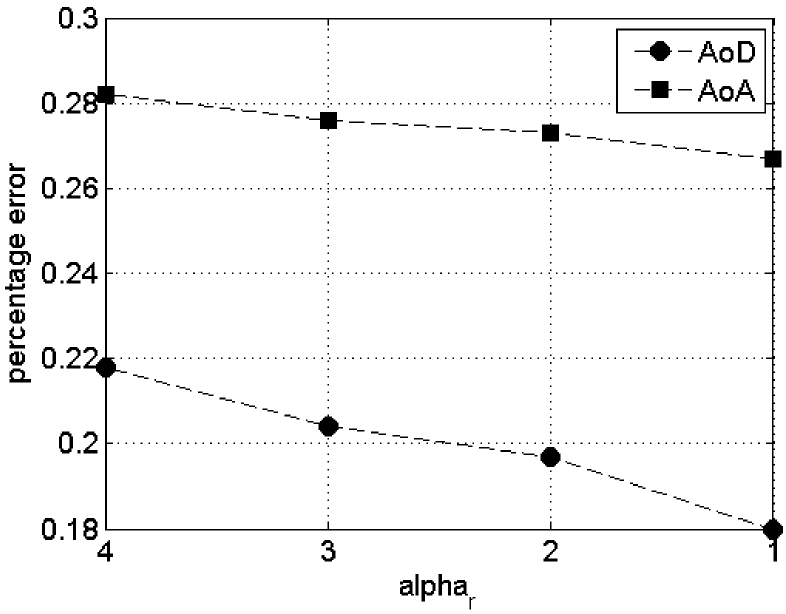

Figure 4.12: Trend of the mean relative errors of AoA and AoD in laboratory scenario whit the variation of α_r and $S = 0.4$

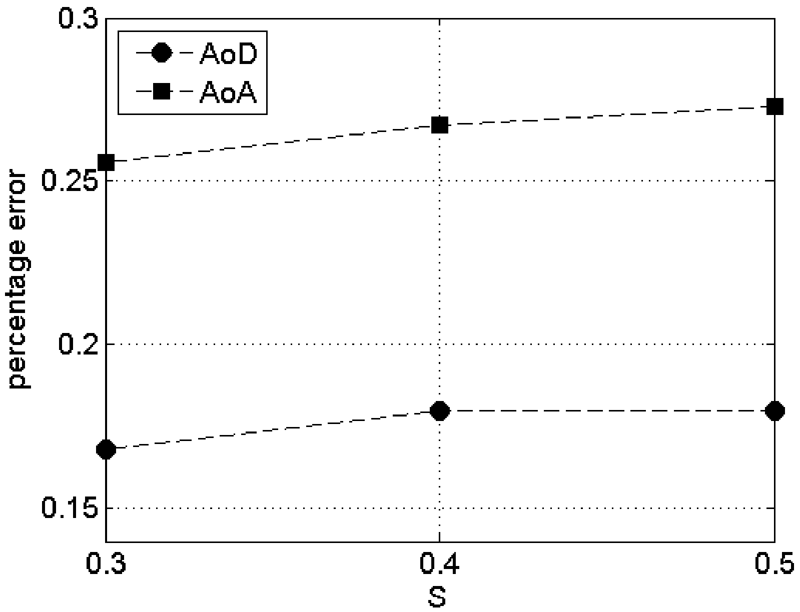

Figure 4.13: Trend of the MRE of AoA and AoD in laboratory scenario whit the variation of S and $\alpha_r = 1$

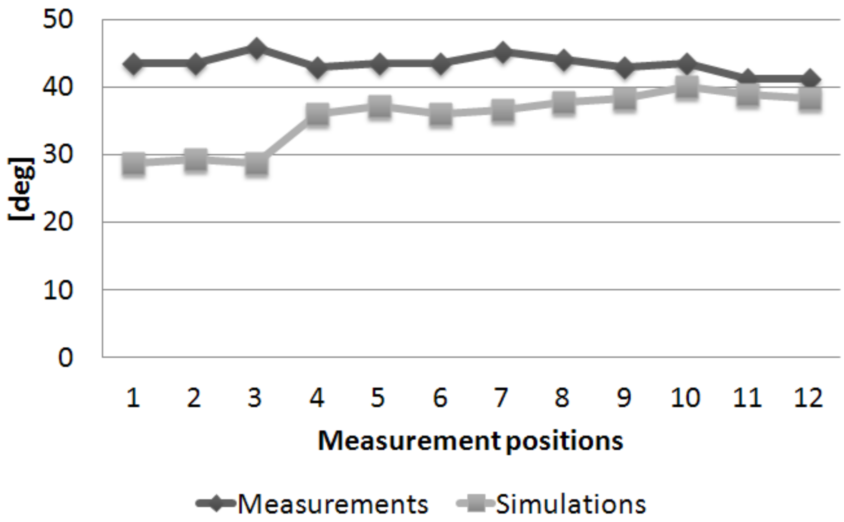

Figure 4.14: AoA spread in office scenario for diffuse component

Table 4.10: Average prediction errors on DMC angular spreads in office scenario

	RMSE	MRE
AoA	9°	17%
AoD	14°	14%
EoD	2°	5%

Office scenario

Fig. 4.14 to Fig. 4.16 illustrate the comparison respectively for AoA spread, Azimuth of Departure (AoD) spread and Elevation of Departure (EoD) spread in the office scenario. Azimuth results show a fairly good agreement while the EoD spread in Fig. 4.16 is clearly underestimated by ray-tracing. The reason for this is that diffuse scattering contributions from ceiling are excluded because of the associated computational cost. When they are added, as in Fig 4.17, the EoD spread prediction improves significantly. In particular the MRE decreases from 31% to 5%. Diffuse scattering by the ceiling also affects the EoA spread, where the mean EoA increases from 14° to 17°. Though in this case there is no comparison with measurements, results limited to simulations are presented in Fig. 4.18.

Table 4.10 summarizes the prediction errors in this scenario. A higher relative error for AoA is expected, considering the limitation of the measurement setting at receiver side.

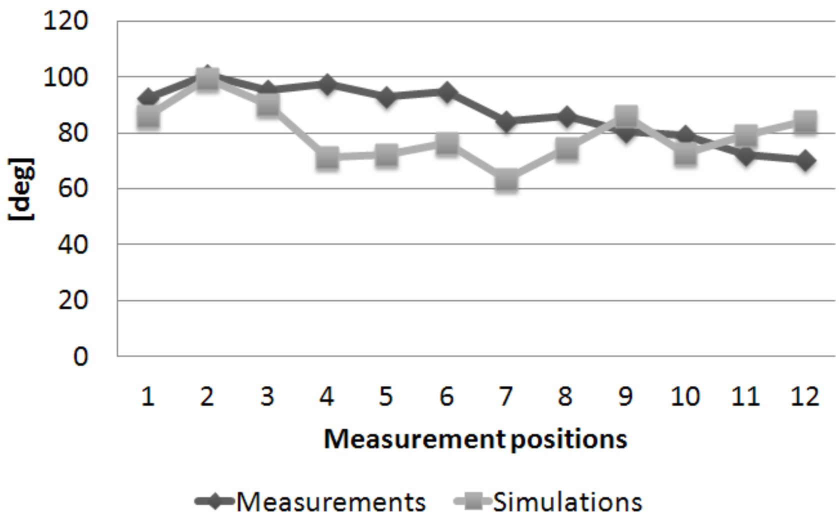

Figure 4.15: AoD spread in office scenario for diffuse component

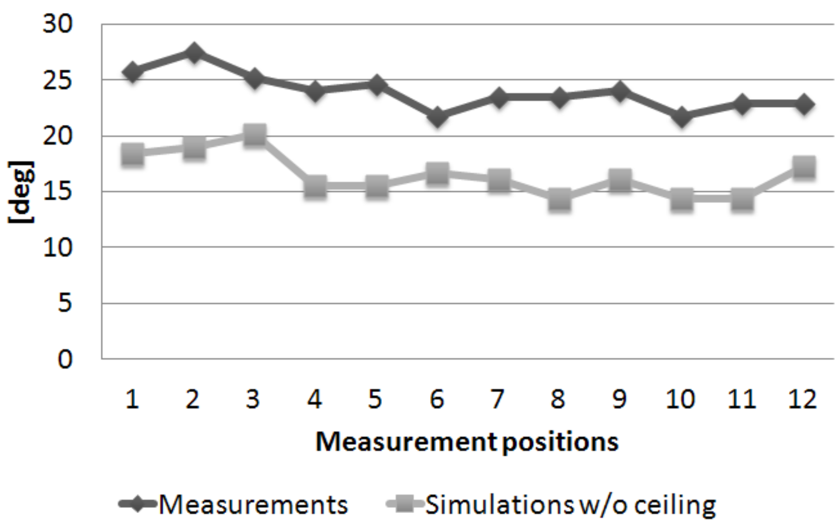

Figure 4.16: EoD spread in office scenario for diffuse component

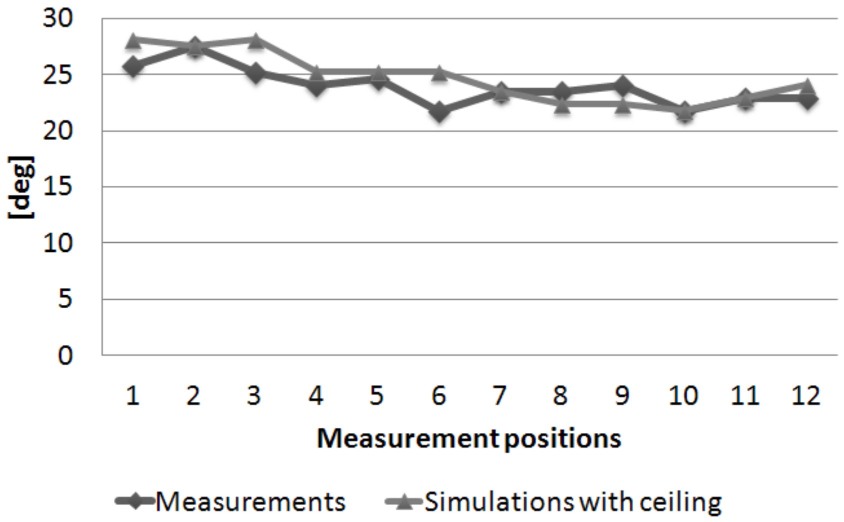

Figure 4.17: EoD spread in office scenario for diffuse component when scattering from ceiling is included

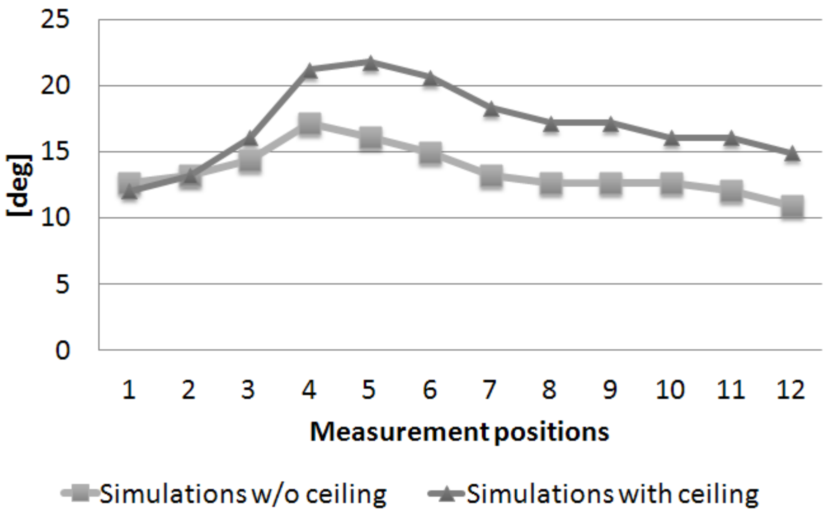

Figure 4.18: Simulations only EoA spread in office scenario for diffuse component when scattering from ceiling is included or not

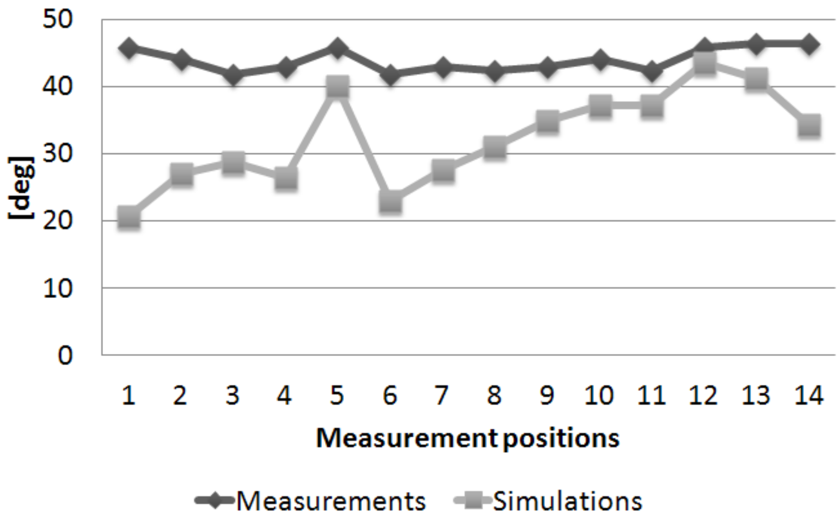

Figure 4.19: AoA spread in laboratory scenario for diffuse component

Table 4.11: Average prediction errors on DMC angular spreads in laboratory scenario

	RMSE	MRE
AoA	13°	27%
AoD	20°	18%
EoD	3°	12%

Laboratory Scenario

In analogy with what has been presented for the office scenario, Figs. from 4.19 to 4.21 compare the experimental and simulated AoA, AoD and EoD spreads in the laboratory environment. Again, the improvement obtained when considering diffuse scattering by the ceiling, as in Fig. 4.21, is evident for EoD spread, where the MRE decreases from 20% to 12%. The mean EoA increases from 14° to 20°, as it is shown in Fig. 4.23, though also in this case no comparison with measurements can be done. In this scenario scattering from ceiling does not have any effect on AoD spread MRE and improves the AoA spread MRE by less than 2%.

The average prediction errors in this scenario are presented in Table 4.11.

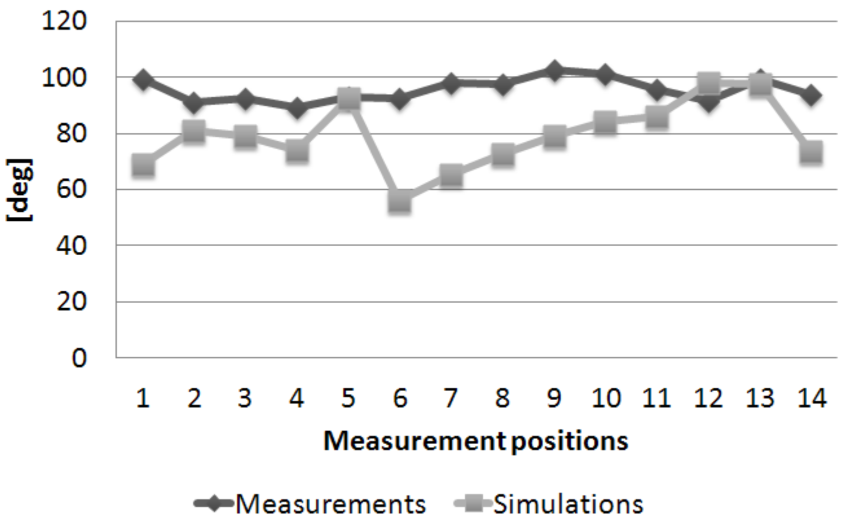

Figure 4.20: AoD spread in laboratory scenario for diffuse component

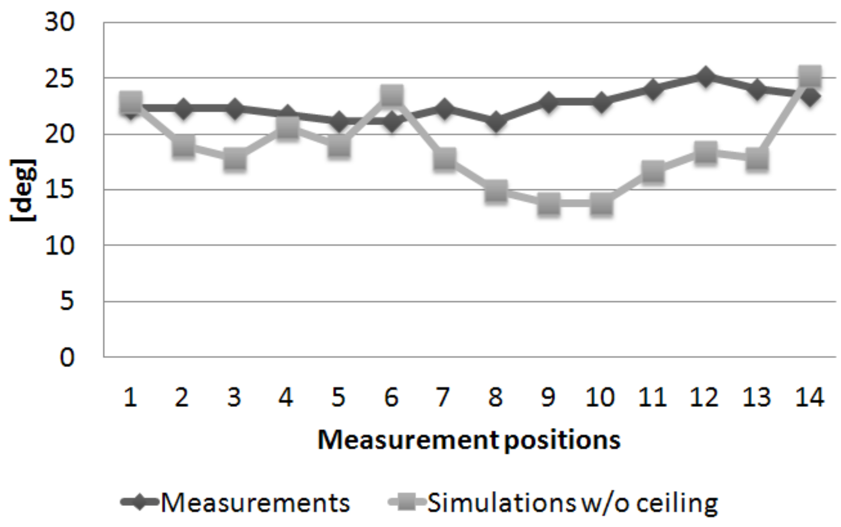

Figure 4.21: EoD spread in laboratory scenario for diffuse component

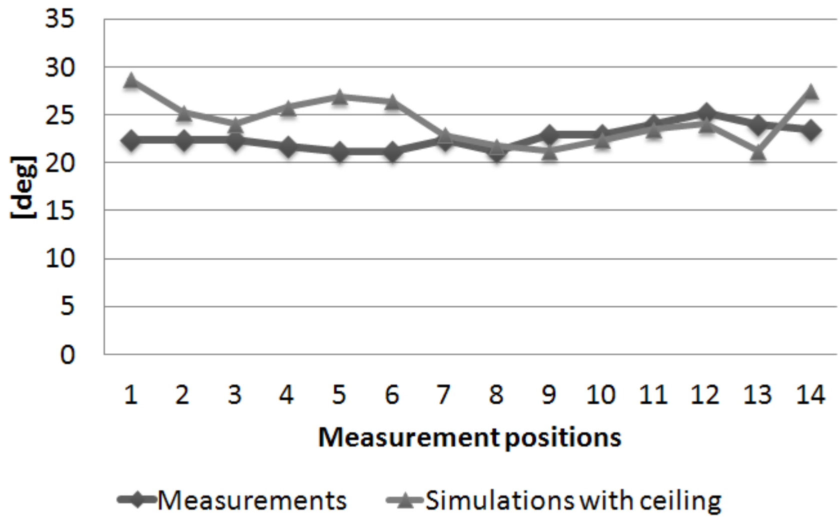

Figure 4.22: EoD spread in laboratory scenario for diffuse component when scattering from ceiling is included

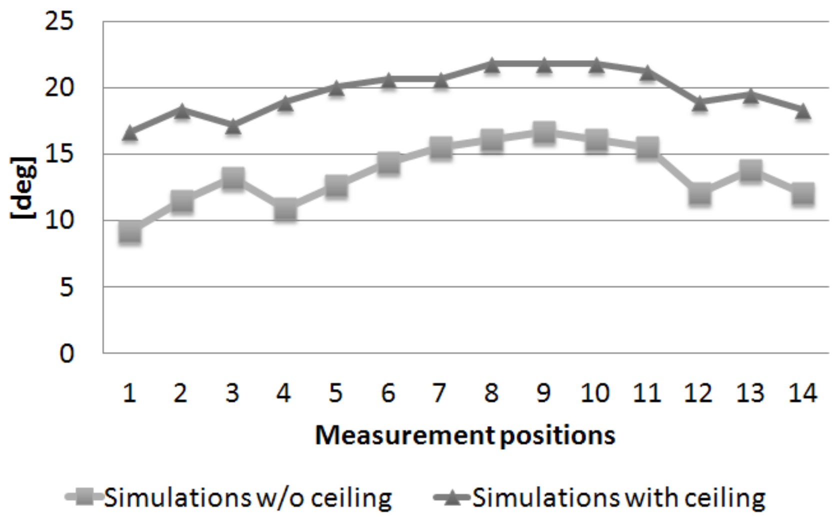

Figure 4.23: Simulations only EoA spread in laboratory scenario for diffuse component when scattering from ceiling is included or not

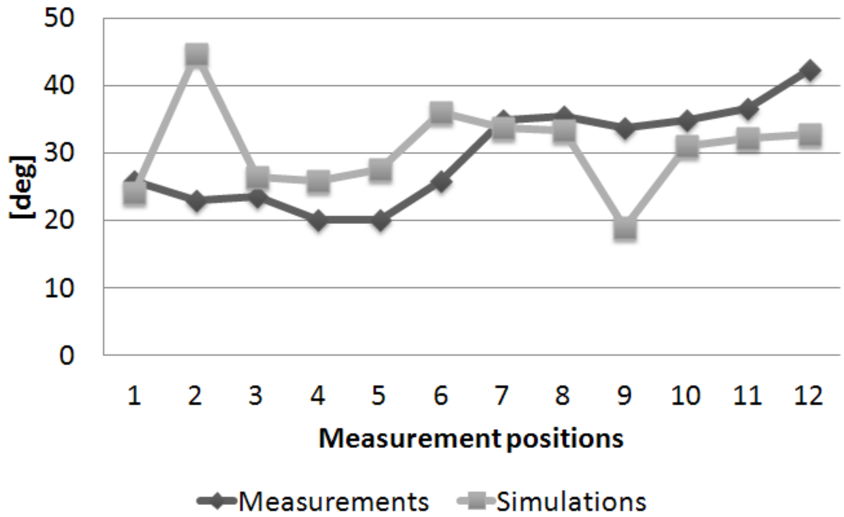

Figure 4.24: AoA spread in office scenario for coherent components

4.3.5 Specular components angular spreads

A similar comparison has been carried out for the specular contributions, i.e. reflections and diffractions. Fig. 4.24, Fig. 4.25 and Fig. 4.26 present the angular spreads for the office scenario. The mean relative error is $\approx 20\%$. The results match reasonably well, partly validating the consistency between both definitions.

In the same way, Fig. 4.27 to Fig. 4.29 show the AoA, AoD and EoD spreads in the laboratory scenario. Here, the prediction is clearly less accurate than in the previous scenario (for AoA, the mean average error reaches $\approx 50\%$), probably because some objects are not modeled in the input database.

4.3.6 Global spreads and general considerations

Global spreads, pertaining to the channel including both specular and diffuse components, have been also evaluated. Tables 4.12 and 4.13 summarizes the mean relative errors in office and laboratory scenario respectively. It can be concluded that the RT prediction relative error is $\approx 20\%$, with the exception of the AoA spread in the laboratory. The standard deviation of the relative error is $\approx 14\%$. Looking at these results, it is possible to come back to the consistency between empirical DMC and ray-based diffuse scattering. An incorrect correspondence between both models would have resulted in a global error lower than both the specular and diffuse errors. If that was the case, one could have

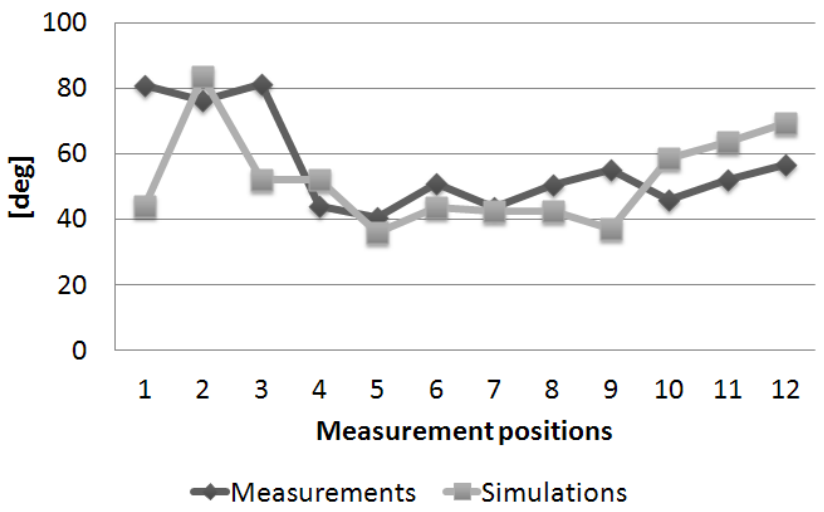

Figure 4.25: AoD spread in office scenario for coherent components

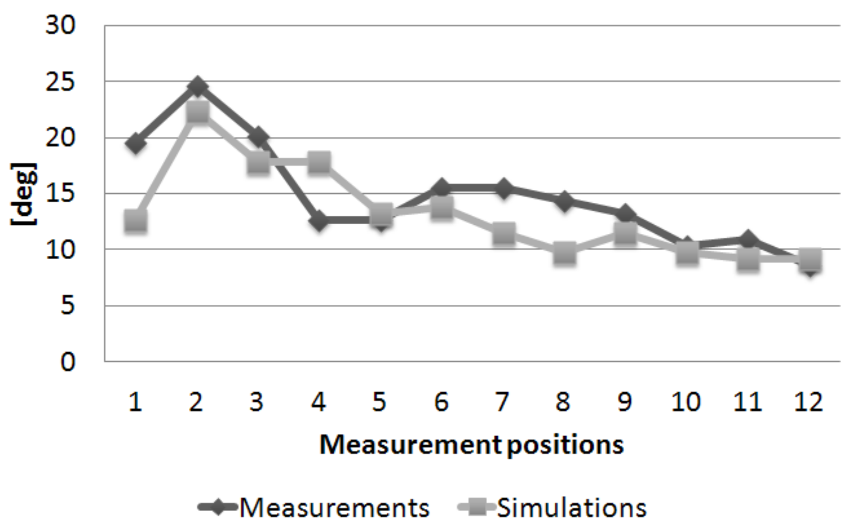

Figure 4.26: EoD spread in office scenario for coherent components

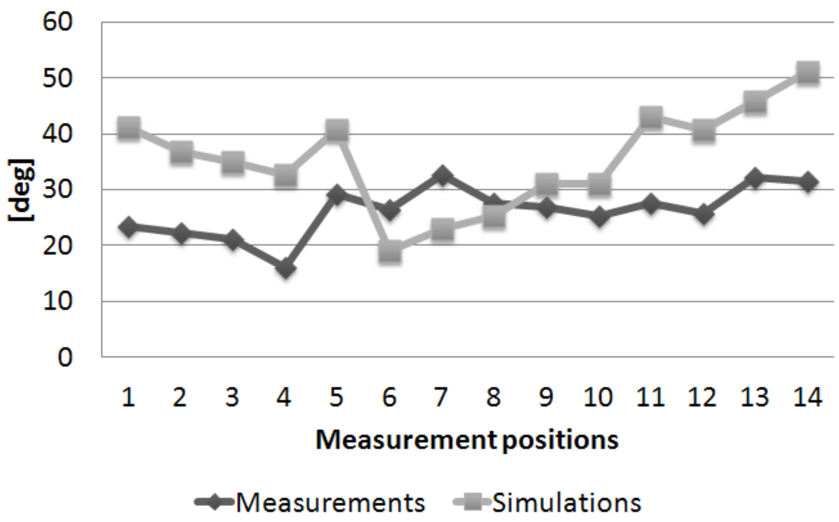

Figure 4.27: AoA spread in laboratory scenario for coherent components

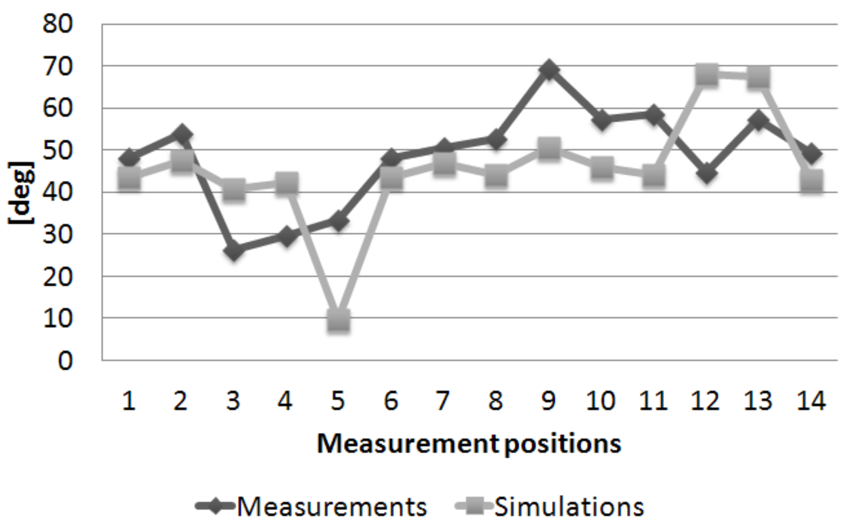

Figure 4.28: AoD spread in laboratory scenario for coherent components

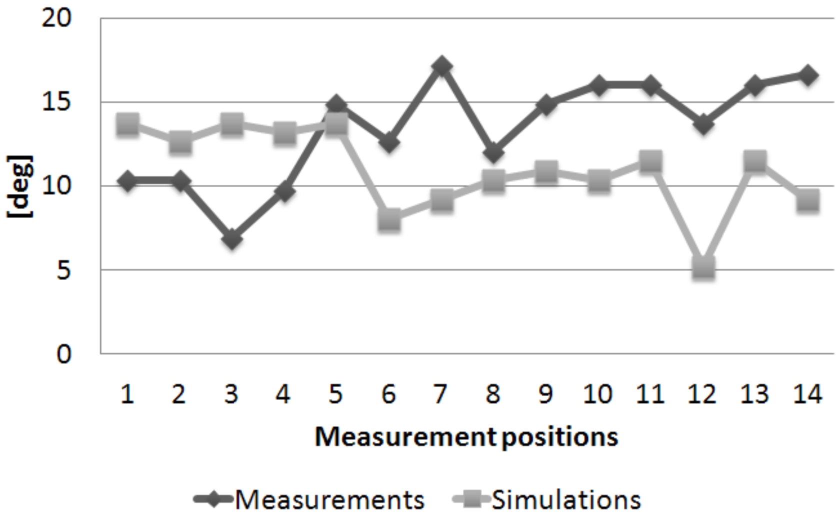

Figure 4.29: EoD spread in laboratory scenario for coherent components

Table 4.12: Mean relative error comparison between global, coherent and diffuse component spreads in office scenario

	Global	Coherent Component	Diffuse Component
AoA	21%	27%	17%
AoD	20%	21%	14%
EoD	18%	17%	11%

concluded that there was a mismatch of what is considered specular and diffuse in the two models, e.g. simulated specular components not found by SAGE and considered DMC. The absence of this phenomenon and the consistency of the errors are an argument in favor of the consistency between the two approaches.

Table 4.14 provides a summary of global RMSEs and standard deviations in both environments. Possible reasons for the discrepancies between measurement-extracted and RT-based values can be classified

Table 4.13: Mean relative error comparison between global, coherent and diffuse component spreads in laboratory scenario

	Global	Coherent Component	Diffuse Component
AoA	29%	48%	27%
AoD	25%	27%	18%
EoD	23%	37%	10%

Table 4.14: Summary of Global RMSEs and Standard Deviations

	Office		Laboratory	
	RMS Error	Std Dev	RMS Error	Std Dev
AoA	6°	3°	11°	5°
AoD	17°	11°	19°	10°
EoD	3°	2°	4°	2°

Table 4.15: Comparison of RMSE of global spreads when diffuse scattering is included or not in the simulations

	Office RMS Errors		Laboratory RMS Errors	
	with d.s.	w/o d.s.	with d.s.	w/o d.s.
AoA	6°	8°	11°	10°
AoD	17°	19°	19°	23°
EoD	3°	5°	4°	7°

into two categories:

- experimental values are extracted from data by means of a high resolution algorithm: this process involves antenna de-embedding and parameter estimation, both of which being the source of errors and possible artifacts;
- the RT approach can be sensitive to the accuracy of the geometrical input database, in particular for indoor settings.

These two facts could possibly explain for outliers in the above graphs, resulting in increasing errors.

Finally, Table 4.15 presents a comparison of RMS Errors with respect to values extracted from measurements for simulated global spreads when diffuse scattering is included or not in the simulations. It is evident that including this feature is significantly beneficial to improve the prediction error. This is not true for laboratory AoA, but this must be put in perspective with the high mis-match between measured and simulated spread for the coherent component (see Fig. 4.27) and the limited accuracy due to the antenna employed at Tx side.

4.3.7 Diffuse scattering cluster behavior

As previously stated in Section 1.1.2, a cluster is defined in GSCM as a group of propagation paths with similar joint angular and delay parameters. Originally it was considered that DMC would have a white angular spectrum [96]. Recently, it has been shown, e.g. in [97], that

- DMC can be described with a clustered behavior, analogous to the specular components in GSCMs,

- there is a tight correlation between DMC and specular clusters [55].

As consequence, in the novel COST 2100 model [98], clusters now include both specular and DMC contributions as co-located.

In a further consistency check between GSCMs and RT, the direction-delay coexistence of specular and diffuse components is investigated, the ultimate goal being to verify the capability of the tool to predict the channel angular behavior at a finer level than the spreads. The results are presented using azimuth-delay spectrum plots of the diffuse scattering component together with a discrete representation of the most powerful specular rays (excluding LOS), for one position in the office and laboratory scenarios.

Fig. 4.32 and Fig. 4.33 present AoA/AoD-delay spectra for position 8 in the laboratory scenario. In a similar way, Fig. 4.30a and Fig. 4.31a show the AoA/AoD-delay spectra respectively, for measurement location 7 in the office scenario. In addition to this, Fig. 4.30b and Fig. 4.31b present the spectra in the same office position, extracted from measurements.

Analyzing the plots it is possible to conclude that the coexistence in the delay-direction domain of the main specular rays and the most significant diffuse contributions is predicted also by the simulations. This seems to confirm the consistency of the apparently different definitions of diffuse scattering (ray-based semi-deterministic versus empirical DMC, defined as what is left out by high resolution algorithms and used in GSCM models). This is promising as one important problem faced by GSCMs is the need for parameterization in many environments: the consistency of between RT and GSCM-based DMC indicates that RT could be used in scenarios where no data is available. Also the comparison with the measured angular spectra seems to bring to a decent accuracy, concerning the diffuse component. In this regard, it is possible to note how measured diffuse components are richer in the delay domain and they have more significant late contributions than the simulated ones. This may show why a lack of accuracy for delay spreads does not correspond to a lack of accuracy for angular spreads.

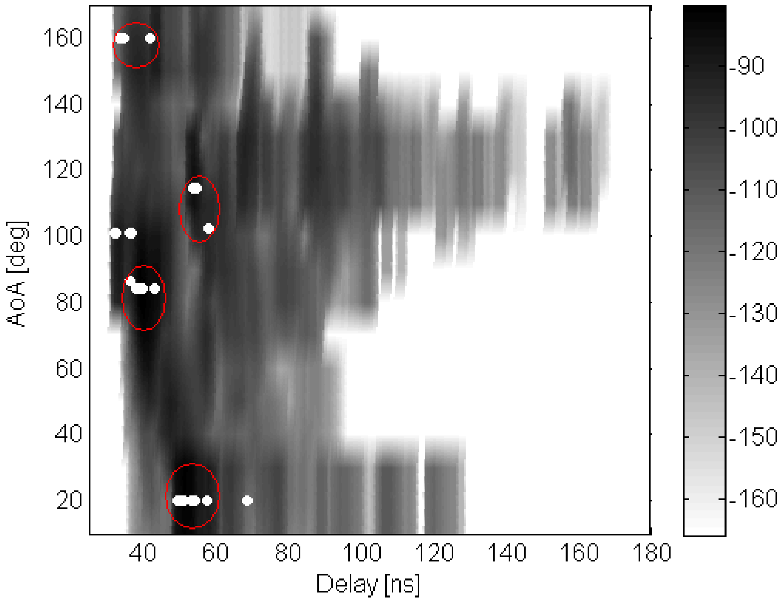

(a) Simulations

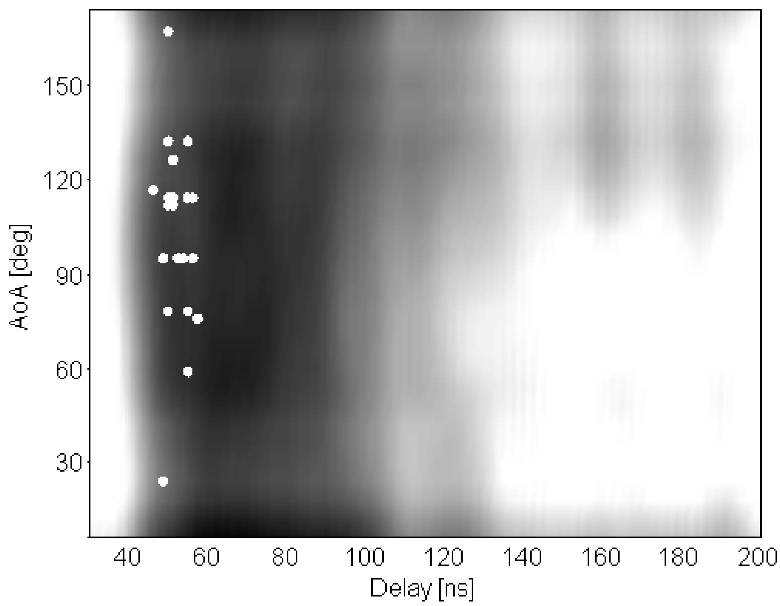

(b) Measurements

Figure 4.30: Diffuse scattering AoA-delay spectrum in office position 7, with main specular contributions indicated by white dots

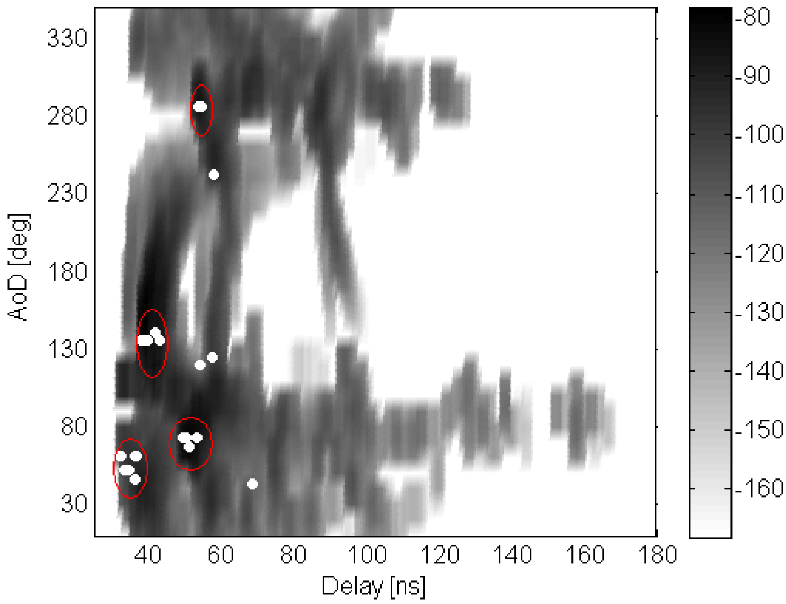

(a) Simulations

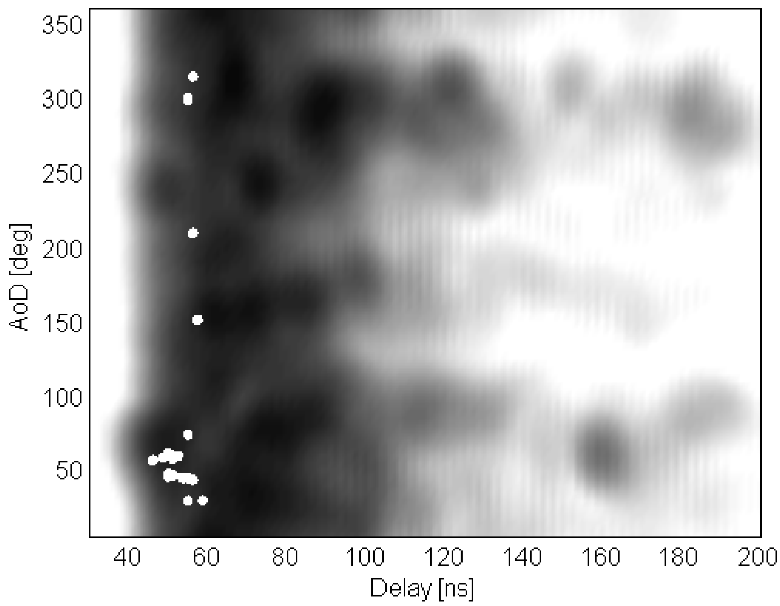

(b) Measurements

Figure 4.31: Diffuse scattering AoD-delay spectrum in office position 7, with main specular contributions indicated by white dots

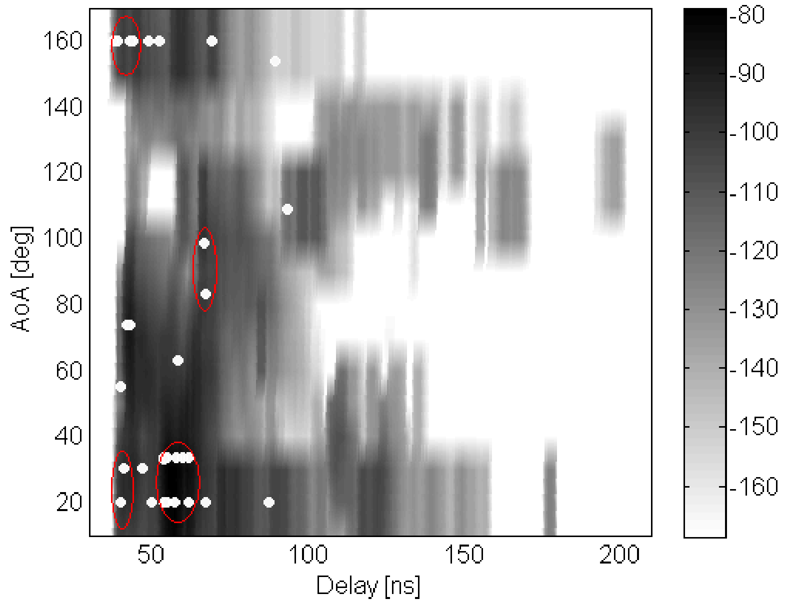

Figure 4.32: Diffuse scattering AoA-delay spectrum in laboratory position 8, with main specular contributions indicated by white dots

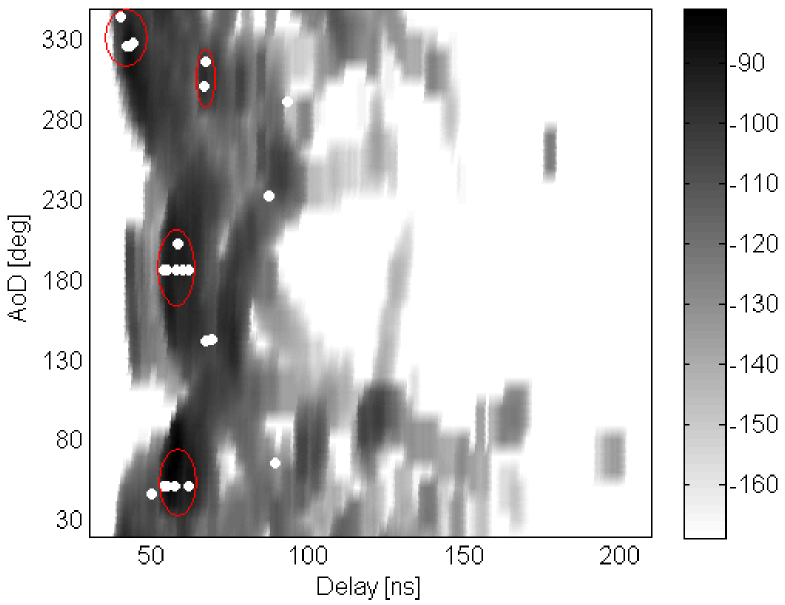

Figure 4.33: Diffuse scattering AoD-delay spectrum in laboratory position 8, with main specular contributions indicated by white dots

4.4 Accuracy of delay spread in indoor scenarios

The capability of RT to accurately predict delay spreads is questionable, e.g. as shown in Figs. 4.4 and 4.9. In this section, in analogy with what it has been done in Section 4.3 for the angular properties of an indoor channel, the prediction capabilities of the RT tool in terms of delay spreads are evaluated for both the specular and the diffuse component of the received signal. The measurement campaign used to validate the simulation results is the one presented in Section 4.3.1. The DMC impulse response in delay and angular domains was obtained by subtracting the contribution of the specular MPCs, extracted from measurement with SAGE algorithm, from the measured impulse response.

The following input parameters are used in the RT simulations:

- the radiation patterns of the antennas employed in the measurement campaign,
- the dielectric properties presented in Table 4.9,
- a maximum order of reflection equal to 3,
- single bounce scattering and scattering combined with single reflection,
- a scattering coefficient $S = 0.4$ and a scattering directivity and a directivity $\alpha_r = 1$.

Fig. 4.34 presents delay spread comparison for the specular component between simulations and values extracted from measurement in the office scenario. Excluding the last three positions, where the simulations significantly underestimate the measurments, the comparison shows a good agreement. On the other hand, the prediction error for the delay spread of the diffuse component is quite large overall, as shown in Fig. 4.35.

Similar results, both for the specular and the diffuse components, are obtained in the laboratory scenario, as shown respectively by Fig. 4.36 and Fig. 4.37.

Figs. 4.38 and 4.39 present a comparison of measured and simulated normalized PDPs in office scenario position 1 for coherent and diffuse components respectively. Analyzing the plots, it is possible to confirm that RT shows some difficulty in predicting contributions arriving with a larger delay. This is even more evident for the diffuse component, as the maximum number of multiple interactions simulated is reduced to a double interaction at most.

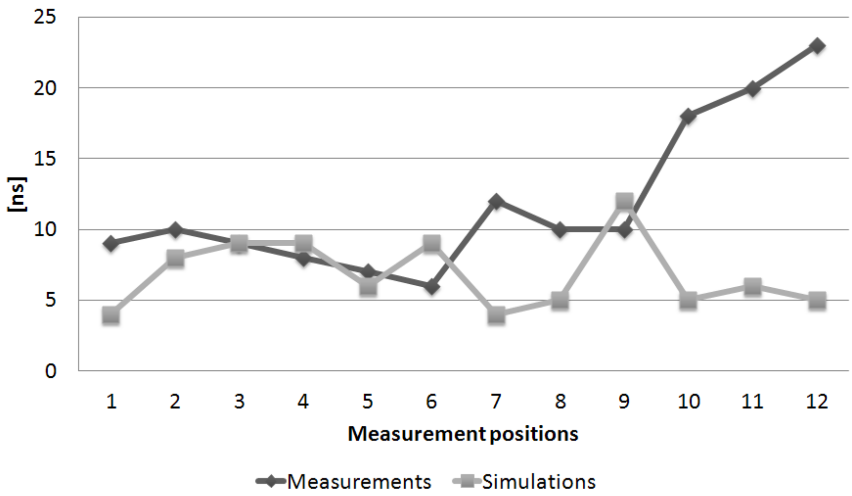

Figure 4.34: Delay spread comparison in office scenario for specular components

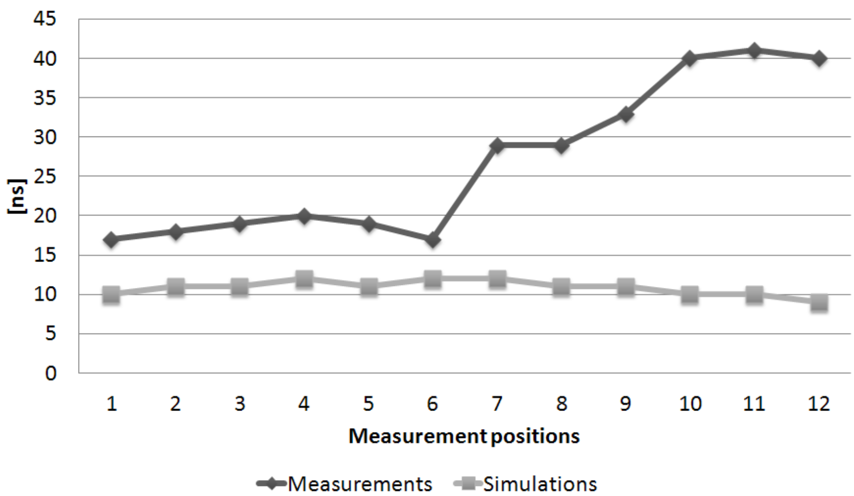

Figure 4.35: Delay spread comparison in office scenario for diffuse components

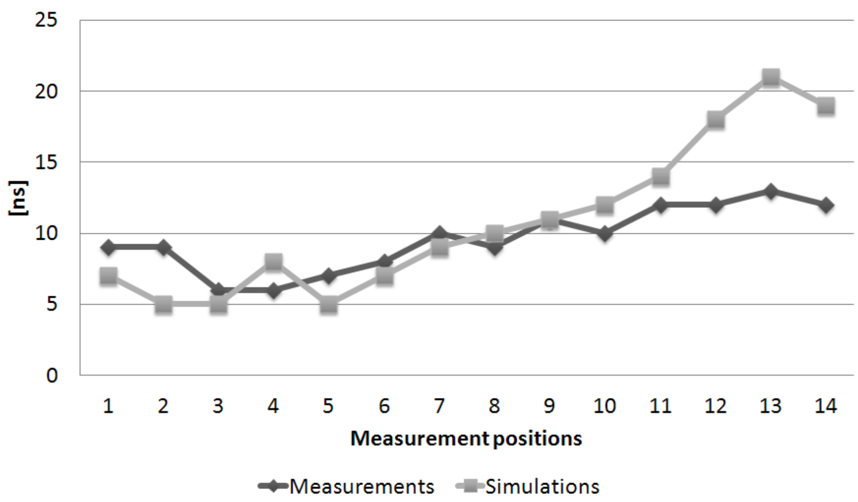

Figure 4.36: Delay spread comparison in laboratory scenario for specular components

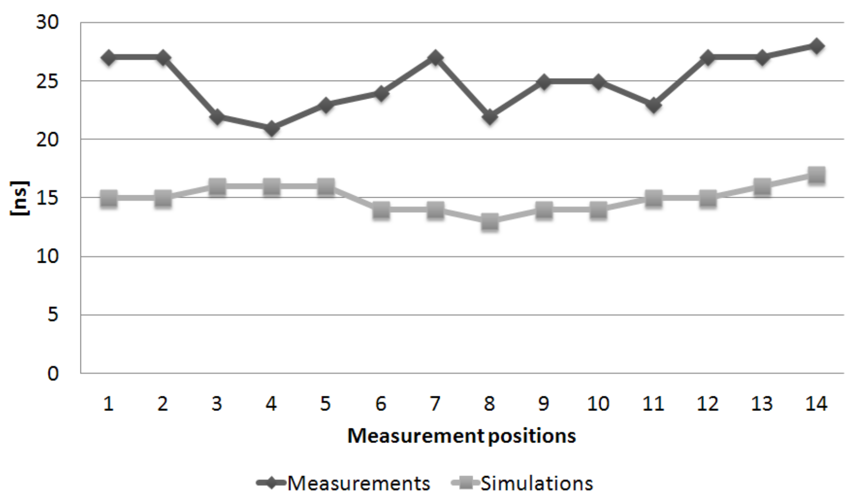

Figure 4.37: Delay spread comparison in laboratory scenario for diffuse components

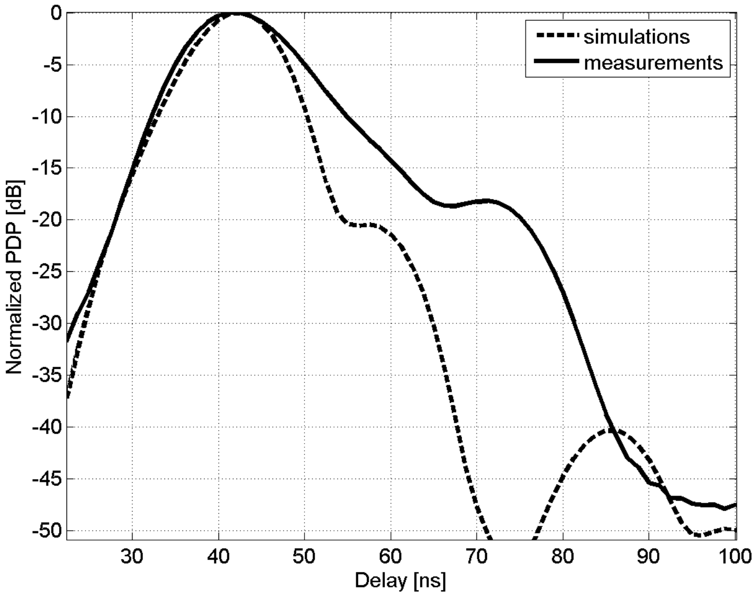

Figure 4.38: Normalized power delay profile for coherent components in office position 1

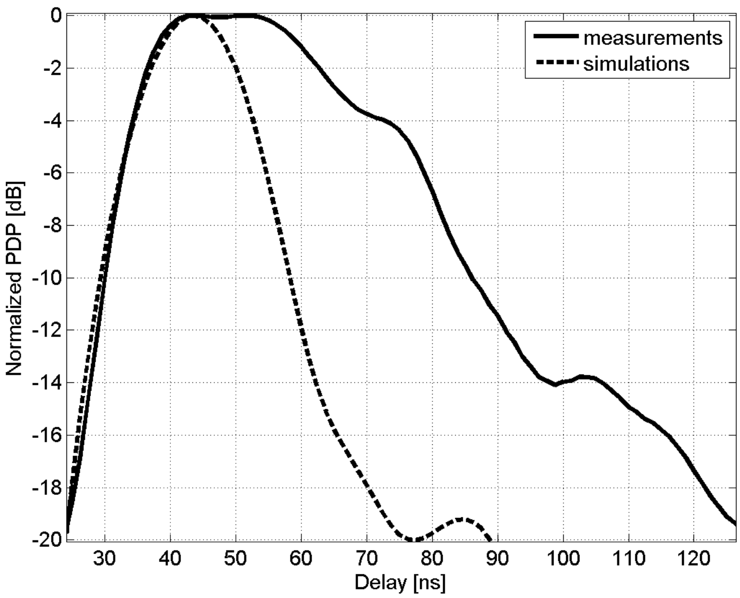

Figure 4.39: Normalized power delay profile for diffuse components in office position 1

4.5 Conclusion

In the first part of this chapter the prediction accuracy of RT including penetration and diffuse scattering has been investigated in two indoor scenarios: a warehouse used for the storage of small containers and classical offices of an university building.

The results showed that penetration is not relevant in the warehouse scenario because of the geometry of the room and the material of the containers, as a row of metallic containers separates the two terminals when they are in opposite parts of the warehouse, thus preventing any penetration. On the other hand, penetration is essential in the office scenario where Tx and Rx are always located in different rooms, thus separated by a door or a wall. An interesting outcome of this study is that while in the warehouse scenario the Lambertian model gives the best prediction, when compared to the measurements, in the office scenario, the best result is achieved by a directive model. This difference can be explained intuitively by noting that in the warehouse scenario, a lot of large objects could not be modelled in the input database, and some surfaces, such as the ceiling, have strong irregularities. In the offices, the irregularities are fewer and smaller. It is consistent, then, that the diffuse rays with higher energy are closer to the direction of specular reflection in this case while they are more randomly distributed in the warehouse.

Following the validation of diffuse scattering with measurements, it is possible to conclude that:

- in LOS (or obstructed LOS in the office scenario) positions, the accuracy of the classic RT tool (neglecting diffuse scattering) is similar to the one of the advanced version,
- the implementation of diffuse scattering is important to model polarization behavior of the channel (e.g. the power transferred from one polarization to its orthogonal) with sufficient accuracy,
- delay spread is generally underestimated; a motivation for this deficiency resides in the limited number of interaction order modeled in the simulations and in the limitation of the scenario described in the input database; even if increasing the complexity of the propagation mechanisms slightly improve the prediction, generally it is at the cost of incurring in impractical computation times.

In the second part of this chapter, the angular behavior of a typical indoor office environment is studied, with specific focus on the angular characteristics of diffuse scattering. Angular spreads have been used as a metric to compare simulation results with values extracted from measurements using SAGE algorithm for MPC and beamforming for DMC. From the comparison between processed measurements and simulations, the following conclusions can be drawn:

- diffuse scattering simulations reproduce with reasonably good accuracy DMC azimuth spreads,
- scattering from ceiling is decisive to obtain a good accuracy on elevation spreads,
- the mean relative error on DMC angular spreads is approximately 20%,
- including diffuse scattering in RT simulations reduces the RMS prediction error.

The cluster behavior of diffuse scattering and its relationship with specular clusters have been also investigated. The results show a coexistence in the direction-delay domain of specular and diffuse scattering main contributions in RT simulations. This is in agreement with what it has been found recently for GSCMs. The conclusion is that RT could be used in place of measurements for the parameterization of those models.

5

Ray-Tracing parametrization and validation in outdoor scenarios

In this chapter, RT simulations are validated with measurements in an outdoor environment.

The first part, based on [99], focuses on the analysis of diffuse scattering contribution in conformity with what has been presented in Chapter 4. Different diffuse scattering parameters are tested and simulation results are compared with measurements in terms of received power, XPD and delay spread. The reference measurement campaign has been carried out in a campus scenario.

In the second part, the scattering by vegetation model presented in Section 2.6 is validated in the same measurement scenario [100]. Together with scattering, another effect is associated with each modeled tree: attenuation. The attenuation that a ray suffers if it intercepts the crown of a tree is evaluated using empirical methods that express the excess attenuation proportionally to the distance covered inside the tree.

5.1 Description of the measurements

The measurement campaign has been performed in a campus scenario in Louvain la Neuve, Belgium. The antennas used for the measurements are two linear arrays of four dual-polarized ($+45°$ and $-45°$ slanted polarizations) patch antennas. Fig. 5.1 shows the map of the measurement scenario. The transmitter, in red in the picture, was placed on the fourth

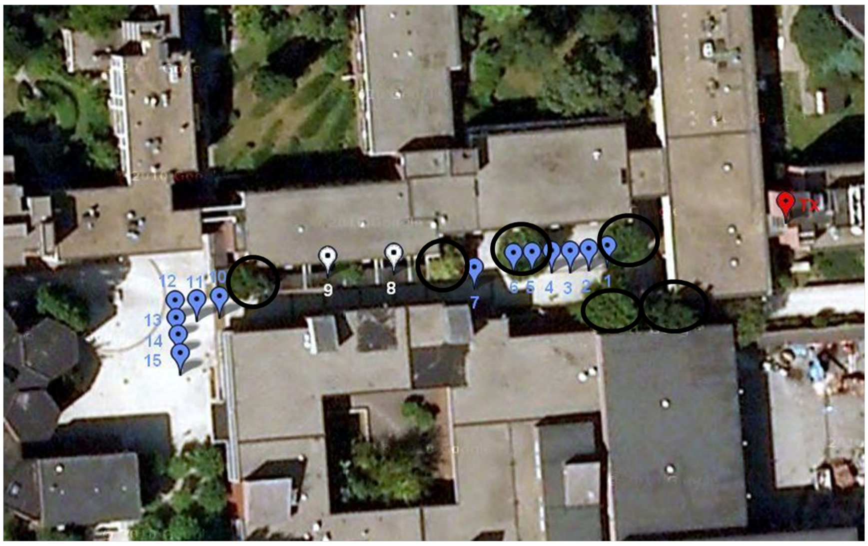

Figure 5.1: Map of the measurement scenario

Table 5.1: Channel sounder setup parameters

Frequency	$3.8GHz$
Bandwidth	$200MHz$
Transmit Power	$23dBm$
Measurable Excess Delay	$10.23\mu s$
Time Resolution	$1.25ns$
Number of Channels	64
Cycles per Measurement	100

floor of a building, facing a pedestrian street. The receiver was moved in fifteen different positions along this street. Positions 1, 13, 14, 15 were in NLOS condition and positions 8 and 9, marked in white in the figure, were in obstructed LOS condition, as the receiver was under a roof that was obstructing the LOS. Measurements were recorded with the Elektrobit MIMO Channel Sounder. Its setup parameters for this campaign are shown in Table 5.1.

In this scenario, building façades are mainly made of brick while roofs are made of concrete. Table 5.2 shows the dielectric parameters of materials utilized in the simulations. The trees, that can be seen in Fig. 5.1, were leafless at the time of the campaign. Their presence is not taken into account in Section 5.2, but their impact is evaluated in Section 5.3.

Table 5.2: Material Properties around $4GHz$

	ϵ_r	$\sigma[S/m]$
Brick	4.4	0.01
Concrete	8.5	0.2

5.2 Diffuse scattering parametrization and validation

A sensitivity test with different values of scattering coefficient S and different width of directive pattern model, set by parameter α_r, has been carried out. Lambertian model is not considered as it has been shown [44] that in outdoor scenarios the Directive one is more suitable. For this test, a maximum of three reflections has been used as well as single bounce scattering. The propagation parameter chosen to determine the best configugation is the received power. In this work, co-polar channels are the ones where antennas at both terminals have the same polarization, whereas cross-polar channels are those with orthogonal polarization at transmitter and receiver sides. Received power is evaluated taking into account co-polar channels only. Fig. 5.2 shows the result of this test in terms of average prediction error for each parameter combination. Considering this outcome, in the following results, a directive model with $S = 0.4$ and $\alpha_r = 2$ has been utilized as it is the one that minimizes the prediction error.

Fig. 5.3 shows the received power comparison between measurements and simulations, when scattering is implemented or not in the simulator. From the graph it is possible to conclude that there is a general improvement when the diffuse component is considered. As a matter of fact, the prediction error drops from 10.1dB to 4.4dB. Excluding positions 14 and 15, that are deep NLOS, the improved tool shows good agreement with measurements. The error, when only the first thirteen positions are taken into account, is 3.2dB.

As previously done for pathloss, Fig. 5.4 is the comparison between simulated and measured values of XPD. In this case the prediction error decreases from 5.5dB, when scattering is not included, to 2.7dB. It has to be noted that, while the tool without scattering seems to accurately predict the XPD in the two last measurement positions, these results are affected by the lack of accuracy of pathloss prediction. In the following part of this section it will be shown that increasing the number of maximum reflections from three to four leads to a complete loss of accuracy in XPD prediction in position 15 if scattering is not included.

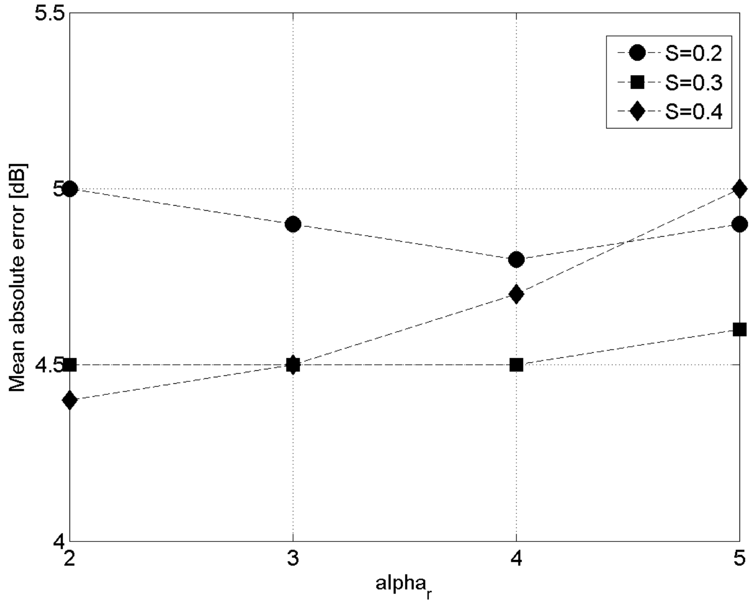

Figure 5.2: Average error in dB for each scattering parameter combination

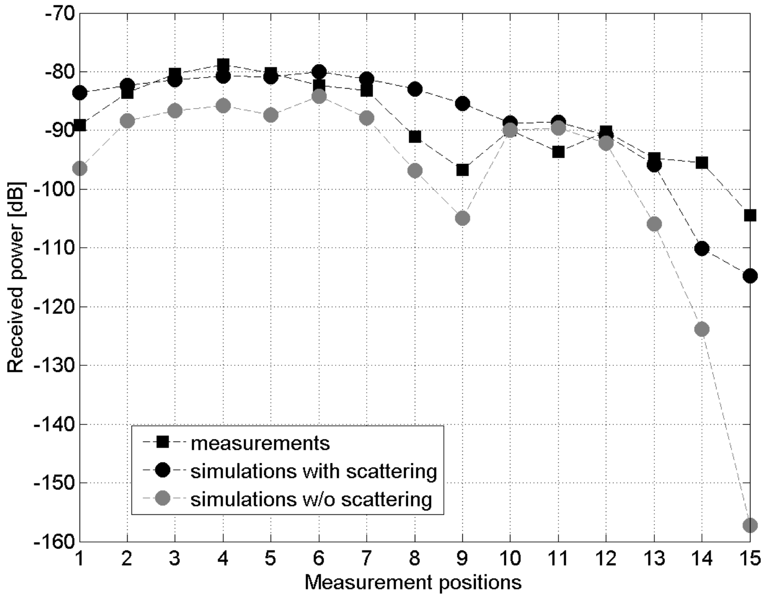

Figure 5.3: Comparison of simulations with measurements for received power

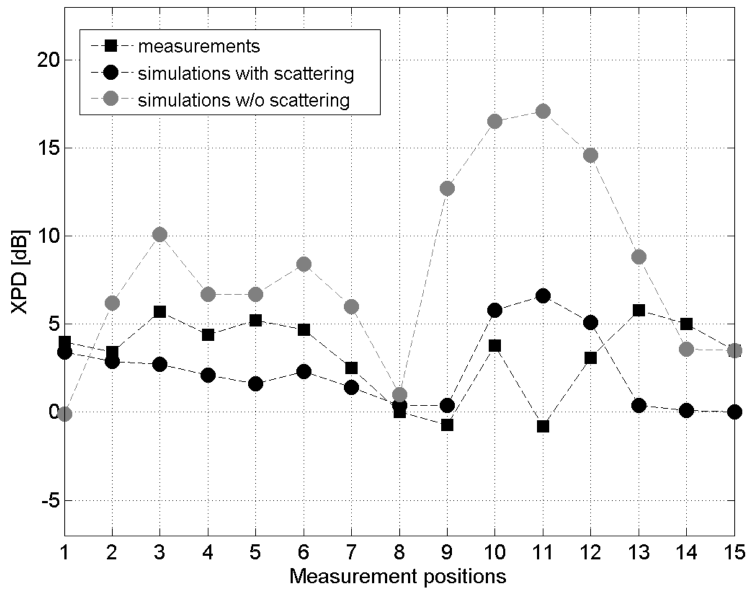

Figure 5.4: Comparison of simulations with measurements for XPD

	Mean Error	Standard Deviation
Received Power [dB]	4.4	4.6
XPD [dB]	2.7	2.0

Table 5.3: Summary of the mean prediction errors for received power and XPD

Table 5.3 presents a summary of the errors standard deviations.

Fig. 5.5 shows the ratio between simulated diffuse power and simulated total received power, both for co-polar and cross-polar channels. It can be noted that, in the cross-polar channels, the power is for the greatest part composed by scattering, with an average ratio of 83%. In the co-polar channels the average ratio is 55%.

Some considerations can be made concerning the results presented. For example, taking into account that, in co-polar channels, it has been found that normally the percentage of scattering power in outdoor scenarios varies from 20% to 80% [97], the results presented in Fig. 5.5 shows that in NLOS conditions this percentage is generally exceeded. By contrast, in positions from 10 to 12, the level is lower than the expected one. In the same three positions, simulated XPD is higher than the measured one. This two results can be seen as a symptom of over-

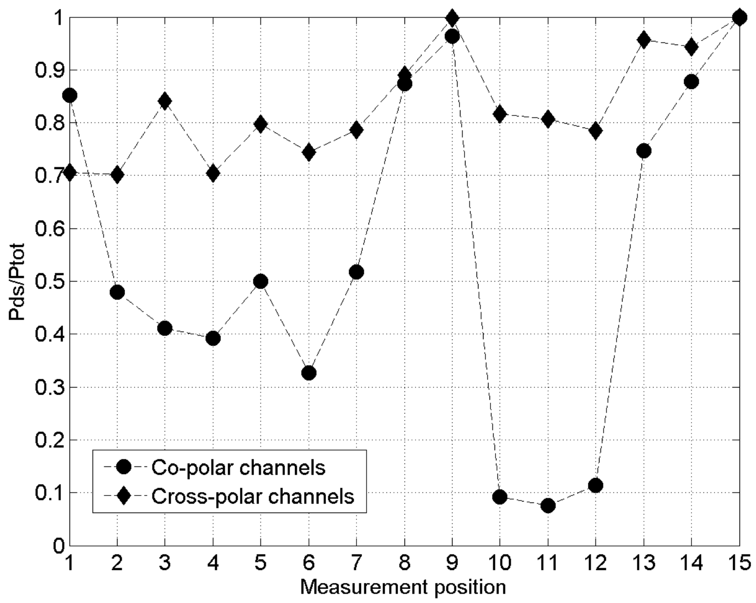

Figure 5.5: Ratio between diffuse power and total received power for simulations

estimation of the coherent component of the signal. This might be due to the fact that the presence of trees was not taken into account in the simulations. Something can also be said about NLOS positions from 13 to 15, where the XPD prediction underestimates the measurements. Considering that in positions 14 and 15 pathloss is also significantly underestimated, it could mean that there is some coherent path that is not estimated by the tool. On the other hand, in position 13 pathloss prediction is good. So an alternative conclusion could be that there is need of a better modeling of polarization behavior of scattering, which is the most significant part of the power received in NLOS conditions.

Fig. 5.6 shows the comparison between simulated, with and without scattering, and measured delay spread. While the results show a slight improvement after the implementation of scattering, there is a significant underestimation of the measurements.

The number of maximum reflections that a single ray can experience has been increased from three to four. This does not affect the prediction error of the simulations with scattering for pathloss and XPD. On the other hand, it affects prediction error in position 15 in the simulations without scattering. It decreases the error for pathloss but it increases significantly the one for XPD, confirming the assumption that the good

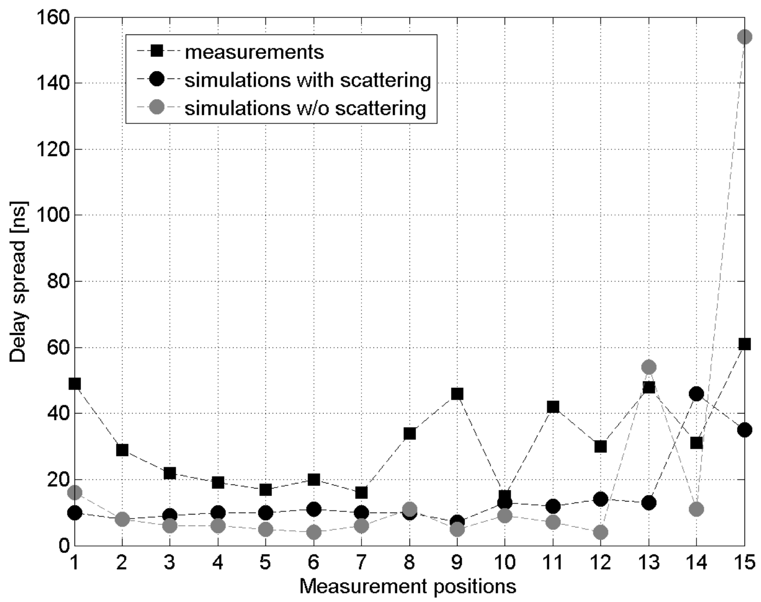

Figure 5.6: Comparison of simulations with measurements for delay spread

match with the measurements was not trustable in that case. The average prediction error, in the simulations without scattering, becomes 8.6dB for pathloss and 6.4dB for XPD. Fig. 5.7 shows that delay spread prediction, instead, is improved, even if just in some positions.

Finally, scattering interaction followed or preceded by a single reflection as been added to simulations. Considering also four maximum reflections, the prediction error for pathloss decreases from 4.4dB to 3.5dB. This is due to an significant improvement in prediction for the last three positions (deep NLOS). Concerning XPD, the prediction error decreases from 2.8dB to 2.6dB. Fig. 5.8 shows that in this case delay spread prediction is generally improved, but the underestimation is always present.

Concluding this section, the results presented show that diffuse scattering is important to obtain accuracy of received power and XPD prediction in outdoor scenario. The improvement is significant and simulations show good agreement with measurements. Considering delay spread, diffuse scattering improves the accuracy of prediction marginally. A more perceptible improvement is noted if the number of interactions allowed for each ray is increased, but the cost in terms of computation time is significantly increased. In any case, there is a general underesti-

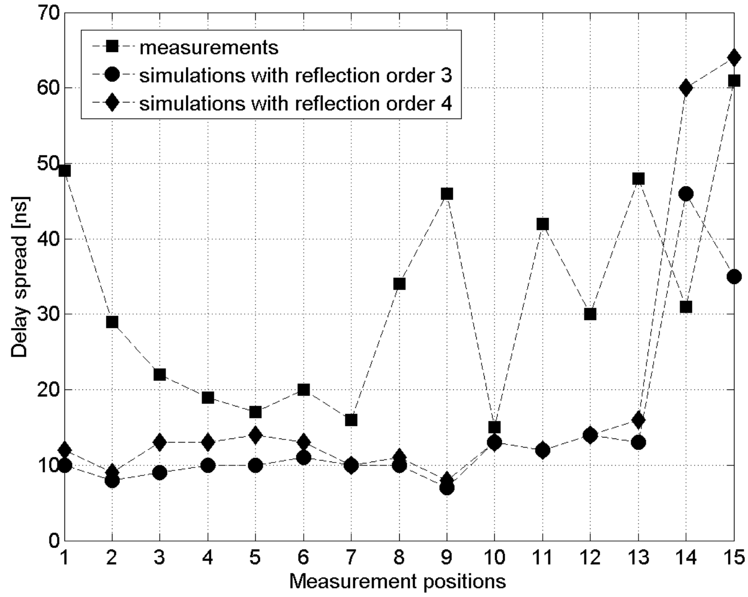

Figure 5.7: Comparison of delay spread results for simulations with scattering with different levels of maximum possible reflections

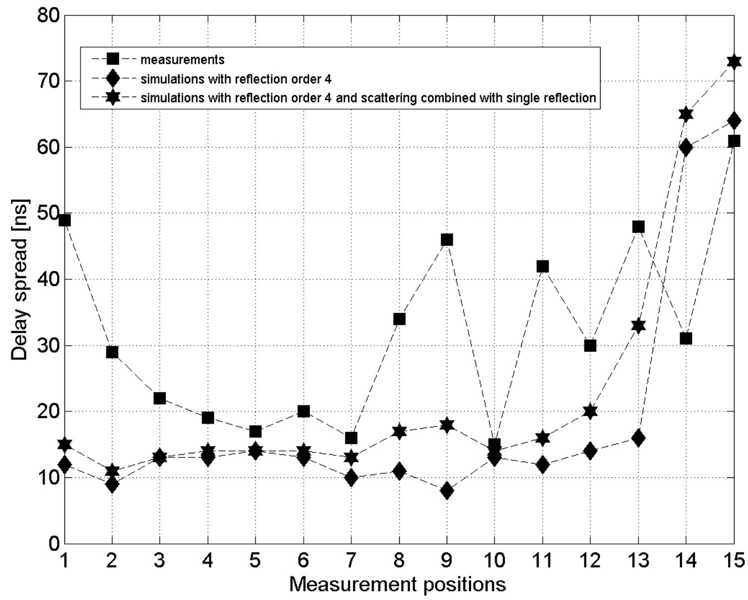

Figure 5.8: Delay spread results for simulations with four maximum possible reflections and scattering with a reflection before or after

Table 5.4: Summary of specific attenuation coefficients by single tree with no foliage

Reference	Atten. [dB/m]	Freq. [GHz]
de Jong and Herben [45]	0.8	1.9
Horak and Pechac [64]	0.6	2

mation of measured delay spreads.

5.3 Parametrization and validation of tree scattering model

5.3.1 Setup parameters for tree modeling

As presented in Section 2.5.1, several empirical models are available to evaluate the excess attenuation by vegetation. Here, the Weissberger model for $d < 14$m is used. At 3.8GHz, the excess attenuation evaluated with this model is $L = 0.66$dB/m. While Weissberger model considers trees with foliage, leafless ones are of interest in this work. In [61] the attenuation coefficient [dB/m] by trees out of leaves is found to be $\approx 20\%$ smaller than the one with foliage, so the excess attenuation has been reduced to $L = 0.55$dB/m.

Weissberger model is generally used for long penetration distances and it might not be suitable for single tree attenuation. For this reason specific attenuation by single trees, presented in Tab. 2.1, have also been used. Tab. 5.4 summarizes the values in case of leafless trees. As these results are evaluated at a single frequency, different from the one it has been used for the measurements, Eq. 2.58 and 2.59 have been used to scale the attenuation coefficient to 3.8GHz and for both formulas the result is an excess attenuation of 1dB/m. The specific attenuation coefficients proposed in [58] and showed in Eq. 2.60 and 2.61 are also utilized in this context.

Six trees, the ones marked by a black circle in Fig.5.1, have been modeled for RT simulations. To build a digital version of a tree, a 3D-fractal tree generator [101] has been used. Fig. 5.9 shows the visualization of an example of tree generated by this software. The position of the center of each branch and its orientation in space are determined directly by the output of this program. Four level of branches were created above the trunk and each branch, trunk included, generates four branches at the following level. The trunk is generated with an height of 3.5m and a diameter of 0.7m. When a mother branch of diameter d_1 produces n daughter branches all of diameter d_2, the two parameters are

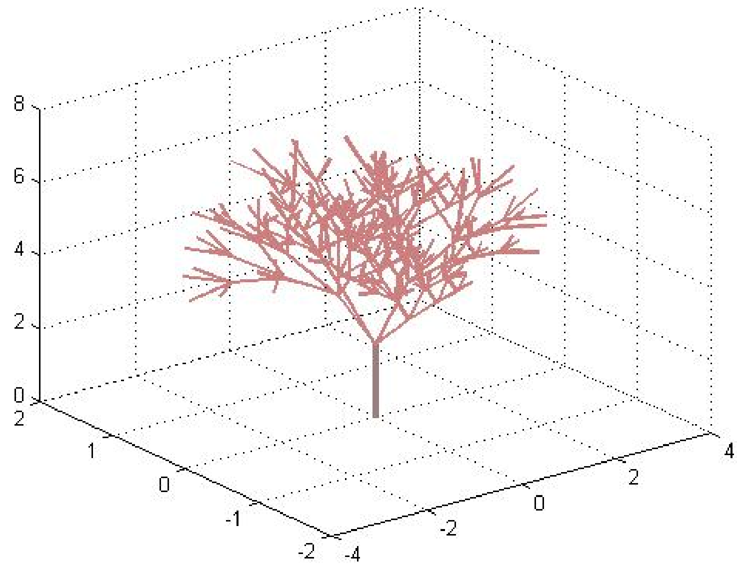

Figure 5.9: Visualization of an example of fractal tree

related by the equation $d_1^2 = n \cdot d_2^2$ [102]. The length reduction factor between mother and daughter branches has been fixed to 0.7 at each level. Each tree is described by a total of 84 branches.

5.3.2 Simulation results

The different scattering reduction laws are tested and the results are presented for the Weissberger model, i.e. a specific attenuation of $0.55dB/m$, in Table 5.10, for the single tree model, i.e. a specific attenuation of 1dB/m, in Table 5.11 and for the specific attenuation cofficients proposed in [58] in Table 5.12. In all cases the comparison with measurements is evaluated by means of RMSE of the received power.

From these results it is possible to conclude that the difference between the reduction law implementations and specific attenuations is not significant, as in all cases the RMSE is $\approx$ 4dB. The exponential law seems to provide slightly worst results. Anyway the improvement with respect to the case when scattering by tree branches in not implemented is evident, as it is also if the new results are compared with the one previosly presented when the presence of trees was not taken into account.

Fig. 5.13 shows the comparison in this situation between simulations,

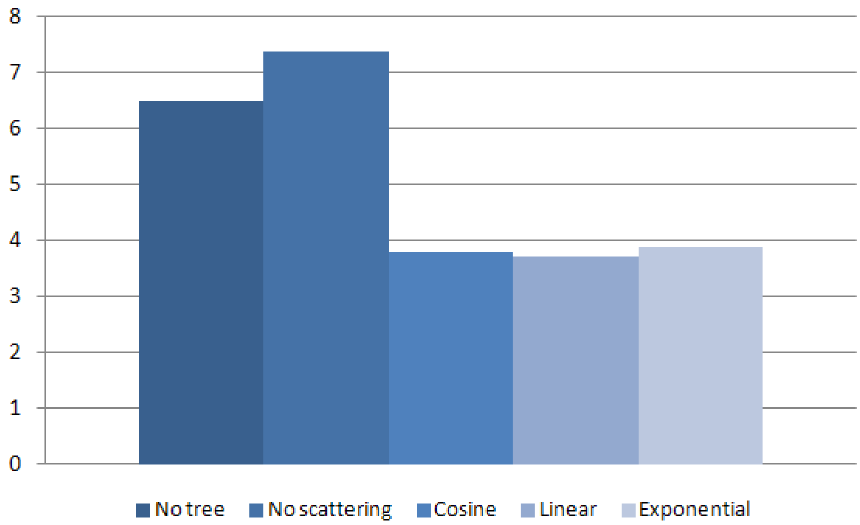

Figure 5.10: Comparison of absolute mean errors when an excess attenuation of 0.55dB/m is considered

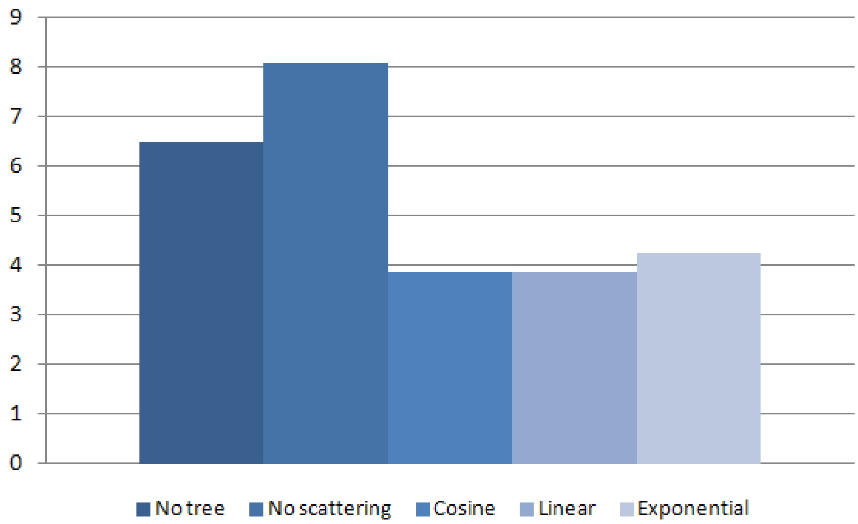

Figure 5.11: Comparison of absolute mean errors when an excess attenuation of 1dB/m is considered

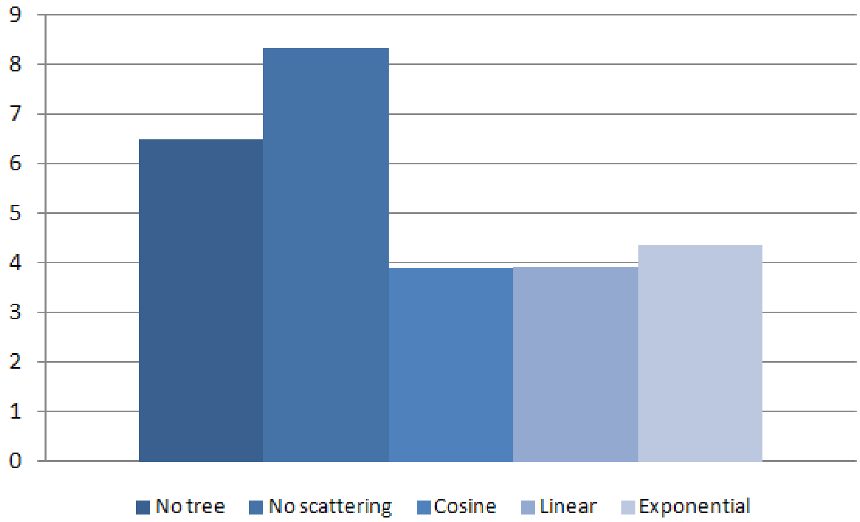

Figure 5.12: Comparison of absolute mean errors when the polarization dependent excess attenuation is considered

with and without contribution by trees, and measurements. The linear reduction law with a specific attenuation of 0.55dB/m has been chosen for trees. As it can be seen, the improvement is particularly important in the last two measurement positions where the accuracy is obtained only when scattering is included. The graph shows also that after the implementation of tree contributions, the accuracy is good everywhere except positions 8 and 9. If those two positions are excluded the RMSE decreases to 2.1dB.

Fig. 5.14 shows, instead, the comparison between simulations with scattering and attenuation by trees and simulations with only attenuation. It is evident that, in such environments, attenuation by vegetation is not sufficient to model tree contribution and that scattering plays a decisive role to correctly evaluate the received power.

5.4 Conclusion

This chapter presented measurements and simulations in an outdoor campus scenario.

In the first part the diffuse scattering by building walls model is validated. The sensitivity of pathloss has been tested with respect to diffuse scattering parameters S and α_r. Results of simulations for pathloss, XDP and delay spread are presented and compared with measurements. These show that diffuse scattering is an important feature to achieve

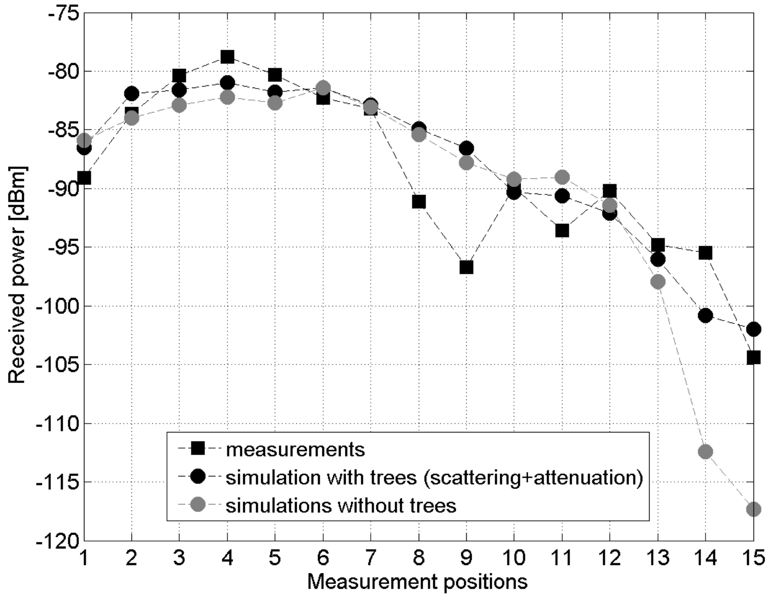

Figure 5.13: Comparison of received power with and without the contribution by trees (scattering and attenuation)

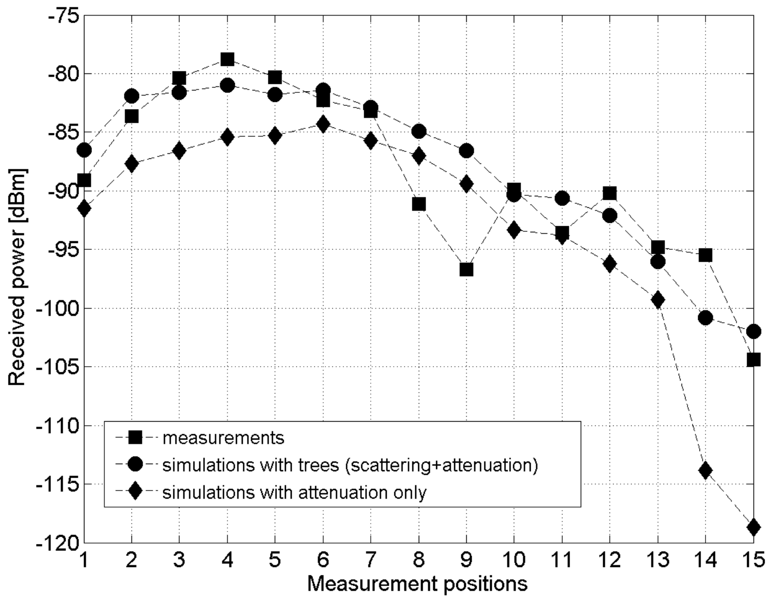

Figure 5.14: Comparison of received power with and without the scattering contribution

good accuracy for pathloss and XPD prediction even in outdoor scenario. The improvement is significant and the simulations generally show good agreement with measuremtnts. Considering delay spread, diffuse scattering improves the accuracy of prediction marginally. A better improvement is noted if the order of interactions allowed is increased, but this costs significantly in terms of computation time. In any case, there is a general underestimation of measured delay spreads.

The proposed ray-based method to evaluate scattering by vegetation is then implemented in the RT tool to take into account the presence of trees out of foliage in the measurement scenario. In the first part they were not modeled in the input database. Attenuation by vegetation is modeled with specific attenuation coefficient, L[dB/m], and different values of L found in literature are tested. Measurements and simulations, when tree contributions are taken into account, are compared in the same campus scenario. The results show that, in such environments, attenuation by vegetation is not sufficient to model tree contributions and scattering by tree branches plays a decisive role to correctly evaluate the received power. As a matter of fact, when scattering by tree branches is implemented in addition to the attenuation, the prediction error is significantly improved.

6

A polarized diffuse scattering model

In chapter 5, it has been shown that diffuse scattering represents an important part of the received power in an outdoor scenario. Moreover, diffuse scattering plays an important role in determining the polarization behavior of the channel, whose importance is increasing as MIMO schemes that exploit polarization diversity are proposed to improve radio channel performance in mobile radio systems. For this reason, in this section a polarization model for diffuse contributions scattered off building walls is proposed, parameterized with ad-hoc measurements and validated in classical outdoor environments.

The environment for the ad-hoc measurement campaigns consists of single building scenarios. To infer scattering properties it is necessary to isolate it from coherent components of the channel response, i.e. LOS, reflections and diffractions. This become harder and harder with the increase of complexity of the channel scenario. In a single building environment the coherent components are few and easy to determine geometrically. The disadvantage is that it may be diffcult to find an isolate buildings that can be considered representative of an urban scenario.

The diffuse component is obtained by subtracting from the measurements the coherent one, that is predicted by jointly utilizing RT and SAGE algorithm. Once the incoherent part is extracted, its polarization behavior is studied and the results are used to parameterize the polarization model.

Table 6.1: Channel sounding setup parameters for diffuse scattering polarization model measurement campaigns

Frequency	3.8 GHz
Bandwidth	200 MHz
Transmit Power	23 dBm
Code Length	5.11 μs
Cycles per Measurement	100

6.1 Derivation and parameterization of the polarization model

6.1.1 Ad-hoc measurement campaigns

The derivation and parameterization of the polarization model for diffuse scattering [103] relies on two experimental campaigns focusing on buildings with different characteristics:

- the first campaign was carried out near the city of Gembloux (Belgium) along the façade of a rural countryside building (see Fig. 6.1), featuring an almost regular brick surface,
- the second campaign took place in Louvain-la-Neuve (Belgium), in front of an isolated office building (see Fig. 6.2), characterized by a large glass wall sustained by a metallic frame.

In both scenarios, grass was present on the ground facing the building, thus attenuating the reflections off the ground. Furthermore, the environment was kept static during the sounding.

Measurements were performed with the Elektrobit MIMO Channel Sounder. Its setup parameters for both the campaigns are shown in Table 6.1. At both transmit (Tx) and receive (Rx) sides, a linear array of 4 dual-polarized ($+45°$ and $-45°$ slanted polarization) patch antennas was used, in such a configuration that the antennas were facing the wall under test. 64 channels, each one corresponding to a couple of Tx/Rx antenna elements with a given polarization-state couple, were therefore measured. The Rx terminal was kept in a fixed position, whereas the Tx array was moved in 3 and 5 locations for the rural (see Fig. 6.3) and office building (see Fig. 6.4) scenarios respectively.

6.1.2 Extraction of the diffuse component

The first step consists ofremoving from the measurements the contributions not coming from the wall under examination, such as the LOS

Figure 6.1: Isolated rural building

Figure 6.2: Isolated office building

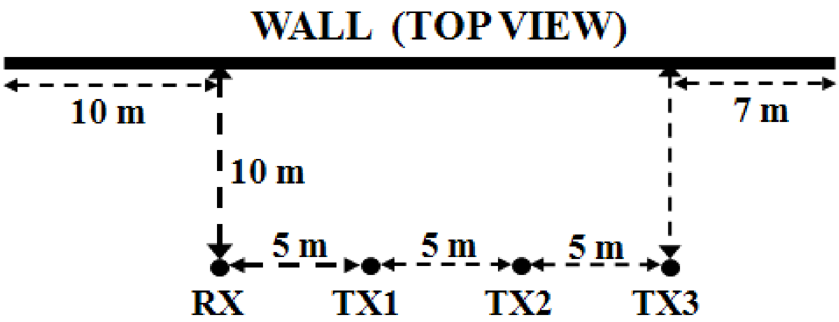

Figure 6.3: Map of the rural scenario measurements for diffuse scattering polarization model

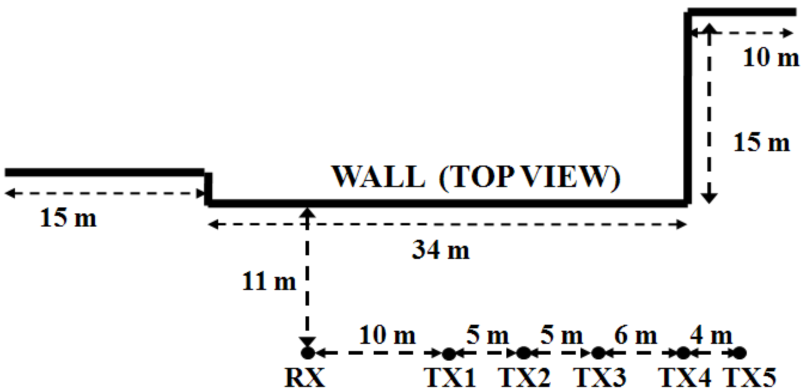

Figure 6.4: Map of the office scenario measurements for diffuse scattering polarization model

component as well as all contributions caused by further objects. A time window can be easily determined knowing the dimension of the wall and its relative position with respect to the transmit and receive antennas. The noise is also removed with a threshold method, i.e. all the contributions falling below the threshold, determined considering a portion of impulse response consisting of only noise, are eliminated. This is advisable to compare the measurements with RT simulations, where noise is not present.

In order to isolate the diffuse component, it is necessary to identify the coherent (or specular) component, so that it can be subtracted from the measured channels. Despite the choice of a single building scenario to simplify the identification of coherent components, it is not possible to determine with sufficient accuracy the power level of these components by ray-tracing only, mostly because of uncertainties regarding the material characteristics (complex electric permeability) of the wall under test. Thus, the RT tool is calibrated using measurements post-processed with a high resolution estimation algorithm based on the SAGE method (see Section 3.3).

From this estimation, the delay and angle values are used to identify the single-reflected ray among all SAGE extracted rays, considering that they can be analytically determined by geometric considerations for each position with the help of RT prediction. Once the single-reflected ray is identified, its polarization matrix Γ

$$\Gamma = \begin{bmatrix} \gamma_{\theta\theta} & \gamma_{\theta\phi} \\ \gamma_{\phi\theta} & \gamma_{\phi\phi} \end{bmatrix} \tag{6.1}$$

is used to calibrate the RT model through the iterative procedure depicted in Fig. 6.5.

Antenna re-embedding, which is also part of the calibration procedure, is performed by re-introducing the antenna contribution into the polarization matrix in the following manner:

$$\begin{aligned} s^{(ij)} = \begin{bmatrix} C^{(j)}_{Rx\theta}\left(\theta_A, \phi_A\right) & C^{(j)}_{Rx\phi}\left(\theta_A, \phi_A\right) \end{bmatrix} \cdot \\ \cdot \begin{bmatrix} \gamma_{\theta\theta} & \gamma_{\theta\phi} \\ \gamma_{\phi\theta} & \gamma_{\phi\phi} \end{bmatrix} \cdot \begin{bmatrix} C^{(i)}_{Tx\theta}\left(\theta_D, \phi_D\right) \\ C^{(i)}_{Tx\phi}\left(\theta_D, \phi_D\right) \end{bmatrix} \end{aligned} \tag{6.2}$$

where the super-scripts (i) and (j) refer to the i^{th} Rx antenna element and j^{th} Tx antenna element, respectively, C_θ and C_ϕ are the radiation pattern θ and ϕ components of the i^{th} receive or j^{th} transmit antennas, and finally (θ_D, ϕ_D) and (θ_A, ϕ_A) are the direction of departure and

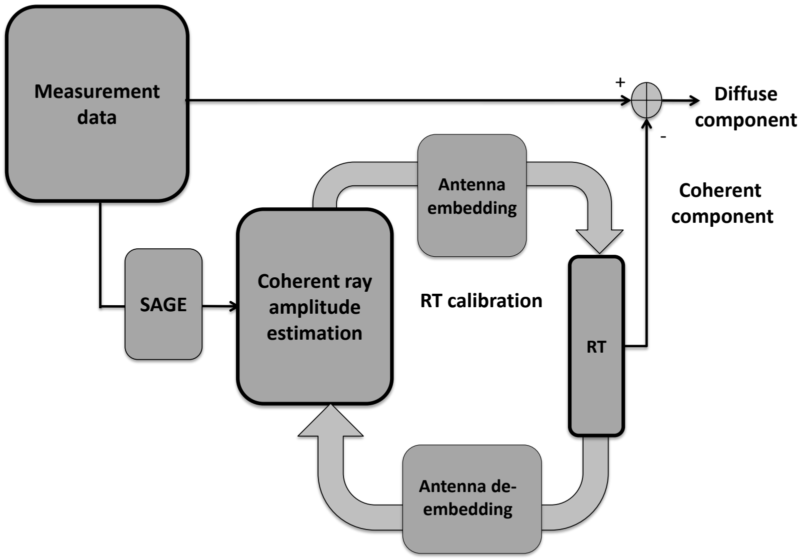

Figure 6.5: Flow chart of data post-processing procedure for RT calibration

arrival, respectively. Considering that the two terminals are at the same height, $\theta_A = \theta_D = \pi/2$.

The final step of the procedure is to subtract the power profile obtained from the calibrated RT output from the total measured power profile. Since the RT output corresponds to an infinite bandwidth, it is first filtered according to the measurement bandwidth of the system, using the channel sounder calibration response as filter.

6.1.3 Analysis of the diffuse extracted component

In Figs. 6.6 and 6.7, the power delay profiles of the coherent, diffuse and overall measured components, taking the office building scenario as example, are presented.

A first indicator to investigate the diffuse component is the ratio between the diffuse power and the total backscattered power. Table 6.2 and Table 6.3 show this ratio for the rural and the office building scenario, respectively. From these results, it can be observed that, even in a simple single building scenario, scattering represents an important part of the total power backscattered from a wall. As previously hypothesized, its relevance increases with the increase of building complexity, i.e.

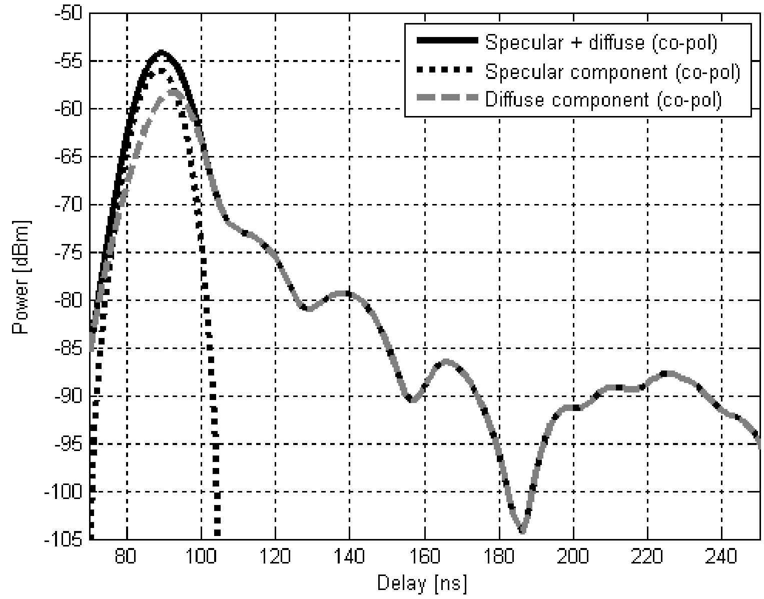

Figure 6.6: Office scenario measurement position 2: specular component, diffuse component and total power on co-pol channels

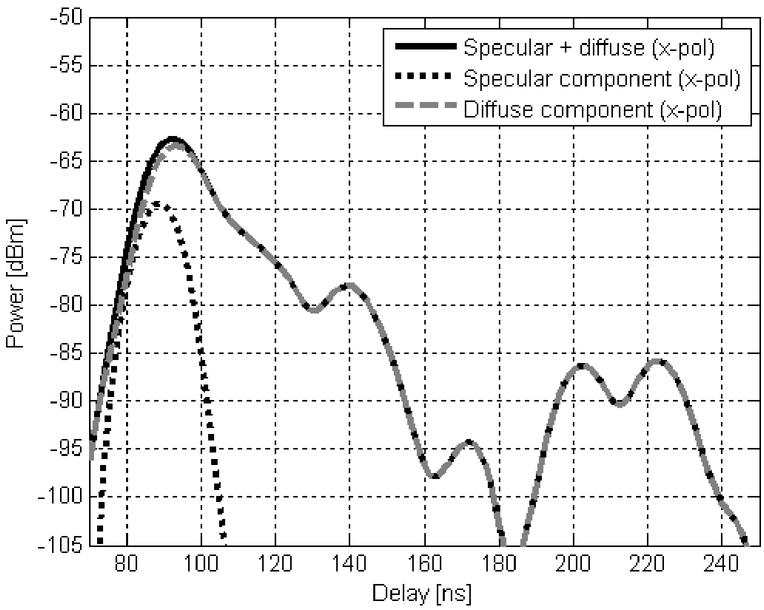

Figure 6.7: Office scenario measurement position 2: specular component, diffuse component and total power on x-pol channels

Table 6.2: Ratio between diffuse power and total backscattered power retrieved from measurements in rural scenario

P_d/P_{tot}	Co-polar channels	Cross-polar channels	All channels
Tx pos. 1	0.27	0.44	0.28
Tx pos. 2	0.30	0.48	0.31
Tx pos. 3	0.27	0.32	0.28
All pos.	0.28	0.41	0.29

Table 6.3: Ratio between diffuse power and total backscattered power retrieved from measurements in office scenario

P_d/P_{tot}	Co-polar channels	Cross-polar channels	All channels
Tx pos. 1	0.47	0.75	0.61
Tx pos. 2	0.43	0.86	0.50
Tx pos. 3	0.45	0.47	0.45
Tx pos. 4	0.36	0.77	0.42
Tx pos. 5	0.52	0.96	0.60
All pos.	0.45	0.69	0.52

$\approx 30\%$ for the rural building and $\approx 50\%$ of the total power for the office building, but it also depends on polarization, e.g. in the office building, the diffuse power can reach 90% of the cross-polar power.

The other metric used in this work to analyze the post-processed data is the XPD. Table 6.4 shows the results for the rural building and Table 6.5 for the office building scenarios. It is important to note that the coherent part of the power generally overestimates the measured XPD, i.e. the diffuse part plays a decisive role also in determining the total XPD. This is particularly evident, once again, in the office building case.

Table 6.4: XPD values for rural building scenario

XPD (dB)	Coherent part (RT)	Diffuse part	Full Measurements
Tx pos. 1	17.7	14.5	15.3
Tx pos. 2	13.2	9.6	11.7
Tx pos. 3	5.6	4.6	5.3
All pos.	12.2	9.6	10.8

Table 6.5: XPD values for office building scenario

XPD (dB)	Coherent part (RT)	Diffuse part	Full Measurements
Tx pos. 1	4.6	-1.0	1.1
Tx pos. 2	13.3	4.2	7.2
Tx pos. 3	5.1	4.7	5.0
Tx pos. 4	11.2	3.5	6.8
Tx pos. 5	17.9	3.9	6.7
All pos.	10.4	3.1	5.4

6.1.4 Description of the polarization model

The diffuse scattering field polarization is described by two states, co-polar and cross-polar, and a parameter K_{xpol}. The co-polar component is the one that the field would have if scattering interaction did not introduce any depolarization. The parameter K_{xpol} sets the amount of power transferred to the cross-polar component, that is orthogonal to the co-polar one.

With an arbitrary choice, the co-polar component is polarized like specular reflection would be. This choice has been suggested by the preliminary analysis of the diffuse component extracted from the ad-hoc measurements presented in the previous section, where a reflection-like behavior has been noticed. According to this choice, $K_{xpol} = 0$ produces a maximum of the cross-polar discrimination (XPD). When K_{xpol} is increased, XPD decreases accordingly.

If E_s is the amplitude of the diffuse scattering field, as presented in Section 2.4.2, the co-polar scattering component can be expressed in the following way:

$$\mathbf{E}_{co} = E_s \hat{\imath}_{inc} \overline{\mathbf{R}}_u \tag{6.3}$$

where $\hat{\imath}_{inc}$ is the polarization unit vector of the incident field and $\overline{\mathbf{R}}_u$ is a unitary dyadic reflection coefficient that can be written as:

$$\overline{\mathbf{R}}_u = e^{j\psi_h} \hat{\imath}_\phi^i \hat{\imath}_\phi^d + e^{j\psi_s} \hat{\imath}_\theta^i \hat{\imath}_\theta^d \tag{6.4}$$

where $\hat{\imath}_\phi$ and $\hat{\imath}_\theta$ are the phi and theta components, that can be referred to the incident (i) or diffusely scattered field (d), and ψ_h and ψ_s are the phases of the hard and soft reflection coefficients [18] at the scattering point. As an example:

$$e^{j\psi_h} = \frac{R_h}{|R_h|} \tag{6.5}$$

This formulates the fact that the polarization behavior of the co-polar component is analogous to the one of the reflection. Fig. 6.8 shows the

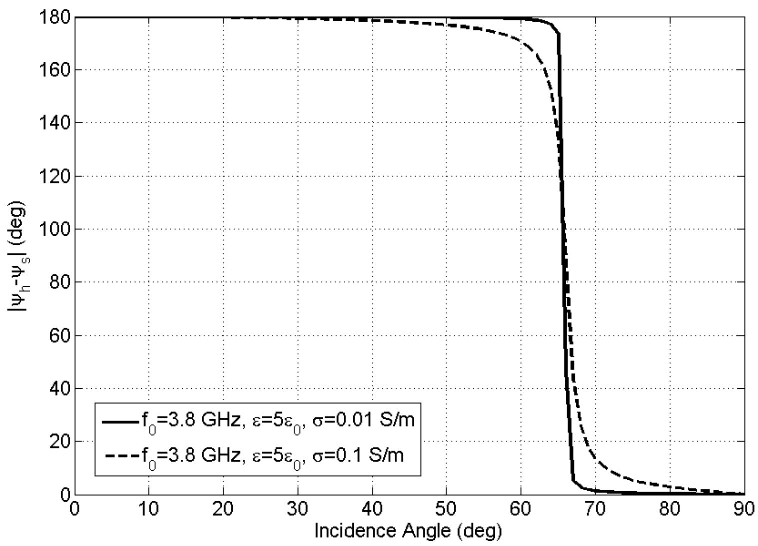

Figure 6.8: Phase difference between hard and soft reflection coefficients

phase difference between the hard and soft reflection coefficients that is assumed to be valid also for the co-polar scattering component.

If the depolarization coefficient K_{xpol} is introduced, the diffuse scattering field can be written as:

$$\mathbf{E}_s = \sqrt{1 - K_{xpol}}\, E_s\, e^{j\chi_{co}} \hat{i}_{co} + \sqrt{K_{xpol}}\, E_s\, e^{j\chi_{xp}} \hat{i}_{xp} \tag{6.6}$$

where $\hat{i}_{co} = \hat{i}_{inc}\overline{\mathbf{R}}_u$ is a polarization unit vector representing the co-polar component, and $\hat{i}_{xp}$ is the unit vector orthogonal to $\hat{i}_{co}$, so that $\hat{i}_{co} \cdot \hat{i}^*_{xp} = 0$.

6.1.5 Parameterization of the polarization model

The polarization model for diffuse scattering is parameterized using the data extracted from post-processed measurements as presented in the previous section. The scattering parameters under test are S and α_r and K_{xpol}.

Rural Building Scenario

For the rural scenario, $S = 0.3$ and $\alpha_r = 3$ are chosen as starting values. Since α_r has a negligible impact on the cited indicators in this case, its optimization is not presented among the following results. Fig. 6.9

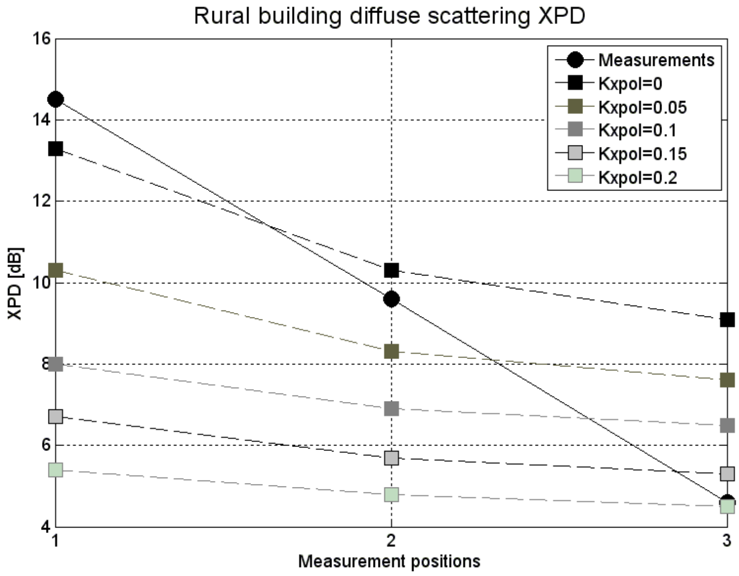

Figure 6.9: Diffuse scattering XPD in rural scenario for different values of K_{xpol}

presents the comparison of measured and RT-predicted diffuse scattering XPD values for different values of K_{xpol} parameter. It is difficult to find an optimal value because the measured and the simulated curves have different shapes. Still, it is possible to notice that the average value of K_{xpol} required for RT simulation to match measurements at best is very low.

Considering the diffuse power ratio, P_d/P_{tot}, and comparing the results for different values of S, as shown in Fig. 6.10, it is possible to infer that the optimal value of S is approximately 0.45, in agreement with what it has been found in other works [44].

Office Building Scenario

Also in the office building scenario, $S = 0.3$ and $\alpha_r = 3$ are chosen as starting values for the scattering parameters. Fig. 6.11 shows the diffuse scattering XPD in this scenario for different values of K_{xpol} parameter. With the exception of position 1, where the measured value diverges significantly, simulations with $K_{xpol} = 0.2$ seem to accurately predict the extracted values. On the other hand, the choice of K_{xpol} does not influence significantly the predicted value of diffuse power ratio, with maximum differences of 3% with respect to the measurements for different values of K_{xpol} tested. Therefore, $K_{xpol} = 0.2$ can be considered the

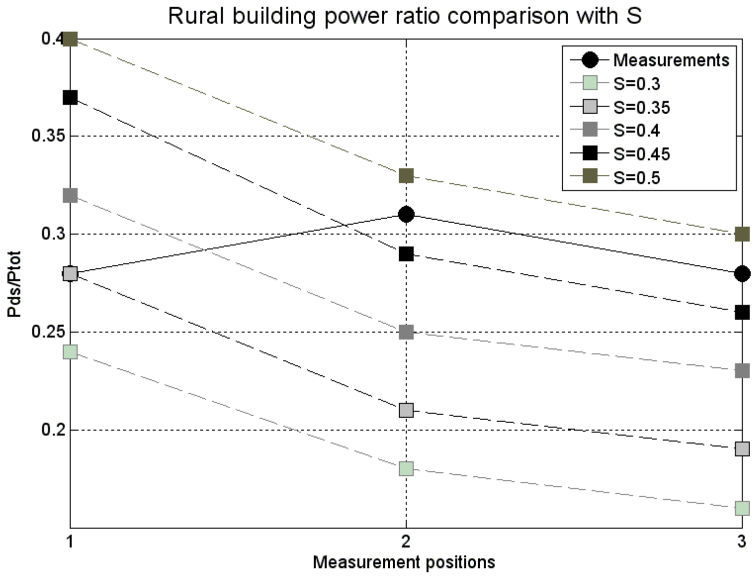

Figure 6.10: Ratio between diffuse power and total backscattered power in rural scenario for different scattering parameters

optimum value and will be adopted in the following simulations. Note that his value is much higher than in the rural building case. This is due to the increased complexity of the building under examination, i.e. the extensive metal grid integrated for sustain purposes into the glass wall.

Fig. 6.12 shows the ratio between diffuse power and total backscattered power in office scenario for different values of S with $\alpha_r = 3$. Excluding position 5, where the measured value diverges significantly from the other positions, $S = 0.6$ yields the lower discrepancy. Comparing this figure with what found in the rural case, it is confirmed that the more complex building generates a higher overall amount of diffuse scattered power.

At this stage, keeping fixed the optimal value of S and K_{xpol}, the parameter α_r can be optimized as illustrated in Fig. 6.13. It is evident that its influence on XPD is marginal. In a similar way, α_r does not influence significantly P_d/P_{tot}, as differences are less than 2% with respect to the measurements for the considered α_r range. However, since $\alpha_r = 2$ yields slightly better results, it is chosen as the final value.

Finally, a finer tuning of K_{xpol} versus XPD, with $S = 0.6$ and $\alpha_r = 2$, is shown in Fig. 6.14, while Fig. 6.15 presents the subsequent mean prediction error (excluding position 1). It can be concluded that $K_{xpol} = 0.2$ minimizes the mean error on XPD.

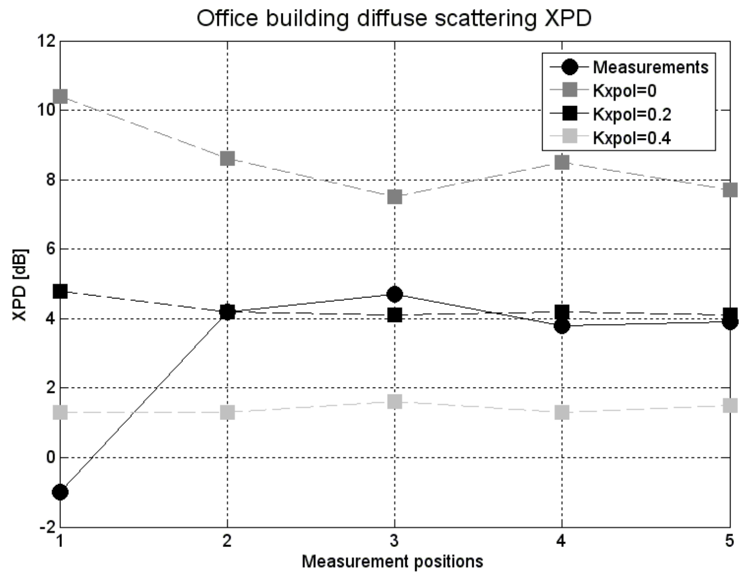

Figure 6.11: Diffuse scattering XPD in office scenario for different values of K_{xpol}

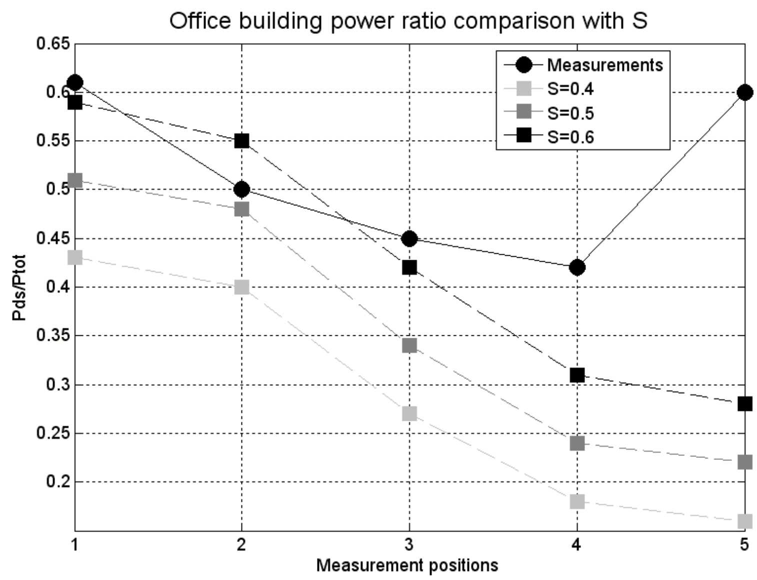

Figure 6.12: Ratio between diffuse power and total backscattered power in office scenario for different scattering parameters

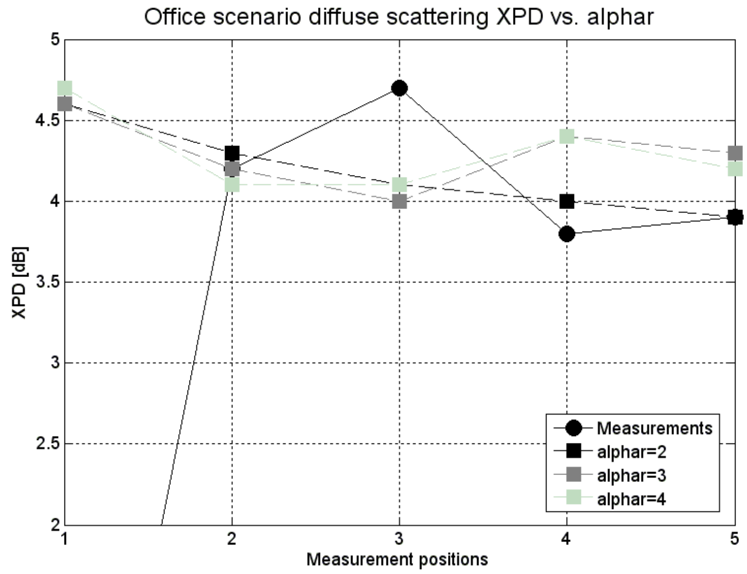

Figure 6.13: Diffuse scattering XPD in office scenario for different scattering lobe width

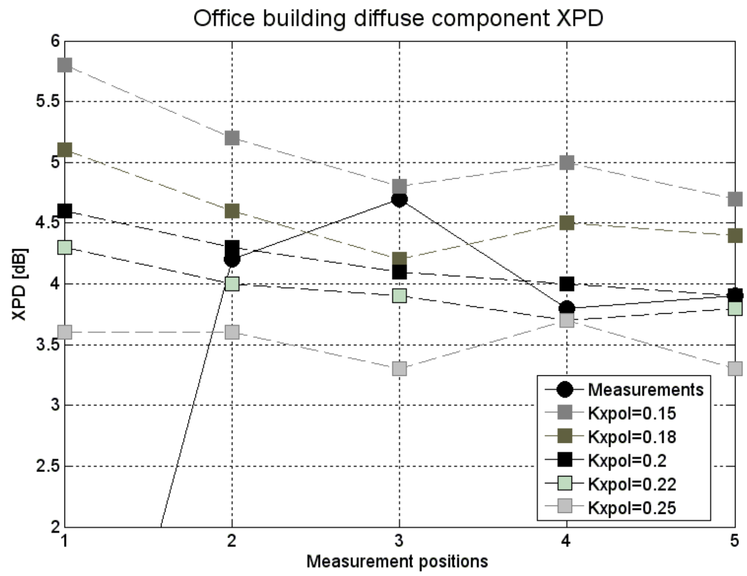

Figure 6.14: Finer tuning of K_{xpol} parameter versus diffuse scattering XPD in office scenario

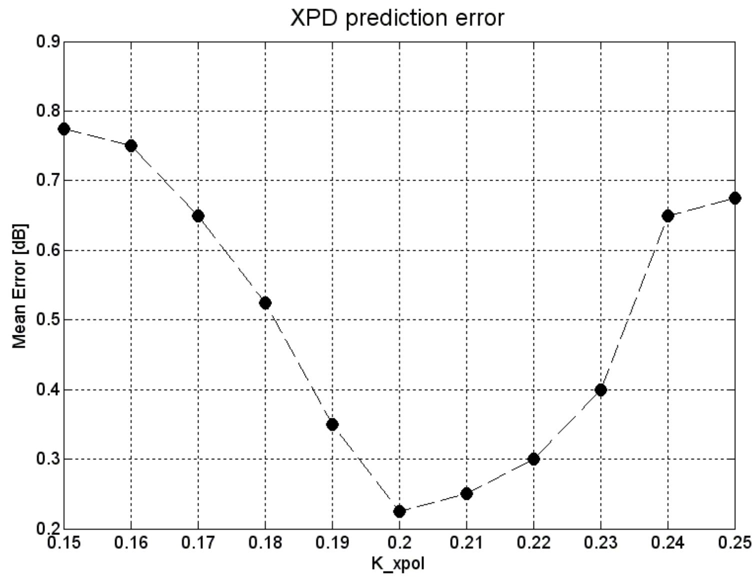

Figure 6.15: XPD mean prediction error, excluding position 1, for different values of K_{xpol}

6.2 Validation of the polarization model

This section, based on the work presented in [104], focuses on the validation of the polarization model for rays scattered off building walls. Two measurement campaigns are exploited with this purpose. The first one is in a street canyon scenario and the second one is the one presented in Section 5.1. It is worth to mention that the validation of the model is done with different measurements carried out in different scenarios with respect to the parameterization part.

6.2.1 Measurements

Both measurement campaigns were recorded with the Elektrobit MIMO Channel Sounder. Its setup parameters are similar to the ones presented for other measurement campaigns and as reminder they are shown in Table 6.6. As usual, linear array of 4 dual-polarized slanted polarization ($+45°$ and $-45°$) patch antennas was employed both at transmitter (Tx) and receiver (Rx) side, giving a total of 64 channels measured.

The first measurement campaign was carried out in a street canyon scenario located in Louvain-la-Neuve, Belgium. The street was chosen because it is pedestrian, thus disturbance from traffic was not a problem. Considering that a static environment was required for the

Table 6.6: Channel sounder setup parameters

Frequency	3.8 GHz
Bandwidth	200 MHz
Transmit Power	23 dBm
Code Length	10.23 μs
Cycles per Measurement	100
Cycles Rate	9.8 Hz
Number of channels	64

measurements, they were conducted on a Sunday morning to avoid the influence of walking-by people.

Fig.6.16 shows the measurement scenario. For practical reasons, Tx unit was moved in different positions while Rx was fixed. Two series of measurements were taken. Considering that the goal was to study the diffuse contributions scattered off building walls, in the first of the two series both antennas were facing towards the same wall, while in the second they were both facing the direction of movement of the Tx unit (towards the white arrow in the figure). This second configuration was decided to try to analyze backscattering from the bottom of the street canyon. In each of the two series, measurements in ten positions were recorded. In the first position the distance between the two units was $10m$. Following positions were at a distance of $5m$ from each other. The height of the antennas was $1.5m$ from the ground. The measurements for the second position in the first series, with antennas facing the wall, were unusable, thus no results are presented in that case.

The second measurement campaign, in a campus scenario, is the one presented in Section 5.1.

6.2.2 Simulation results

In the following section, XPD values extracted from measurements are compared with RT simulations, taking into account the full channel response composed by coherent components, i.e. LOS, reflections and diffractions, and diffuse scattering. The goal is to validate the model presented in Section 6.1.4.

Street canyon scenario

The interactions simulated are: reflection, with maximum order equals to three, double diffraction and single bounce diffuse scattering, with a scattering coefficient $S = 0.4$ and a directive lobe width $\alpha_r = 2$.

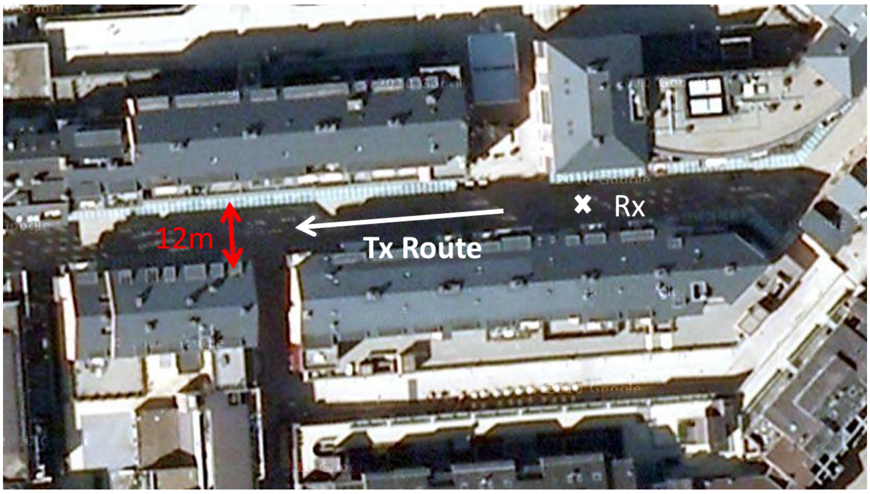

Figure 6.16: Street canyon measurement scenario

In Fig. 6.17 the mean absolute error and the standard deviation of the error computed for all the transmitter positions and for both the antenna configurations are reported, as a function of K_{xpol}: it is evident that the prediction error starts to saturate when $K_{xpol} = 0.2$ is exceeded, and the minimum error is achieved for $K_{xpol} \approx 0.3$. It is worth noticing that in this scenario the observed XPD values are on average very low, and often close to zero, due to the fact that both coherent components and DMC contribute to the polarization coupling. Moreover, the optimum value obtained for the K_{xpol} parameter is even higher than 0.2, which was obtained in the parameterization process for an office building with complex metal frame structure and glass. An explanation of this behaviour could be found in the very complicated structure of some buildings facing to the street canyon, which are full of colonnades, balconies and protruding objects.

In Fig. 6.18 a comparison between the measured and simulated XPD values is shown, for the different positions of the Tx route, using the first antenna configuration (arrays facing to the wall).

In Fig. 6.19 the same results are presented, with reference to the second antenna configuration (arrays oriented along the route direction). In both cases, it can be observed that increasing the K_{xpol} value, i.e. the polarization coupling, the agreement between simulations and measurement improves.

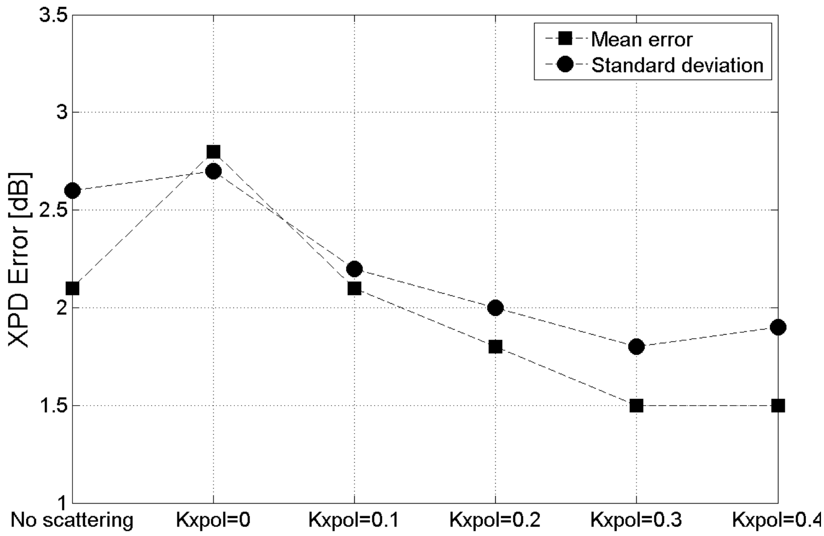

Figure 6.17: Mean prediction error and standard deviation as a function of K_{xpol} in street canyon scenario

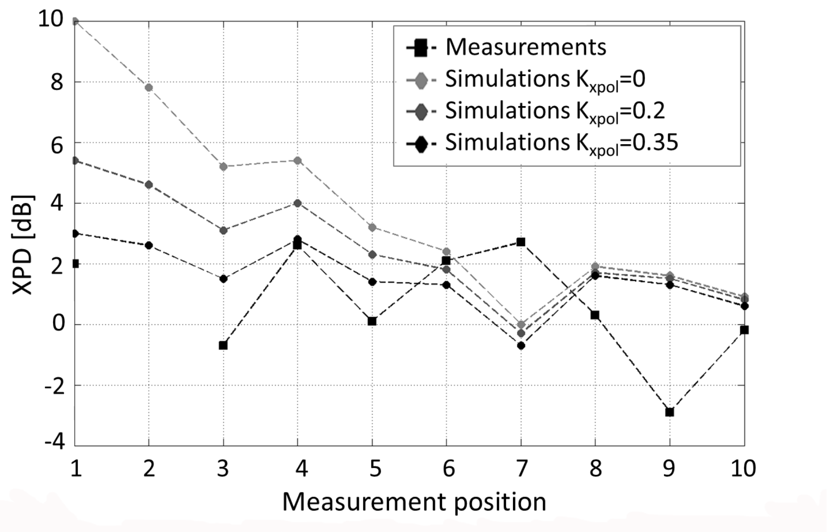

Figure 6.18: Measured vs. simulated XPD for different K_{xpol} values for antenna configuration 1 in the street canyon scenario

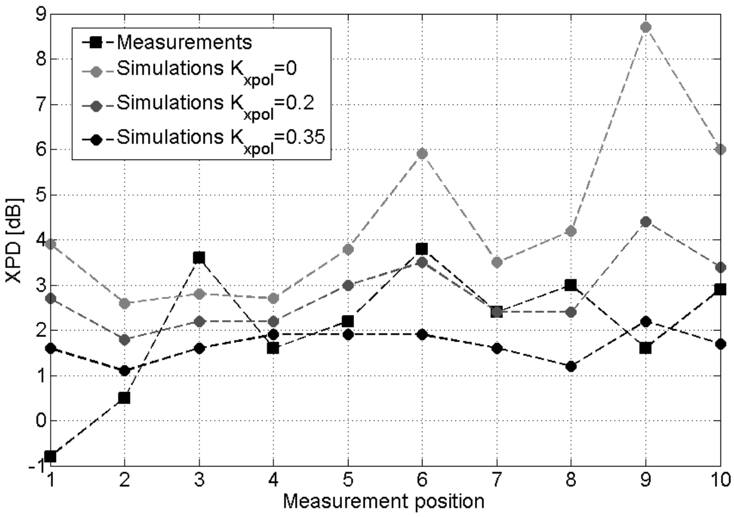

Figure 6.19: Measured vs. simulated XPD for different K_{xpol} values for antenna configuration 2 in the street canyon scenario

Campus scenario

Reflection, with maximum order equals to three, single diffraction and single bounce diffuse scattering are considered in the simulations in this scenario. According to what has been found in Section 5.2, a scattering coefficient $S = 0.4$ and a directive lobe width $\alpha_r = 2$ have been utilized for the simulations.

As it has been done in the other scenario, Fig. 6.20 shows the mean prediction error and its standard deviation for different values of K_{xpol} parameter. Also in this case it seems that $K_{xpol} = 0.3$ minimizes the error. On the other hand, in Fig. 6.21, where XPD is plotted for different values of K_{xpol} for all the measurement positions, it is possible to see that there is a significant overestimation of the measurements between position 8 and position 12. The source of this prediction error might be the presence of trees, leafless at the time of the measurements, that are not taken into account in these simulations. This might tend to create an estimation bias in favor of a higher K_{xpol}, for which XPD is decreased as the error in the positions where there is the overestimation. The XPD results, when scattering by vegetation elements is included in the simulations, are presented in Section 6.3.

In Fig. 6.22 the mean error, already presented in Fig. 6.20, is compared to the one when positions from 8 to 12 are excluded. If the latter case is considered, $K_{xpol} = 0.2$ is the best match when compared with

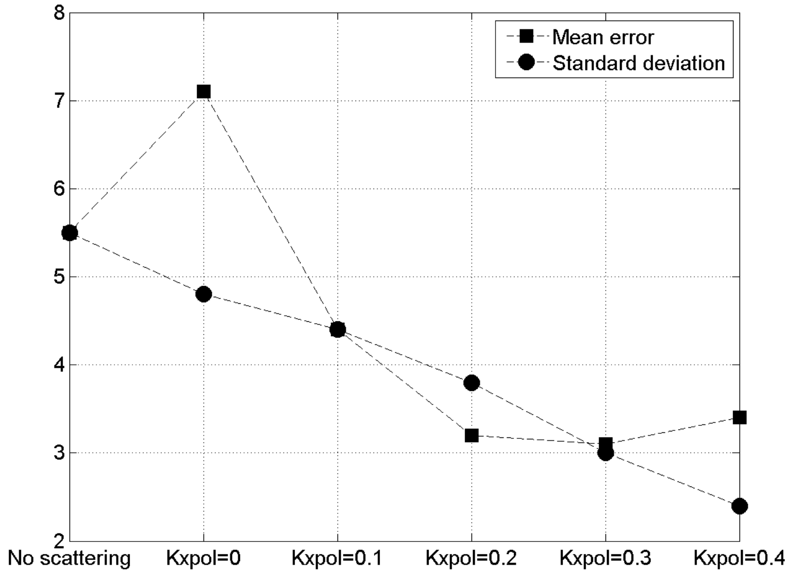

Figure 6.20: Mean prediction error and standard deviation as a function of K_{xpol} in campus scenario

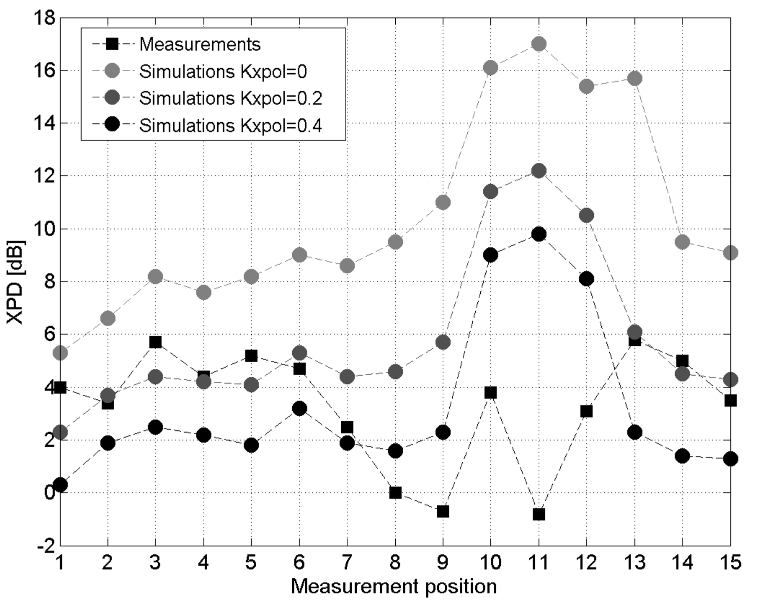

Figure 6.21: Measured vs. simulated XPD for different K_{xpol} values in the campus scenario

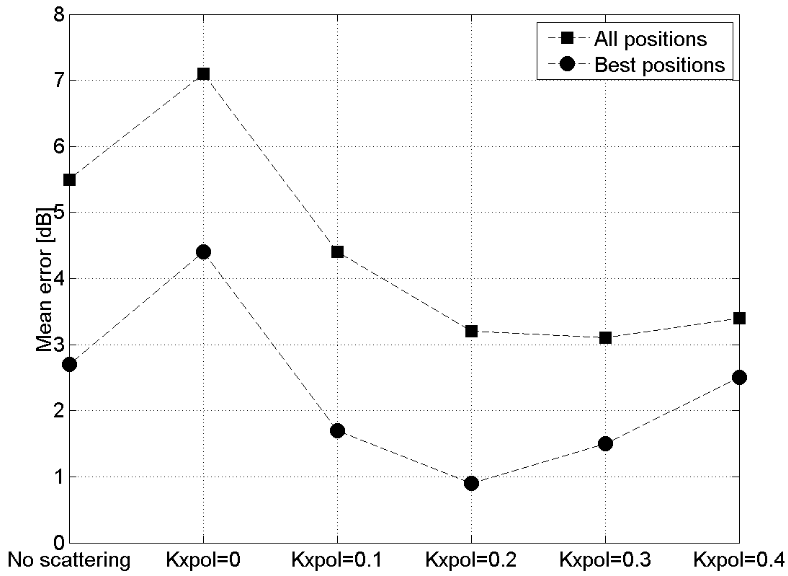

Figure 6.22: Mean prediction error as a function of K_{xpol} in campus scenario with a reduced set of measurement positions

measurements, as it was expected from Fig. 6.21. This confirms the results obtained in the parameterization of the model, where a similar result was found.

6.3 Preliminary evaluations on the impact of scattering by vegetation on XPD

In Section 5.3.2, the importance of scattering by vegetation elements for the prediction of pathloss is presented. Given the results obtained from the validation of the polarization model for scattering by building walls in the campus scenario, the effect of trees in the prediction of XPD is evaluated together with the one of K_{xpol} parameter.

Firstly, the diffuse scattering polarization coefficient is set to $K_{xpol} = 0.2$, according to what is found to be optimum in an office building scenario. Following the results obtained in Section 5.3.2 a linear reduction factor is used for the evaluation of scattering by trees. By analogy with what it is found in the previous sections, the scattering by tree branches interaction it is assumed to depolarize the impinging wave in the follow-

Table 6.7: Summary of the RMSEs for different specific attenuation coefficients

	Weissberger	Single-tree	Torrico-Lang
RMSE [dB]	3.7	3.3	3.2

Table 6.8: Summary of the RMSEs for different K_{xpol} coefficients

	$K_{xpol} = 0$	$K_{xpol} = 0.2$	$K_{xpol} = 0.4$
RMSE [dB]	3.6	3.2	3

ing way:

$$\mathbf{E}_s = \frac{1}{\sqrt{2}} E_r C_r \hat{e}_r + \frac{1}{\sqrt{2}} E_r C_r \hat{e}_{xp} \tag{6.7}$$

where $\hat{e}_r$ is the polarization that the reflected field would have and $\hat{e}_{xp}$ is the polarization orthogonal to $\hat{e}_r$.

Concerning the specific attenuation by vegetation, the Torrico-Lang model, presented in Section 2.5.1, seems to provide a lower RMSE, as shown in preliminary results presented in Table 6.7. This behavior could be expected as this model uses polarization dependent coefficients. They are the following:

$$L_{\theta\theta} = 91 f \chi^{''} \rho_c \frac{\pi h r_c}{\sin\theta_i} \left(\frac{1}{2} \cos^2\theta_i I_1 + \sin^2\theta_i I_2 \right) \tag{6.8}$$

$$L_{\phi\phi} = 45.5 f \chi^{''} \rho_c \frac{\pi h r_c}{\sin\theta_i} I_1 \tag{6.9}$$

where L is the specific attenuation in dB/m, f is the frequency in GHz, $\chi^{''}$ is the imaginary part of $\chi = \epsilon_e - 1$, ρ_c is the density of branches in the canopy, h is the average length and r_c is the average radius of the branches, I_1 and I_2 are parameters that depend on the inclination angles of the branches.

The effect of different values K_{xpol} is tested when both attenuation and scattering by trees are included in the simulations. The comparison with measurements is presented in Fig. 6.23, while Table 6.8 shows the RMSEs for the different cases. The results show that, in accordance with the results without tree contributions presented in Section 6.2.2, $K_{xpol} = 0.4$ seems to minimize the error.

When considering $K_{xpol} = 0.4$, Fig. 6.24 shows the comparison between simulations with and without tree contributions (scattering and attenuation). A significant improvement can be seen in positions 10 to 12, while the prediction is slightly degraded for positions between 13

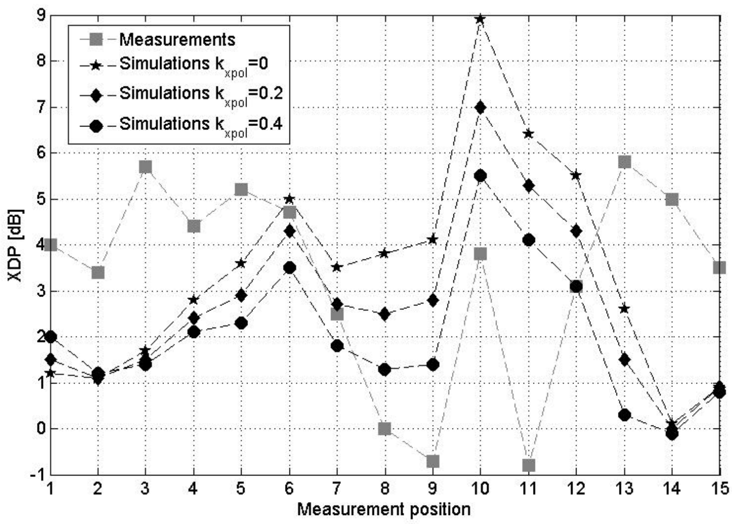

Figure 6.23: XPD when attenuation and scattering by trees is taken into account and for different values of K_{xpol}

and 15. In general, the RMSE is decreased by taking into account the presence of trees from 4.1dB to 3.0dB.

Results presented until this point show that the first tentative model of depolarization due to scattering by tree branches, as in Eq. 6.7, could be improved to achieve a better accuracy. A depolarization coefficient, T_{xp}, similar to the one used in diffuse scattering by building walls is introduces as in the following equation:

$$\mathbf{E}_s = \sqrt{1 - T_{xp}} E_r C_r \hat{e}_r + \sqrt{T_{xp}} E_r C_r \hat{e}_{xp} \tag{6.10}$$

When $T_{xp} = 0.5$ the model is equivalent to Eq. 6.7. Preliminary results show that a T_{xp} higher than 0.5 improves the prediction accuracy. Fig. 6.25 shows a comparison between simulations with $T_{xp} = 0.5$ and $T_{xp} = 0.9$. If positions 8 and 9, where the overestimation of XPD could be linked to the overestimation of the pathloss shown in Section 5.3.2, are excluded the RMSE is reduced from 3.2dB to 2.9dB. Taking as example position 15, where the propagation is dominated by tree scattering, it seems that the scattered wave tends to maintain the polarization of the incident wave. A better model for depolarization may be derived exploiting ad-hoc measurement campaigns focused on vegetated areas.

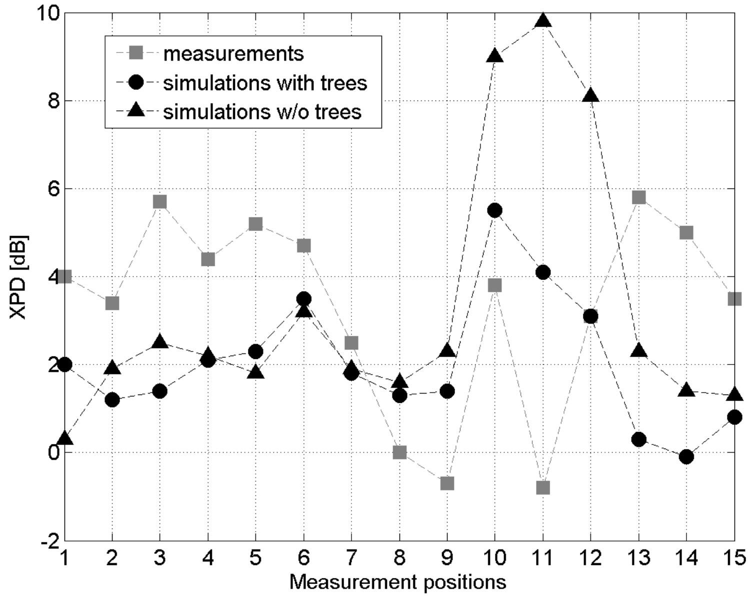

Figure 6.24: Comparison between simulated XPD when tree contributions are included or not

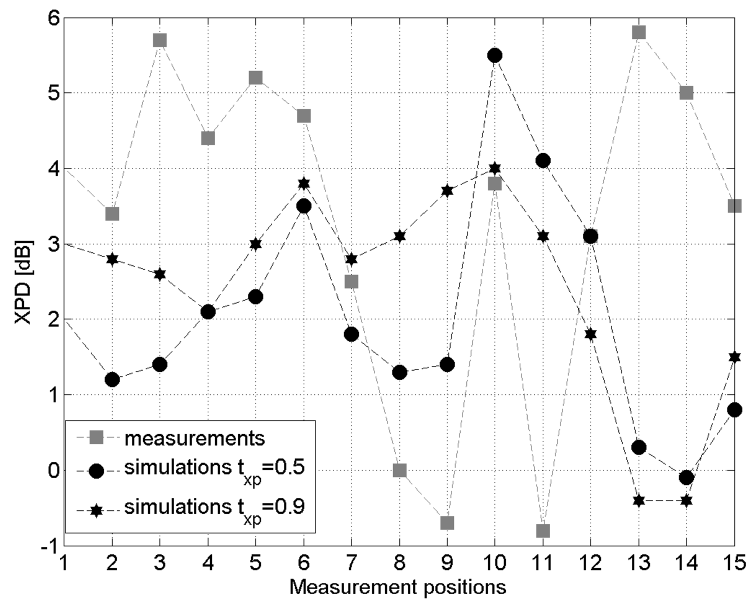

Figure 6.25: Comparison of simulations with different values of T_{xp} for depolarization by vegetation scattering

6.4 Conclusion

This chapter presented the study of polarization behavior of diffuse scattering by building walls and the parameterization and validation of the derived model.

Two isolated single building scenarios have been chosen as reference for the study. In such a scenario, it was possible to exclude contributions not coming from the wall under examination and to determine, using RT tuned with the help of a SAGE-based high resolution algorithm, the coherent components. After subtracting the coherent components from the measurements, diffuse contribution was obtained. Preliminary analysis of the processed data showed that, even in simple environments such as single walls, the diffuse part of the received signal represents a significant contribution to the total power, in particular for the cross-polar channels. Furthermore, the confirmation of the importance of diffuse scattering for an accurate prediction of the polarization behavior of the channel was found.

One of the main advantages of the polarization model is its simplicity. The model relies on a single parameter, K_{xpol}, that sets the amount of power transferred by the scattering interaction into polarization orthogonal to a reference one. The adopted reference polarization is the one of specular reflection. This choice followed the results obtained from measurements so that $K_{xpol} = 0$ produces the highest level of XPD. Once the K_{xpol} parameter is implemented into the diffuse scattering model for RT, the comparison with values extracted from measurements brings to the following conclusions:

- for a simple and homogeneous wall, such as a brick wall in a rural building, diffuse scattering yields very low depolarization, $K_{xpol} \approx 0$,
- for a more complex wall structure, such as the wall of the tested office building, the depolarization of diffuse rays is not negligible, and $K_{xpol} = 0.2$ is the best match.

In the second part of this chapter, the polarization model for diffuse scattering is validated in two complex outdoor scenarios. Good agreement between measurements and RT simulations has been obtained and the improvement in the XPD prediction after the implementation of the polarization model is evident. In the street canyon scenario, due to the presence of balconies and other protruding objects, the optimal value for K_{xpol} seems to be even higher than the one found in the parameterization process.

Finally, in the campus scenario, the effect of trees is taken into account to improve the results in term of XPD. Despite the reduction of the XPD prediction error, the model for polarization behavior of scattering by vegetation elements is still not accurate. An ad-hoc measurement campaign would be needed to improve it.

7

Practical applications of Ray-Tracing

In this last chapter three examples of practical applications of the advanced RT tool are presented: RT simulations to be used as input for a localization algorithm, RT simulations to be used to train a detection algorithm for surveillance in industrial scenarios and RT simulations in an airport scenario.

7.1 Ray-Tracing for indoor localization

RT simulations are used, together with measurements, to test a localization algorithm for indoor scenarios. The correlation-based algorithm tries to estimate the position of distributed nodes, without knowledge of transmitter locations or the transmitted signal, by computing pairwise cross-correlations of the signals received at the nodes, exploiting spatial and time diversity [105].

To have consistency with the environment where the measurements were carried out, an office at Stanford University, the simulations are performed modeling a cubicle-style office scenario. The dimensions of the room are to 50×20m with a height of 4m. The walls, the ceiling, and the floor are supposed to be made of concrete. Cubicles are $4 \times 3 \times 1.8$m and are organized in two rows. They are represented by their metallic frames that have been treated as perfect electric conductors. A number of 14 receiving nodes were placed in the cubicles and the surrounding area, while the transmitted signals are generated by 14 sources placed at the walls of the room. At both sides, the antennas are placed at an height of 1m. The 2-D map of the simulated scenario together with position of transmitter and receivers is shown in Fig. 7.1.

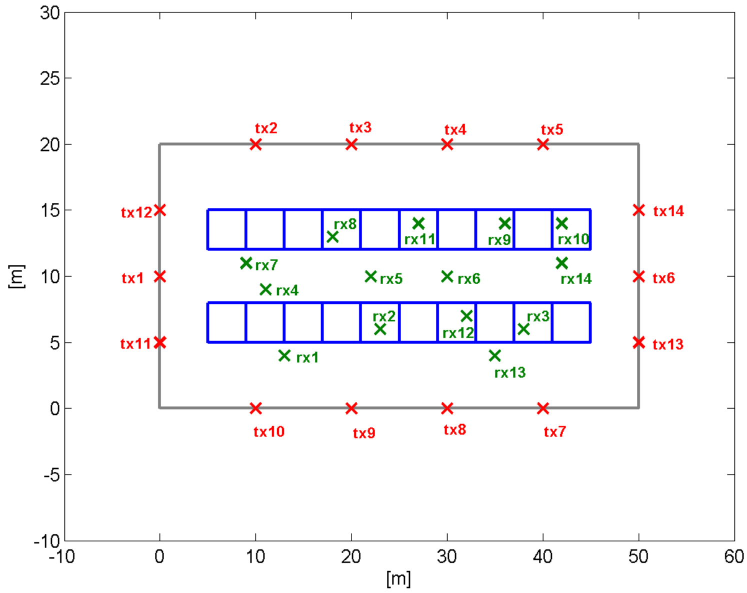

Figure 7.1: 2-D map of the simulated scenario for localization with position of transmitters (in red) and receivers (in green) for simulations

The time variance of the channel has been simulated by creating 100 different realizations of the channel environment. In each realization ten persons are randomly placed in the scenario. A rough model for the human body as a rectangular parallelepiped has been used to achieve this.

The simulation frequency has been set to 2.45GHz. The antennas used for the simulations are vertically polarized ideal half-wavelenght dipoles both at receive and transmit side. Whenever transmitters are placed at walls, they radiate only into the relative half-space. A maximum order of reflection equal to three, single diffraction, and single bounce scattering have been used in the simulations. A directive scattering pattern model with scattering coefficient $S = 0.4$ and beamwidth $\alpha_r = 4$ has been chosen, according to what has been found in Section 4.2.2. The simulation results were filtered using a rectangular filter in frequency domain with a bandwidth of $240MHz$, in accordance with the measurement characteristics. The dielectric properties used in the simulations are shown in Table 7.1. For the human body, a classic two-thirds muscle homogeneous model [106] has been adopted.

Fig. 7.2 presents results of the localization algorithm based on RT simulations presented in this Section.

Material	ϵ_r	$\sigma\,[S/m]$
Reinforced concrete	9	0.06
Human body	35.2	1.16

Table 7.1: Material properties for localization simulations

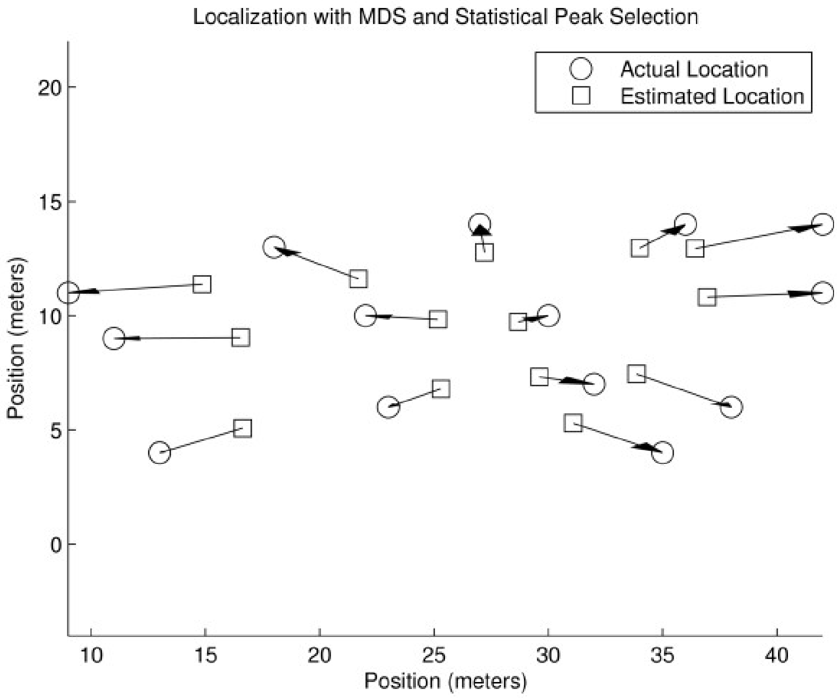

Figure 7.2: Results of the localization algorithm based on RT simulations [105]

7.2 Ray-Tracing for radio surveillance in industrial scenarios

In the framework of a project that is intended to develop a technology to detect the degradation or motion of goods stored in a warehouse or in a truck, RT simulations in industrial scenarios are carried out to be combined with measurements. The importance of the characterization of the propagation channel in this case is given by the fact that the channel itself, whose variation is tracked and used as input for a classification algorithm, is the information.

Both truck and warehouse simulation scenarios have been investigated to provide simulated channels to be used for testing the detection algorithm. In each scenario two frequencies, 868 MHz and 2.4 GHz, have been exploited. Simulated radiation patterns of a dual frequency and dual polarized microstrip antennas, developed in the framework of the same project, have been implemented.

The virtual truck is 8.5m long, 2.5m wide and 2.5m high, starting from an elevation of 80cm from the ground. Its floor is made of wood, while the structure is composed by horizontal and vertical metallic bars. The goods are supposed to be arranged in boxes. Two series of simulations have been performed: the first one with small boxes and the second one with big boxes. Small boxes are cubes with 50cm edges. They are disposed in six double rows, each with a height of 2 boxes. Big boxes are cubes with 1m edges. Four of them are placed in the truck trailer. The virtual warehouse is a room of 375m^2 and 5m high. The walls, the ceiling and the floor are made of concrete and there are four rows of metallic shelves 22m long and 3.7m high for the storage of small boxes.

An array of four dual polarized and dual frequency antennas are placed both at transmit and receive side, that are opposite sides of the truck or of the warehouse, at an height of 1.5m from the floor in both scenarios.

Tab 7.2 and Tab 7.3 show the dielectric properties of the materials involved in the propagation at both frequencies. Water has been chosen as material stored in the boxes for its high permittivity and representing a generic kind of liquid. The human intruders have been represented by parallelepipeds for which a classic two-thirds muscle homogeneous model [106] has been used to get realistic values of permittivity and conductivity. In all the simulations, a maximum order of reflection equal to three, single diffraction and single bounce scattering are taken into account.

In each environment, the following realizations have been simulated:

Material	ϵ_r	$\sigma\,[S/m]$
Wood	2.5	0.02
Water	75	0.47
Muscle	55.1	0.93
Concrete	6	0.06

Table 7.2: Material Properties for industrial scenario at 868 MHz

Material	ϵ_r	$\sigma\,[S/m]$
Wood	2	0.03
Water	75	1.25
Muscle	52.8	1.7
Concrete	7	0.03

Table 7.3: Material Properties for industrial scenario at 2.4 GHz

- normality, that is the original situation before any perturbation,
- changes of the dielectric properties of the liquid material stored to simulate degradation or leakage,
- removal of boxes or rows of boxes from the scenario,
- empty truck or warehouse, i.e. all the boxes removed from the scenario,
- one or two intruders, modeled as dielectric parallelepipeds, inside the scenario,
- a car or a truck parked close to the trailer under surveillance (only in truck scenario).

For each realization 128 different channels

$$(4_{TxAntennas} \times 2_{Polarizations}) \times (4_{RxAntennas} \times 2_{Polarizations}) \times 2_{Frequencies} \tag{7.1}$$

are evaluated. It is consequently possible to exploit and combine space, frequency and polarization diversity to improve the accuracy of the detection.

As an example, the results of the warehouse environment are presented for a single co-polar channel. A unitary power is assumed at transmit side. Fig. 7.3 shows the received power for the 8 frequency and polarization configurations concerning the scenario with changes of the dielectric properties of the liquid material stored due to leakage.

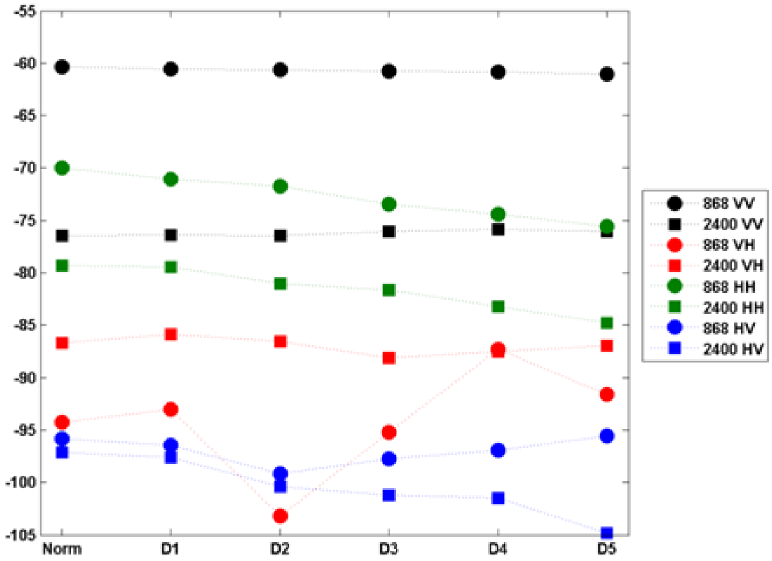

Figure 7.3: Received power in the warehouse environment for scenario with changes of dielectric properties

The label $Norm$ in the x-axis refers to the normality simulation that is the reference one. Labels from $D1$ to $D5$ refer to decreasing values of dielectric values.

In analogous way, Fig. 7.4 shows the received power for scenario configurations where some of the boxes are removed from the warehouse. Labels from $B1$ to $B4$ refer to different set of boxes removed from the environment, while label *Empty* refer to the situation where all the boxes are removed.

Figs. 7.5 and 7.6, instead, show the results for the single intruder and two intruders scenarios, respectively. The graphs present the case when intruders are present in the surveillance area in different positions (labels from $T1$ to $T5$).

Taking as example Fig. 7.5, it is possible to see how diversity may help in detecting an intruder in the surveillance area. While the Vertical-to-Vertical (VV) polarization channels may detect intruder in position 2, Horizontal-to-Horizontal (HH) looks suitable to detect when the intruder is in position 1, while VH and HV may provide an alarm in position 3 and position 5 respectively.

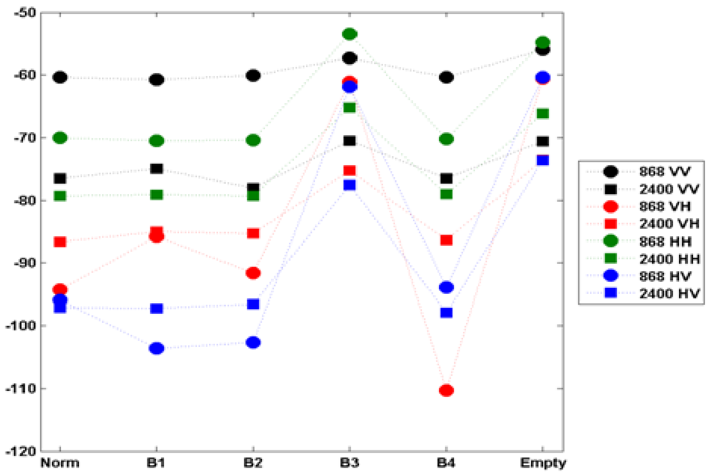

Figure 7.4: Received power in the warehouse scenario for scenario with boxes removed from surveillance zone

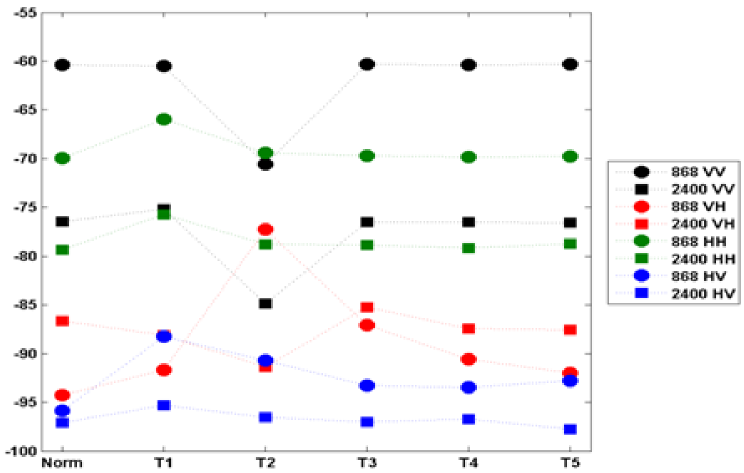

Figure 7.5: Received power in the warehouse scenario for scenario with a single intruder

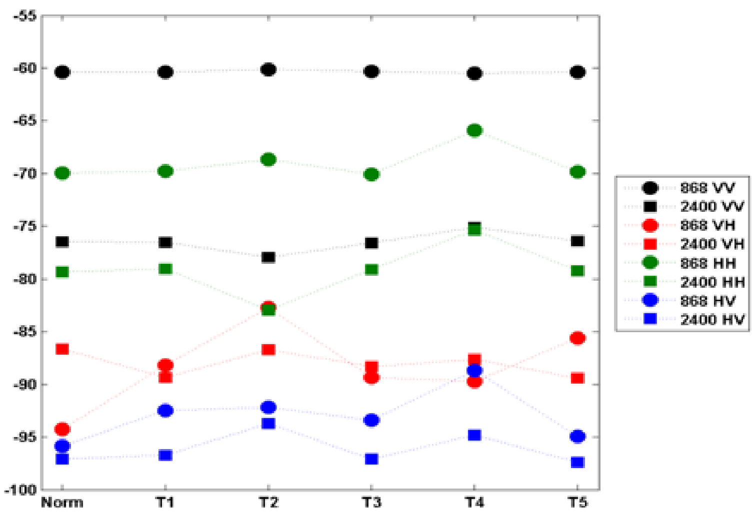

Figure 7.6: Received power in the warehouse scenario for scenario with two intruders

7.3 Propagation in an airport scenario

This section presents preliminary results of RT simulations in a simplified airport environment. The goal is to evaluate through simulations the received power in a scenario with a fixed base station at transmit side and a mobile terminal, which position can be both outdoor and indoor, at receive side.

The scenario used in these simulations represents a simplified model of Charleroi airport. Fig. 7.7 shows the 2D plan of the environment. Two positions for the BS antenna, at opposite side of the runaway, have been considered as shown in the picture. The block in red represents the firefighter building, that is the indoor location where the MT is considered moving. Fig. 7.8 shows the schematization of the building modeled in the RT input database, together with the routes followed by the MT.

The frequency used in the simulations is 425MHz, i.e. the TETRA frequency at Charleroi Airport. Dipole antennas are used both at Tx and Rx side. BS dipoles are placed on top of buildings while MT is placed at a height of 1.8m. Table 7.4 presents the dielectric properties of the materials used in the simulations.

In the preliminary simulations, a maximum of triple reflection and single diffraction are employed and no scattering is included. Following

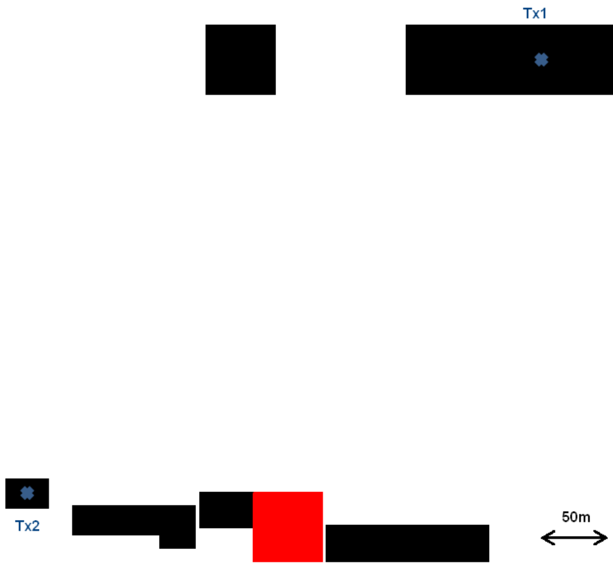

Figure 7.7: 2D Plan of the airport scenario with BS positions

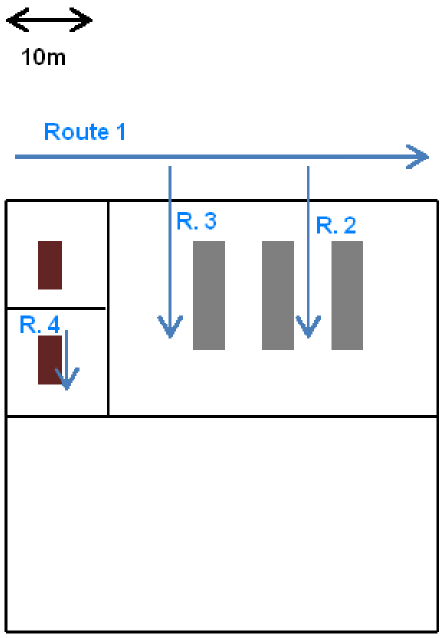

Figure 7.8: 2D Plan of the firefighters building with MT routes

Table 7.4: Dielectric properties of materials in airport scenario

Material	ϵ_r	$\sigma\,[S/m]$
Concrete	7	0.02
Plyood	3	0.007
Brick	4.45	0.003

Figure 7.9: Outdoor route 1 for Tx position 1

this choice, the simulation time does not exceed 10s.

Moreover, a first rough model of an airplane has been attempted. The fuselage has been modeled as an ellipsoid. Reflection on a curved surface is implemented, following what is presented in Section 2.2. Wings and tail are modeled as thin parallelepipeds. The dimensions of the plane are the ones of a Boeing 737-800 [107].

RT simulation results are presented in terms of received power considering antennas with unitary gain and unitary transmit power. One simulation each meter is evaluated for all the routes. Concerning Tx position 1, that is placed on the opposite side of the runaway with respect to the firefighters building, Fig. 7.9 shows the results for the outdoor route 1. Fig. 7.10 and Fig. 7.11, instead, refers to the outdoor to indoor routes 2 and 3. The gap that can be seen in the graphs is due to the transition from outdoor to indoor, where two simulations are skipped.

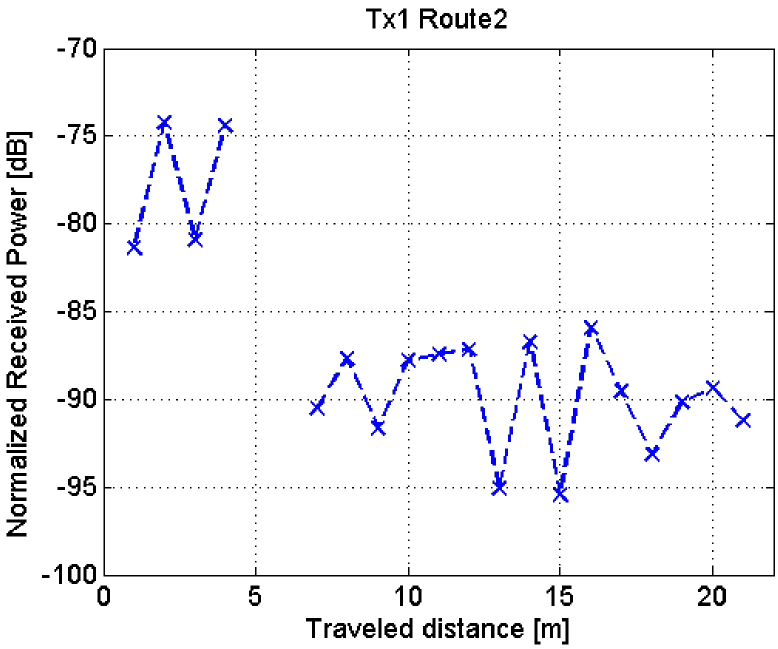

Figure 7.10: Outdoor to indoor route 2 for Tx position 1

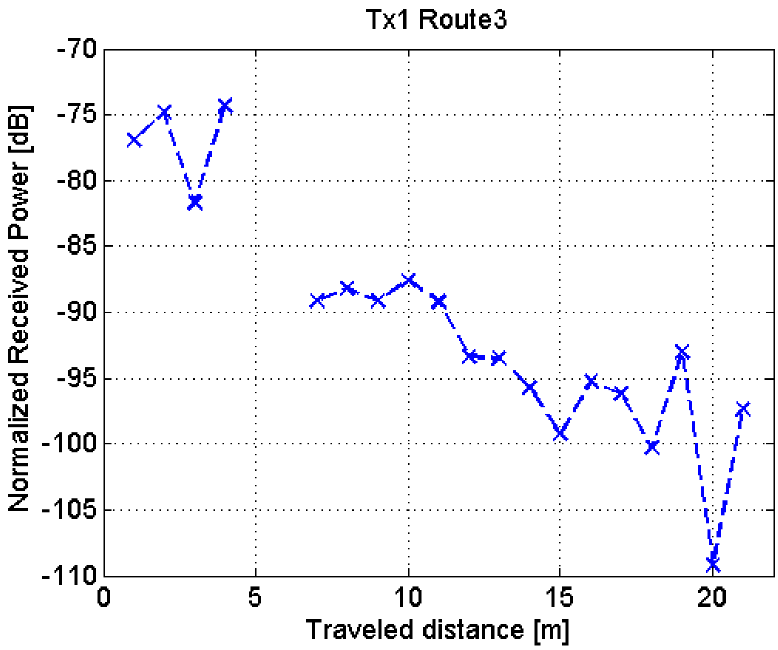

Figure 7.11: Outdoor to indoor route 3 for Tx position 1

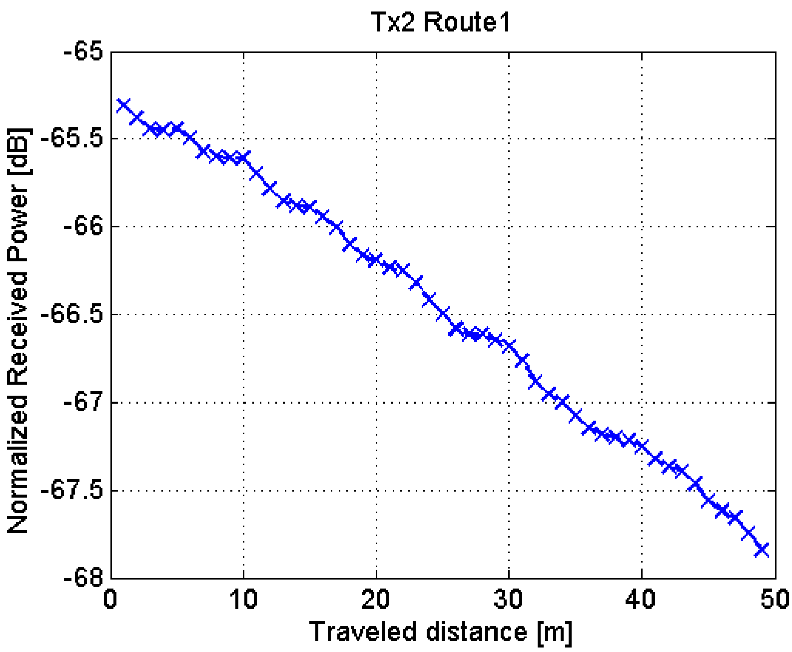

Figure 7.12: Outdoor route 1 for Tx position 2

Fig. 7.12 shows again the simulated results for the outdoor route 1, but in this case for Tx position 2. In route 1 propagation is dominated by LOS, so the received power is higher than for Tx1 because the BS is closer to the MT. When Tx position 2 is utilized for route 2 and 3, no ray is predicted arriving at the MT in indoor positions. This is due to the relative position of the two antennas and the interposition of several buildings that are considered non-penetrable between the terminals.

Then, the airplane model is placed in two positions in the scenario, as shown in Fig. 7.13. The choice of the two positions is made to impact the two different BS scenario. Airplane position 1 is in the LOS propagation zone of Tx1 and airplane position 2 is in a zone where it can produce a reflecion towards MT routes for Tx2. Route 1 and route 2 have been tested with this new configuration.

As examples, Fig. 7.14 and Fig. 7.15 show the received power results with the airplane in position 1 for route 1 and 2 respectively. In both cases Tx1 is considered, since is the one influenced by the presence of the airplane in that position. No significant difference with respect to the case without airplane can be seen on route 2, while up to 2dB difference can be noticed on route 1.

In the following steps of this work, a realistic and more detailed map of Charleroi airport is going to be employed as input for the simulations.

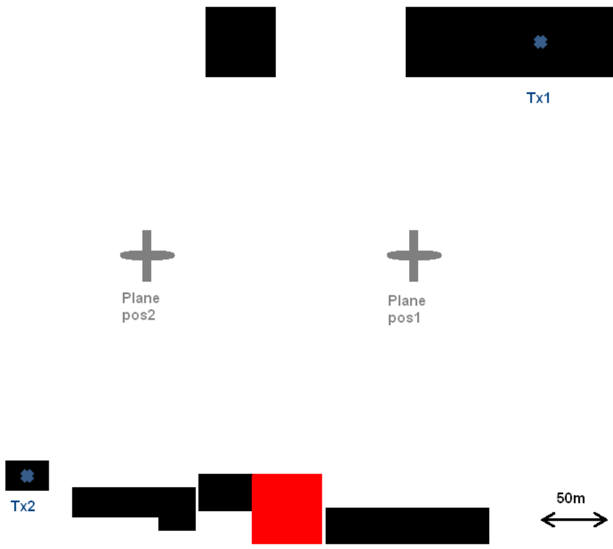

Figure 7.13: 2D Plan of the airport scenario with two airplane posititions

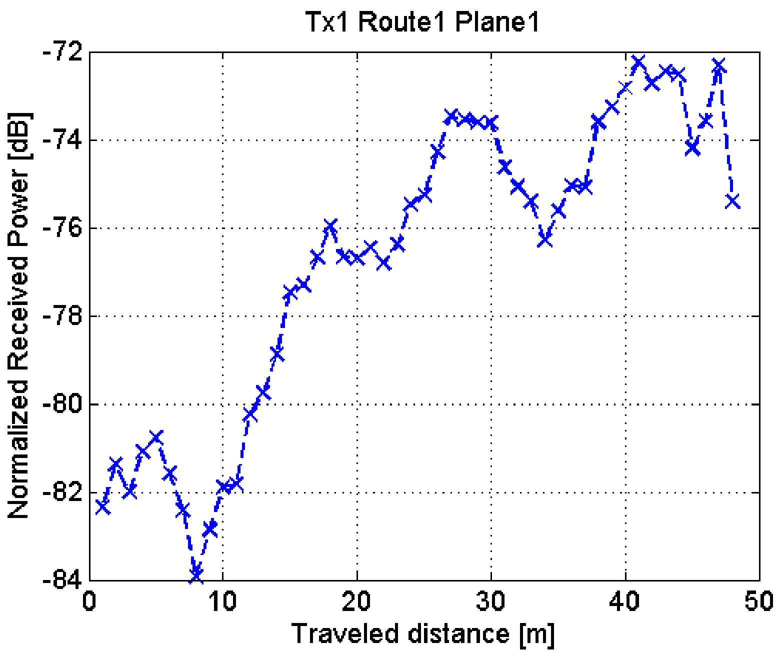

Figure 7.14: Outdoor route 1 for Tx position 1 with airplane in position 1

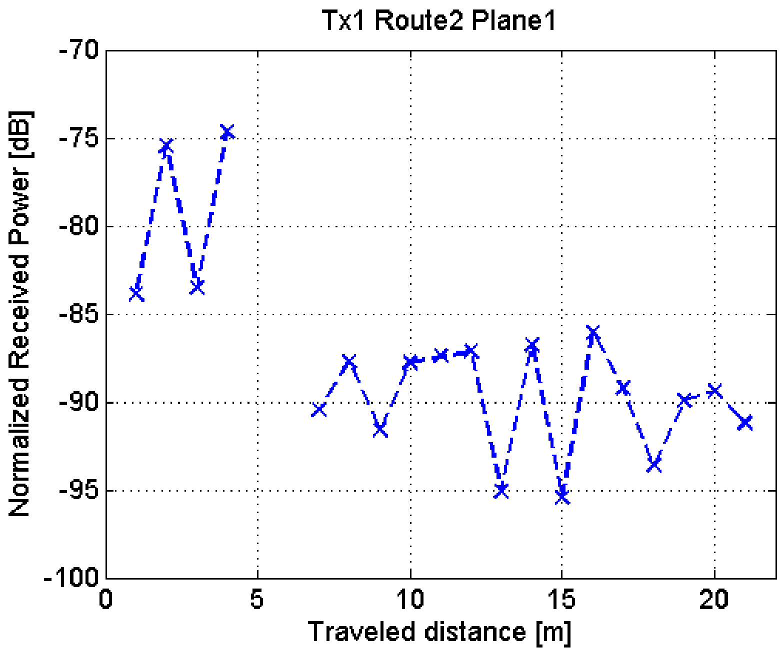

Figure 7.15: Outdoor to indoor route 2 for Tx position 1 with airplane in position 1

The full airport ground is going to be divided in cells with sides of 10m and a simulated level of pathloss is going to be associated with each cell. Simulations will be run also in the firefighters building and measurements are foreseen to validate the simulation results. Finally, a combination of Method of Moments and RT will be employed to take into account the presence of airplanes in the airport ground.

8

Conclusion

In this thesis, a pre-existent RT tool has been improved with penetration, diffuse scattering and other propagation mechanisms to achieve the state of the art level in channel modeling. RT, a deterministic propagation model based on GO and UTD, is a useful tool to model specific propagation channels. One of its most important values is the extreme adaptability, e.g.

- it can be used both in outdoor and indoor scenarios (or in outdoor-to-indoor ones),
- it can model the propagation channel with any type of antenna plugged in, as well as an antenna de-embedded channel,
- from its results it is possible to evaluate any channel metric, from the simplest to the most complex.

The improved version of RT has been validated versus measurements in some representative scenarios, both outdoor and indoor. The results showed that the improved version of the RT generally achieved good accuracy. In particular, one significant result is the validation, versus parameters extracted from measurements with an high-resolution algorithm, of the angular properties in an indoor scenario. The capability of the RT tool to predict with good accuracy the directional properties of the channel was demonstrated with a specific focus on the angular properties of diffuse scattering. On the other hand, one of the critical points that RT showed is the capability of predicting delay spreads, both in indoor and outdoor scenarios. This can be partially improved increasing the maximum order of different mechanisms, but at the severe cost of computation time.

The importance of diffuse scattering for the prediction of polarization behaviour of the channel was confirmed both in outdoor and indoor

Table 8.1: Summary of the suggested diffuse scattering parameters depending on the scenario

Scenario	Pattern model	S	K_{xpol}	α_r
Industrial indoor	Lambertian	0.4	N.D.	-
Office indoor	Directive	0.4	N.D.	1
Simple outdoor (rural)	Directive	0.4	0	2
Complex outdoor (office)	Directive	0.6	0.2	2

environments. In this regard, a polarization model for diffuse scattering, that relies on a single parameter (K_{xpol}), has been derived and parameterized from ad-hoc single-wall measurements in outdoor scenarios. The results showed that in a simple and homogeneous wall, such as a brick wall in a rural building, diffuse scattering yields very low depolarization, while in a more complex wall structure, as a brick and glass wall with metallic frames, the depolarization of diffuse rays is not negligible. The validation of the model in classical outdoor environments showed a significant improvement in XPD predictions.

Table 8.1 presents a summary of suggested diffuse scattering parameters depending on the scenario under consideration, resulting from the parameterizations and validations carried out during this thesis. It has to be noted that the polarization properties of diffuse scattering have been studied only in outdoor scenarios thus, the value of K_{xpol} in indoor cases is not determined.

During this thesis, a novel method to evaluate scattering by tree branches has been introduced. This method has been developed to be easily included in the RT tool. The performance of the model has been tested with channel measurements in an outdoor scenario in presence of trees out of foliage. The comparison showed that, in such environments, attenuation by vegetation is not sufficient to model tree contribution and that scattering plays a decisive role to correctly evaluate the received power. When scattering is added to the attenuation, the received power prediction error is reduced significantly.

The thesis is concluded with some practical example of channel modeling applications, where the RT tool has been used. Despite the fact that, at this stage, this RT can be used with good results in most applications, research in general and the possible extensions of RT in particular can be never-ending. Thus, before concluding, some ideas of possible future work to improve the tool are provided. One of the most significant improvement that can be done is implementing a speed-up method to decrease computation times. On a related matter, some work could be done to make more efficient the C-code on the programming side. At this moment, a time-variant channel can be modeled by successive simulations, where the mobile terminal (and/or any block representing a mobile object) is placed in different positions. To make time-variant RT more efficient, subspace methods as the sum-of-complex-exponentials (SoCE) or the discrete prolate spheroidal sequences (DPSS) [108], already used in GSCMs, could be employed.

Concerning improvements from the interactions point of view, the scattering by tree branches model, introduced in this thesis, can be improved focusing ad-hoc measurements towards this goal. Results presented in Chapter 4 showed good accuracy in XPD prediction even before the implementation of the diffuse scatting polarization model. As power was divided equally between the two components, this could suggest that in indoor scenarios $K_{xpol} \rightarrow 0.5$. To check this assumption or to verify if the accuracy could be improved, another interesting step would be testing and parameterizing this polarization model in some typical indoor scenario. To this end, the diffuse scattering component has to be extracted from measurements with the help of high-resolution algorithms, as it is impossible to isolate coherent components just from geometrical considerations and it is not possible to identify a simple, single-surface, indoor scenario.

Bibliography

[1] C. Oestges, B. Clerckx, L. Raynaud, and D. Vanhoenacker-Janvier, "Deterministic channel modeling and performance simulation of microcellular wide-band communication systems," *IEEE Transactions on Vehicular Technology*, vol. 51, no. 6, pp. 1422–1430, November 2002. 1, 27, 31, 34

[2] C. Shannon, "A mathematical theory of communication," *Bell System Technical Journal*, vol. 28, pp. 379–423 and 623–56, 1948. 3, 4

[3] S. R. Saunders, *Antennas and Propagation for Wireless Communication Systems.* Wiley, 1999. 3, 6, 17

[4] A. Goldsmith, *Wireless Communications.* Cambridge University Press, 2005. 6, 7

[5] V. Erceg, L. Greenstein, S. Tjandra, S. Parkoff, A. Gupta, B. Kulic, A. Julius, and R. Bianchi, "An empirically based path loss model for wireless channels in suburban environments," *IEEE Journal on Selected Areas in Communications*, vol. 17, no. 7, pp. 1205 –1211, Jul. 1999. 7

[6] S. Ghassemzadeh, L. Greenstein, A. Kavcic, T. Sveinsson, and V. Tarokh, "UWB indoor path loss model for residential and commercial buildings," in *IEEE 58th Vehicular Technology Conference (VTC-2003 Fall)*, vol. 5, Oct. 2003, pp. 3115–3119. 7

[7] T. S. Rappaport, *Wireless Communications.* Prentice Hall, 1996. 7

[8] A. Molisch, *Wireless Communications.* John Wiley & Sons, 2005. 8, 55, 61

[9] M. Hata, "Empirical formula for propagation loss in land mobile radio services," *IEEE Transactions on Vehicular Technology*, vol. 29, no. 3, pp. 317 – 325, Aug. 1980. 9

[10] COST231, "Digital mobile radio: COST231 view on the evolution towards third generation systems," European Commission/COST Telecommunications, Tech. Rep., 1998. 9, 83

[11] A. Saleh and R. Valenzuela, "A statistical model for indoor multipath propagation," *IEEE Journal on Selected Areas in Communications*, vol. 5, no. 2, pp. 128 –137, Feb. 1987. 10

[12] P. Almers, E. Bonek, A. Burr, N. Czink, M. Debbah, V. Degli-Esposti, H. Hofstetter, P. Kyosti, D. Laurenson, G. Matz, A. Molisch, C. Oestges, and H. Ozcelik, "Survey of channel and radio propagation models for wireless MIMO systems," *EURASIP Journal on Wireless Communications and Networking*, vol. 2007, no. 1, 2007. 10

[13] F. Quitin, "Channel modeling for polarized MIMO systems," Ph.D. dissertation, Université libre de Bruxelles, 2011. 10, 92

[14] N. Czink, X. Yin, H. Ozcelik, M. Herdin, E. Bonek, and B. Fleury, "Cluster characteristics in a MIMO indoor propagation environment," *IEEE Transactions on Wireless Communications*, vol. 6, no. 4, pp. 1465 –1475, Apr. 2007. 10

[15] B. Gschwendtner, G. Wölfe, B. Burk, and F. Landstorfer, "Ray tracing vs. ray launching in 3-D microcell modelling," in *1st European Personal and Mobile Communications Conference (EPMCC)*, Bologna, Italy, Nov. 1995. 12

[16] G. Durgin, N. Patwari, and T. Rappaport, "Improved 3D ray launching method for wireless propagation prediction," *Electronics Letters*, vol. 33, no. 16, pp. 1412 –1413, Jul. 1997. 12

[17] M. Lawton and J. McGeehan, "The application of a deterministic ray launching algorithm for the prediction of radio channel characteristics in small-cell environments," *IEEE Transactions on Vehicular Technology*, vol. 43, no. 4, pp. 955 –969, Nov. 1994. 12

[18] D. McNamara, C. Pistorius, and J. Malherbe, *Introduction to the Uniform Geometrical Theory of Diffraction*. Artech House, 1990. 13, 18, 19, 35, 36, 38, 53, 141

[19] B. H. Walker, *Optical engineering fundamentals*. SPIE Publications, 1998. 13

[20] R. K. Verma, *Ray Optics*. Discovery Publishing House, 2006. 13

[21] J. Keller, "Geometrical theory of diffraction," *Journal of the optical society of America*, vol. 52, no. 2, pp. 116–130, Feb. 1962. 15

[22] R. Kouyoumjian and P. Pathak, "A uniform geometrical theory of diffraction for an edge in a perfectly conducting surface," *Proceeding of the IEEE*, vol. 62, no. 11, pp. 1448–1461, Nov. 1974. 16, 37

[23] P. Beckmann and A. Spizzichino, *The scattering of electomagnetic waves from rough surfaces.* Artech House, 1987. 17

[24] M. Kline and I. Kay, *Electromagnetic theory and geometrical optics.* John Wiley & Sons, 1965. 18

[25] G. Deschamps, "Ray techniques in electromagnetics," *Proceedings of the IEEE*, vol. 60, no. 9, pp. 1022 – 1035, Sep. 1972. 19

[26] W. Stutzman, *Polarization in elctromagnetic systems.* Artech House, 1993. 20, 24

[27] C. Balanis, *Antenna Theory.* John Wiley & Sons, Inc., 2005. 22

[28] G. Athanasiadou, A. Nix, and J. McGeehan, "A microcellular ray-tracing propagation model and evaluation of its narrow-band and wide-band predictions," *IEEE Journal on Selected Areas in Communications*, vol. 18, no. 3, pp. 322 –335, Mar. 2000. 25, 26, 27, 79

[29] R. Fritzsche, J. Voigt, C. Jandura, and G. Fettweis, "Verifying ray tracing based CoMP-MIMO predictions with channel sounding measurements," in *2010 International ITG Workshop on Smart Antennas*, Feb. 2010, pp. 161 –168. 25, 26

[30] T. Fugen, J. Maurer, T. Kayser, and W. Wiesbeck, "Capability of 3-D ray tracing for defining parameter sets for the specification of future mobile communications systems," *IEEE Transactions on Antennas and Propagation*, vol. 54, no. 11, pp. 3125 –3137, Nov. 2006. 25, 26, 27

[31] V. Degli Esposti, D. Guiducci, A. de'Marsi, P. Azzi, and F. Fuschini, "An advanced field prediction model including diffuse scattering," *IEEE Transactions on Antennas and Propagation*, vol. 52, no. 7, pp. 1717 – 1728, Jul. 2004. 25, 26

[32] F. Fuschini, H. El-Sallabi, V. Degli Esposti, L. Vuokko, D. Guiducci, and P. Vainikainen, "Analysis of multipath propagation in urban environment through multidimensional measurements and advanced ray tracing simulation," *IEEE Transactions on Antennas and Propagation*, vol. 56, no. 3, pp. 848 –857, Mar. 2008. 25, 26, 27

[33] H.-J. Li, C.-C. Chen, T.-Y. Liu, and H.-C. Lin, "Applicability of ray-tracing technique for the prediction of outdoor channel characteristics," *IEEE Transactions on Vehicular Technology*, vol. 49, no. 6, pp. 2336 –2349, Nov. 2000. 25, 26, 27

[34] Y. Corre and Y. Lostanlen, "Three-dimensional urban EM wave propagation model for radio network planning and optimization over large areas," *IEEE Transactions on Vehicular Technology*, vol. 58, no. 7, pp. 3112 –3123, Sep. 2009. 25, 26

[35] T. Rautiainen, G. Wolfle, and R. Hoppe, "Verifying path loss and delay spread predictions of a 3D ray tracing propagation model in urban environment," in *IEEE 56th Vehicular Technology Conference, VTC 2002-Fall*, vol. 4, 2002, pp. 2470 – 2474. 25, 26

[36] G. Athanasiadou and A. Nix, "A novel 3-D indoor ray-tracing propagation model: the path generator and evaluation of narrow-band and wide-band predictions," *IEEE Transactions on Vehicular Technology*, vol. 49, no. 4, pp. 1152 –1168, Jul. 2000. 25, 26, 27

[37] F. Saez de Adana, O. Gutierrez Blanco, I. Gonzalez Diego, J. Perez Arriaga, and M. Catedra, "Propagation model based on ray tracing for the design of personal communication systems in indoor environments," *IEEE Transactions on Vehicular Technology*, vol. 49, no. 6, pp. 2105 –2112, Nov. 2000. 25, 26

[38] E. Haddad, N. Malhouroux, P. Pajusco, and M. Ney, "Optimization of 3D ray tracing for MIMO indoor channel," in *2011 XXXth URSI General Assembly and Scientific Symposium*, Aug. 2011, pp. 1 –4. 25, 26

[39] M. Janson, J. Pontes, C. Sturm, and T. Zwick, "BER simulations of a UWB spatial multiplexing system using an extended ray-tracing approach," *IEEE Antennas and Wireless Propagation Letters*, vol. 9, pp. 1096 –1098, 2010. 25, 26, 27

[40] S. Seidel and T. Rappaport, “Site-specific propagation prediction for wireless in-building personal communication system design,” *IEEE Transactions on Vehicular Technology*, vol. 43, no. 4, pp. 879–891, Nov. 1994. 25, 26, 27

[41] T. Rautiainen, R. Hoppe, and G. Wölfle, “Measurements and 3D ray tracing propagation predictions of channel characteristics in indoor environments,” in *IEEE Symposium on Personal, Indoor and Mobile Radio Communications*, Athens, Greece, Sept. 3-7 2007. 25, 26, 27

[42] A. Burr, “Evaluation of capacity of indoor wireless MIMO channel using ray tracing,” in *2002 International Zurich Seminar on Broadband Communications*, 2002, pp. 28–1 –28–6. 25, 27

[43] C. Sturm, W. Sorgel, T. Kayser, and W. Wiesbeck, “Deterministic UWB wave propagation modeling for localization applications based on 3D ray tracing,” in *IEEE 2006 MTT-S International Microwave Symposium Digest*, Jun. 2006, pp. 2003 –2006. 26, 27

[44] V. Degli Esposti, F. Fuschini, E. M. Vitucci, and G. Falciasecca, “Measurement and modelling of scattering from buildings,” *IEEE Transactions on Antennas and Propagation*, vol. 55, no. 1, pp. 143–154, Jan. 2007. 26, 41, 121, 143

[45] Y. de Jong and M. Herben, “A tree-scattering model for improved propagation prediction in urban microcells,” *IEEE Transactions on Vehicular Technology*, vol. 53, no. 2, pp. 503 – 513, Mar. 2004. 26, 47, 50, 127

[46] V. Degli-Esposti, V.-M. Kolmonen, E. Vitucci, and P. Vainikainen, “Analysis and modeling on co- and cross-polarized urban radio propagation for dual-polarized MIMO wireless systems,” *IEEE Transactions on Antennas and Propagation*, vol. 59, no. 11, pp. 4247 –4256, Nov. 2011. 26

[47] C. Jandura and J. Voigt, “Analysis of measured and simulated delay and angular propagation channel parameters for MIMO network planning,” in *2011 IEEE Vehicular Technology Conference (VTC Fall)*, Sep. 2011, pp. 1 –5. 27

[48] C. Sturm and W. Wiesbeck, “Ray-tracing in a virtual drive for mobile communications,” in *3rd European Conference on Antennas and Propagation, EuCAP*, Mar. 2009, pp. 1937 –1939. 27

[49] S. Priebe, M. Jacob, C. Jastrow, T. Kleine-Ostmann, T. Schrader, and T. Kurner, "A comparison of indoor channel measurements and ray tracing simulations at 300 GHz," in *35th International Conference on Infrared Millimeter and Terahertz Waves (IRMMW-THz)*, Sep. 2010, pp. 1 –2. 27

[50] G. Tiberi, S. Bertini, W. Malik, A. Monorchio, D. Edwards, and G. Manara, "Analysis of realistic ultrawideband indoor communication channels by using an efficient ray-tracing based method," *IEEE Transactions on Antennas and Propagation*, vol. 57, no. 3, pp. 777 –785, Mar. 2009. 27

[51] C. Oestges, "Propagation modelling of low earth-orbit satellite personal communication system," Ph.D. dissertation, Université catholique de Louvain, 2000. 38

[52] V. Degli Esposti and H. L. Bertoni, "Evaluation of the role of diffuse scattering in urban microcellular propagation," in *1999 IEEE 50th Vehicular Technology Conference (VTC-1999 Fall)*, Amsterdam. The Netherlands, Sept. 1999. 40

[53] J. Poutanen, J. Salmi, K. Haneda, V. Kolmonen, and P. Vainikainen, "Angular and shadowing characteristics of dense multipath components in indoor radio channels," *IEEE Transactions on Antennas and Propagation*, vol. 59, no. 1, pp. 245 –253, Jan. 2011. 41

[54] A. Richter, C. Schneider, M. Landmann, and Thomä, "Parameter estimation results of specular and dense multi-path components in microcell scenarios," in *WPMC 2004*, Abano Terme, Italy, Sept. 2004. 41

[55] F. Quitin, C. Oestges, F. Horlin, and P. De Doncker, "A spatio-temporal channel model for modeling the diffuse multipath component in indoor environments," in *4th European Conference on Antennas and Propagation - EuCAP*, Barcelona, Spain, Apr. 2010. 41, 109

[56] V. Degli Esposti, F. Fuschini, E. M. Vitucci, and G. Falciasecca, "Speed-up techniques for ray tracing field prediction models," *IEEE Transactions on Antennas and Propagation*, vol. 57, no. 5, pp. 1469 – 1480, May 2009. 41, 78, 79

[57] U. Inan and A. Inan, *Electromagnetic Waves.* Prentice Hall, 2000. 46

[58] S. Torrico and R. Lang, "A simplified analytical model to predict the specific attenuation of a tree canopy," *IEEE Transactions on Vehicular Technology*, vol. 56, no. 2, pp. 696 –703, Mar. 2007. 46, 47, 50, 127, 128

[59] M. Weissberger, "An initial critical summary of models for predicting the attenuation of radio waves by trees," Department of Defense, Electromagnetic Compatibility Analysis Center, Tech. Rep., 1982. 46

[60] M. Al-Nuaimi and R. Stephens, "Measurements and prediction model optimisation for signal attenuation in vegetation media at centimetre wave frequencies," *IEE Proceedings Microwaves, Antennas and Propagation*, vol. 145, no. 3, pp. 201 –206, June 1998. 46

[61] ITU-R, "Attenuation in vegetation," Recommendation ITU-R P.833-4, International Telecommunication Union, Tech. Rep., 1999. 47, 127

[62] J. Goldhirsh and W. Vogel. Handbook of propagation effects for vehicular and personal mobile satellite systems. [Online]. Available: http://www.utexas.edu/research/mopro 47

[63] I. Cavdar, H. Dincer, and K. Erdogdu, "Propagation measurements at L-band for land mobile satellite link design," in *Proceedings of the 7th Mediterranean Electrotechnical Conference*, vol. 3, Apr. 1994, pp. 1162 –1165. 47

[64] P. Horak and P. Pechac, "Vegetation attenuation by a single tree for high elevation angles at 2.0 and 6.5 GHz," Department of Electromagnetic Field, Czech Technical University in Prague, Tech. Rep. 47, 127

[65] ITU-R, "Propagation data required for the design of earth-space land mobile telecommunication systems," Recommendation ITU-R PN.681-1, International Telecommunication Union, Tech. Rep., 1994. 47

[66] W. Vogel and J. Goldhirsh, "Earth-satellite tree attenuation at 20 GHz: foliage effects," *Electronics Letters*, vol. 29, no. 18, pp. 1640 –1641, Sep. 1993. 47

[67] S. Seidel and T. Rappaport, "914 MHz path loss prediction models for indoor wireless communications in multifloored buildings,"

IEEE Transactions on Antennas and Propagation, vol. 40, no. 2, pp. 207 –217, Feb. 1992. 50

[68] Y.-C. Lin and K. Sarabandi, "A Monte Carlo coherent scattering model for forest canopies using fractal-generated trees," *IEEE Transactions on Geoscience and Remote Sensing*, vol. 37, no. 1, pp. 440 –451, Jan. 1999. 50

[69] M. Karam, A. Fung, and Y. Antar, "Electromagnetic wave scattering from some vegetation samples," *IEEE Transactions on Geoscience and Remote Sensing*, vol. 26, no. 6, pp. 799 –808, Nov. 1988. 50

[70] P. de Matthaeis and R. H. Lang, "Microwave scattering models for cylindrical vegetation components," *Progress In Electromagnetics Research*, vol. 55, pp. 307–333, 2005. 51

[71] L. Correia, Ed., *Mobile Broadband Multimedia Networks.* Academic Press, 2006. 55, 63

[72] ElektroBit, "ElektroBit channel sounder user manual," Tech. Rep. 57, 60

[73] B. Van Veen and K. Buckley, "Beamforming: a versatile approach to spatial filtering," *IEEE ASSP Magazine*, vol. 5, no. 2, pp. 4 –24, Apr. 1988. 62

[74] R. Schmidt, "Multiple emitter location and signal parameter estimation," *IEEE Transactions on Antennas and Propagation*, vol. 34, no. 3, pp. 276 – 280, Mar. 1986. 62

[75] R. Roy and T. Kailath, "ESPRIT-estimation of signal parameters via rotational invariance techniques," *IEEE Transactions on Acoustics, Speech and Signal Processing*, vol. 37, no. 7, pp. 984 –995, Jul. 1989. 62

[76] J. Fessler and A. Hero, "Space-alternating generalized expectation-maximization algorithm," *IEEE Transactions on Signal Processing*, vol. 42, no. 10, pp. 2664 –2677, Oct. 1994. 62

[77] B. Fleury, M. Tschudin, R. Heddergott, D. Dahlhaus, and K. Ingeman Pedersen, "Channel parameter estimation in mobile radio environments using the SAGE algorithm," *IEEE Journal on Selected Areas in Communications*, vol. 17, no. 3, pp. 434 –450, Mar. 1999. 62

[78] E. Haddad, "Apport de la modelisation deterministe 3D indoor pour l'ingenierie des systems radio avances," Ph.D. dissertation, Telecom Bretagne, 2011. 79

[79] F. Mani, F. Quitin, and C. Oestges, "Accuracy of depolarization and delay spread predictions using advanced ray-based modeling in indoor scenarios," *EURASIP Journal on Wireless Communications and Networking*, no. 11, p. 11, 2011. [Online]. Available: http://jwcn.eurasipjournals.com/content/2011/1/11 81

[80] L. Barclay, *Propagation of Radiowaves.* The Institution of Electrical Engineers, 2003. 81

[81] D. Chizhik, J. Ling, and R. A. Valenzuela, "The effect of electric field polarization on indoor propagation," in *IEEE International Conference on Universal Personal Communications*, Florence, Italy, Oct. 5-9 1998. 81

[82] Y. Lostanlen and G. Gougeon, "Introduction of diffuse scattering to enhance ray-tracing methods for the analysis of deterministic indoor UWB radio channels," in *International Conference on Electromagnetics in Advanced Applications, ICEAA*, Sept. 2007, pp. 903–906. 81

[83] P. Bosselmann, "Planning and analysis of UHF RFID systems for consumer goods logistics using ray tracing predictions," in *1st Annual RFID Eurasia Conference*, Sept. 2007, pp. 1–7. 81

[84] E. Tanghe, W. Joseph, L. Martens, H. Capoen, K. Van Herwegen, and W. Vantomme, "Large-scale fading in industrial environments at wireless communication frequencies," in *Antennas and Propagation Society International Symposium*, Honolulu, Hawaii, Usa, June 2007. 81

[85] S. Haese, C. Moullec, P. Coston, and K. Sayegrih, "High-resolution spread spectrum channel sounder for wireless communications systems," in *IEEE International Conference on Personal Wireless Communication*, 1999, pp. 170–173. 82

[86] SMT-8TO25M-A SkyCross antenna. [Online]. Available: http://www.skycross.com/Products/PDFs/SMT-8TO25M-A.pdf 82

[87] F. Gallee, "Development of an isotropic sensor 2GHz - 6GHz," in *European Microwave Conference*, 9-12 2007, pp. 91 –93. 87, 94

[88] R. Wilson. Propagation losses through common building materials. [Online]. Available: http://www.am1.us/Papers/E10589.pdf 89

[89] O. Landron, M. Feuerstein, and T. Rappaport, "A comparison of theoretical and empirical reflection coefficients for typical exterior wall surfaces in a mobile radio environment," *IEEE Transactions on Antennas and Propagation*, vol. 44, no. 3, pp. 341–351, March 1996. 89

[90] H. Bertoni, *Radio Propagation for Modern Wireless Systems.* Prentice Hall, 2000. 89

[91] J. Baker Jarvis, M. Janeziw, B. Riddle, R. Johnk, P. Kabos, C. Holloway, R. Gever, and C. Grosvenor, "Measuring the permittivity and permeability of lossy materials: solids, liquids, metals, building materials, and negative-index materials," National Institute of Standards and Technology, USA, Tech. Rep. 1536, Feb. 2005. 89, 95

[92] F. Mani, F. Quitin, and C. Oestges, "Directional spreads of dense multipath components in indoor environments: experimental validation of a ray-tracing approach," *IEEE Transactions on Antennas and Propagation*, 2012, accepted for pubblication. 92

[93] X. Yin, B. Fleury, P. Jourdan, and A. Stucki, "Polarization estimation of individual propagation paths using the SAGE algorithm," in *Proc. of the PIMRC 2003 - Personal, Indoor and Mobile Radio Communications*, 2003. 94

[94] F. Quitin, C. Oestges, F. Horlin, and P. De Doncker, "A polarized clustered channel model for indoor multiantenna systems at 3.6 GHz," *IEEE Transactions on Vehicular Technology*, vol. 59, no. 8, pp. 3685 –3693, Oct. 2010. 94

[95] B. Montenegro, B. Clerckx, D. Vanhoenacker-Janvier, and C. Oestges, "Literature review and preliminary models for propagation into buildings and forests," Sensor for Terrestrial and Airborne Radio transmitter Rescue Search - STARRS Project, Tech. Rep., 2007. 95

[96] N. Czink, A. Richter, E. Bonek, J.-P. Nuutinen, and J. Ylitalo, "Including diffuse multipath parameters in MIMO channel models," in *2007 IEEE 66th Vehicular Technology Conference. VTC-2007 Fall.*, Oct. 2007, pp. 874 –878. 108

[97] J. Salmi, J. Poutanen, K. Haneda, A. Richter, V.-M. Kolmonen, P. Vainikainen, and A. F. Molisch, "Incorporating diffuse scattering in geometry-based stochastic MIMO channel models," in *4th European Conference on Antennas and Propagation - EuCAP*, Barcelona, Spain, Apr. 2010. 108, 123

[98] R. Verdone, Ed., *Pervasive Mobile & Ambient Wireless Communications: The COST Action 2100.* Springer, 2011. 109

[99] F. Mani and C. Oestges, "Ray-tracing evaluation of diffuse scattering in an outdoor scenario," in *Proceedings of the 5th European Conference on Antennas and Propagation (EuCAP 2011)*, Apr. 2011, pp. 3439–3443. 119

[100] ——, "A ray-based method to evaluate scattering by vegetation elements," *IEEE Transactions on Antennas and Propagation*, 2012, accepted for pubblication. 119

[101] Generation of 3D fractal trees. [Online]. Available: http://www.mathworks.com/matlabcentral/fileexchange/29537-generation-of-3d-fractal-trees 127

[102] P. Prusinkiewicz and A. Lindenmayer. The algorithmic beauty of plants. [Online]. Available: http://algorithmicbotany.org/papers 128

[103] E. M. Vitucci, F. Mani, V. Degli-Esposti, and C. Oestges, "Polarimetric properties of diffuse scattering from building walls: Experimental parameterization of a ray-tracing model," *IEEE Transactions on Antennas and Propagation*, 2012, accepted for publication. 134

[104] E. Vitucci, V. Mani, F. Degli Esposti, and C. Oestges, "Study of a polarimetric model for diffuse scattering in urban environment," in *Proceedings of the 6th European Conference on Antennas and Propagation (EuCAP 2012)*, Mar. 2012. 147

[105] T. Callaghan, N. Czink, F. Mani, A. Paulraj, and G. Papanicolaou, "Correlation-based radio localization in an indoor environment," *EURASIP Journal on Wireless Communications and Networking*, vol. 2011, no. 1, p. 135, 2011. 159, 161

[106] A. Ruddle, "Computed SAR levels in vehicle occupants due to on-board transmissions at 900 MHz," in *Loughborough Antennas Propagation Conference, 2009*, Nov. 2009, pp. 137 –140. 160, 162

[107] Boeing 737 airplane description. [Online]. Available: http://www.boeing.com/commercial/airports/acaps/737sec2.pdf 168

[108] N. Czink, F. Kaltenberger, Y. Zhou, L. Bernado, T. Zemen, and X. Yin, "Low-complexity geometry-based modeling of diffuse scattering," in *4th European Conference on Antennas and Propagation - EuCAP*, Barcelona, Spain, Apr. 2010. 175

List of publications

Journal papers

- F. Mani, F. Quitin and C. Oestges, "Accuracy of depolarization and delay spread predictions using advanced ray-based modeling in indoor scenarios," *EURASIP Journal on Wireless Communications and Networking*, no. 11, 2011.

- T. Callaghan, N. Czink, F. Mani, A. Paulraj and G. Papanicolaou, "Correlation based radio localization in an indoor environment," *EURASIP Journal on Wireless Communications and Networking*, no. 135, 2011.

- E. M. Vitucci, F. Mani, V. Degli Esposti and C. Oestges, "Polarimetric properties of diffuse scattering from building walls: Experimental parameterization of a ray-tracing model," *IEEE Transactions on Antennas and Propagation*, June 2012, in press.

- F. Mani, F. Quitin and C. Oestges, "Directional spreads of dense multipath components in indoor environments: experimental validation of a ray-tracing approach," *IEEE Transactions on Antennas and Propagation*, July 2012, in press.

- F. Mani and C. Oestges, "A ray-based method to evaluate scattering by vegetation elements," *IEEE Transactions on Antennas and Propagation*, 2012, accepted for pubblication.

Conference papers

- F. Mani, C. Oestges, "A ray based indoor propagation model including depolarizing penetration," in*Proceedings of the 3rd European Conference on Antennas and Propagation (EuCAP 2009)*, Mar. 2009.

- F. Mani, C. Oestges, "Evaluation of diffuse scattering contribution for delay spread and cross-polarization ratio prediction in an indoor scenario," in*Proceedings of the 4th European Conference on Antennas and Propagation (EuCAP 2010)*, Apr. 2010.

- E. M. Vitucci, F. Mani, V. Degli-Esposti and C. Oestges, "A study on polarimetric properties of scattering from building walls," *IEEE 72nd Vehicular Technology Conference Fall (VTC 2010-Fall)*, Sep. 2010.

- F. Mani and C. Oestges, "Ray-tracing evaluation of diffuse scattering in an outdoor scenario," in*Proceedings of the 5th European Conference on Antennas and Propagation (EuCAP 2011)*, Apr. 2011.

- E. M. Vitucci, F. Mani, V. Degli Esposti, and C. Oestges, "Study of a polarimetric model for diffuse scattering in urban environment," in *Proceedings of the 6th European Conference on Antennas and Propagation (EuCAP 2012)*, Mar. 2012.

COST TDs

- F. Mani and C. Oestges, "Evaluation of diffuse scattering contribution in warehouse scenario", COST 2100 TD(09)812, May 2009.

- F. Mani, F. Quitin and C. Oestges, "Evaluation of diffuse scattering contribution in office scenario", COST 2100 TD(10)10001, Feb. 2010.

- E. M. Vitucci, F. Mani, V. Degli Esposti and C. Oestges, "A study on polarimetric properties of scattering from building walls", COST 2100 TD(10)11020, Jun. 2010.

- F. Mani and C. Oestges, "Ray-Tracing evaluation of diffuse scattering in an outdoor scenario", COST 2100 TD(10)12018, Nov. 2010.

- F. Mani, F. Quitin and C. Oestges, "Directional spreads of dense multipath components: a ray-tracing approach,", COST IC1004 TD(11)02003, Oct. 2011.

- E. M. Vitucci, F. Mani, V. Degli Esposti and C. Oestges, "Polarimetric properties of diffuse scattering from building walls", COST IC1004 TD(11)02006, Oct. 2011.

- F. Mani and C. Oestges, ”A ray-based method to evaluate scattering by vegetation elements,” COST IC1004 TD(12)04018, May 2012.